The petrogenesis of Liberian diamondiferous rocks, Man Craton, West Africa

By: Njabulo Ndimande

A dissertation submitted in fulfilment for the degree of

Master of Science

in the Department of Geological Sciences,

University of Cape Town, South Africa

February 2022

Supervisor: Dr Geoffrey Howarth

Declaration

I, NJABULO NDIMANDE (Student Number: NDMNJA001), know the meaning of plagiarism and declare that all of the work in this dissertation, save for that which is properly acknowledged, is my own.

Signature: Signed by candidate

Date: 11 – 02 – 2022

Acknowledgements

First and foremost, I would like to truly thank my supervisor, Dr Geoffrey Howarth, for giving me the opportunity to do this research, I will forever be grateful for his support and scientific guidance. I would also like to thank the following people for their great assistance in various aspects of my research:

- Rene van der Merwe for preparation of thin sections.
- Assoc Prof Philip Janney and Christel Tinguely for their assistance in ICP-MS analyses.
- Dr Petrus le Roux for his assistance in Sr and Nd radiogenic isotope analyses.
- Christian Reinke (from the University of Johannesburg) and Nicolas Laidler for assisting me with Microprobe analyses.

Abstract

Kimberlites and lamproites are ultramafic igneous rocks believed to originate from the convective asthenosphere and sub-continental lithospheric mantle, respectively, however, the genetic link between these rock types is still a debate among researchers. Recently, it has been shown (e.g., in the Dharwar Craton, India) that both kimberlites and lamproites may be derived from the same asthenospheric mantle source. During their ascent to the surface, they assimilate differently metasomatized SCLM material. However, it is not clear if this process applies to all cratonic regions.

The Man Craton, West Africa, is a host to diamondiferous rocks that share petrographic and geochemical characteristics with both kimberlites and lamproites, thus not easy to classify. The Camp Alpha (possibly Precambrian in age) and Neoproterozoic-aged Weasua clusters are the selected locations for this study. To further assist with the classification of peculiar West African diamondiferous rocks and evaluate their genetic link and origin, I provide detailed petrography, as well as phlogopite and spinel chemistry, bulk-rock geochemistry (for the Camp Alpha samples) and perovskite chemistry (for the Weasua samples).

The Camp Alpha rocks contain abundant macrocrysts of olivine (that are completely altered) and ilmenite occurring in a groundmass that comprises spinel, phlogopite (the samples are phlogopite-poor), perovskite, calcite, serpentine, and rare apatite. Most importantly, there is no evidence of diopside in the Camp Alpha samples. The Camp Alpha phlogopite is enriched in Al_2O_3 but slightly depleted in FeO and TiO_2 and the spinel exhibits a kimberlitic compositional evolution (i.e., trend 1). The bulk-rock trace element ratios Ba/Nb (0.91 – 9.55), La/Nb (0.12 – 1.22; mostly < 1.10) and Ce/Pb (6.77 – 99.2; mostly > 22), fall within the ranges defined by kimberlites. Additionally, primitive mantle normalised trace element patterns are similar to kimberlite patterns (e.g., Rb, K, Sr and P show negative anomalies). As a result of these characteristics, the studied Camp Alpha rocks are classified as kimberlites. A close to parent melt composition of the Camp Alpha kimberlite is provided in this study, based on bulk rock geochemistry. The composition of the estimated melt is similar to that of kimberlite magmas and characterised by low K_2O (of 0.80 wt.% relative to 3.63 ± 1.40 wt.% of orangeites for example; reflective of mica-poor nature). The Weasua rocks, in this study, are micaceous (phlogopite-rich) and contain primary groundmass diopside and calcite, which suggests that the studied Weasua rocks represent carbonate-rich olivine lamproites. From the inversion of trace element data for the perovskites using known partition coefficients, the composition of the melt in equilibrium with perovskite at the time of crystallisation is determined. The composition of this Weasua parent melt is similar to that of kimberlite magmas (i.e., similar primitive mantle-normalised trace element patterns, Ba/Nb, Ce/Pb and La/Nb ratios).

Whereas the Camp Alpha and Weasua rocks are classified as kimberlite and lamproite, respectively, the trace element composition of the parent melt is similar to that of kimberlite magmas for both cases. This suggests a common asthenospheric magma source for the Camp Alpha kimberlite and Weasua lamproite. *En route* to the surface, these rock types assimilated differently metasomatized SCLM material (i.e., the Weasua lamproite magma assimilated mica-diopside-rich wall rock). The Camp Alpha kimberlite was shown to be approximately 800 Ma old, similar to the Weasua lamproite. Therefore, the Camp Alpha and Weasua magmas were interpreted to be broadly coeval based on the similarity in age and location, In addition to the Indian Dharwar Craton, the hypothesis that kimberlites and lamproites share a common convective asthenospheric magma source but assimilate differently metasomatized SCLM material *en route* to the surface is confirmed in the Man Craton, West Africa.

Contents

List of Figures

List of Tables

CHAPTER 1: Introduction

Kimberlites and olivine (cratonic) lamproites are ultramafic igneous rocks that crystallise from magmas forming as a result of low degrees of partial melting in the upper mantle (e.g., Mitchell, 1995, 2005). These magmas are the primary transporters of diamonds from the mantle to the Earth's surface. Lamproites are divided into orogenic and cratonic lamproites (e.g., Mitchell and Bergman, 1991). Orogenic lamproites are found in orogenic belts and related to complex subduction processes (e.g., Mitchell and Bergman, 1991; Mitchell, 2020). Kimberlites are typically mica-poor and contain abundant primary groundmass carbonate (e.g., Mitchell, 1995; Mitchell et al., 2019). Most importantly, kimberlites do not contain primary (magmatic) diopside, and if diopside is present, it is a secondary phase (e.g., Mitchell, 1995). Conversely, lamproites are typically micaceous and contain primary diopside but not primary carbonate (e.g., Mitchell and Bergman, 1991; Mitchell, 1995). Kimberlites and lamproites occasionally occur together (e.g., the Wajrakarur kimberlite-lamproite field located in the Dharwar Craton, southern India; Sarkar et al., 2021; Shaikh et al., 2018)), but their petrogenetic association is unclear. i.e., are they related to each other or not?

The origin of kimberlites and lamproites has been a long debate among researchers. The source region of both kimberlites and lamproites was first thought to be located within the sub-continental lithospheric mantle (SCLM) (e.g., le Roex et al., 2003; Becker and le Roex, 2006). However, the model that is now well accepted, suggests that kimberlites are derived from very small degrees of partial melting (< 1%) of carbonated garnet lherzolite in the convective asthenospheric mantle (e.g., Stamm and Schmidt, 2017; Pearson et al., 2019; Woodhead et al., 2019; Giuliani et al., 2020). During their ascent to the near-surface, the asthenosphere-derived kimberlite melts incorporate and assimilate a significant amount of sub-continental lithospheric mantle (SCLM) material in the form of xenocrysts and xenoliths (e.g., Dalton et al., 2020; Tovey et al., 2021; Pearson et al., 2019; Giuliani et al., 2020). Assimilation of SCLM material affects the composition of major elements, whereas the trace elements are less sensitive to assimilation due to their high abundances (e.g., Giuliani et al., 2020). Lamproites, on the other hand, are generally believed to originate from the non-convective SCLM and are derived from low degree partial melting of intensely metasomatized SCLM lithologies such as mica-amphibole-rutile-ilmenite-diopside (MARID) veins in lithospheric harzburgite (e.g., Coe et al., 2008; Mitchell, 2005;Giuliani *et al.*, 2015). As a result, kimberlites exhibit similar isotopic and trace element patterns worldwide (i.e., the asthenosphere is homogeneous) whereas the compositions of lamproites may differ from Craton to Craton (i.e., the SCLM is heterogeneous).

Recently, it has been shown that lamproites may be derived from a convective asthenospheric source, similar to that of kimberlites. The Dharwar Craton is host to both kimberlites and lamproites (i.e., the Wajrakarur kimberlite-lamproite field, located in southern India; Chalapathi Rao et al., 2004; Shaikh et al., 2018; Sarkar et al., 2021). The Wajrakarur kimberlites and lamproites have different petrography, mineralogy and major element chemistry but exhibit remarkably similar trace element and Sr-Nd-Hf isotope patterns (Paton et al., 2009; Pandey and Chalapathi Rao, 2020; Shaikh et al., 2018; Sarkar et al., 2021). The Wajrakarur kimberlites and lamproites are, therefore, believed to share a common asthenospheric mantle source (e.g., Sarkar et al., 2021) (because trace elements are less sensitive to assimilation, thus, they represent the nature of the source). The difference in petrography, mineralogy and major element chemistry is interpreted to be related to a primary asthenospheric magma that assimilated a heterogeneous SCLM, resulting in the occurrence of both kimberlites and lamproites (Sarkar et al., 2021). However, it is not clear how common this process may be or if it applies to other cratonic regions. For example, the mineralogy and major element chemistry, as well as trace element and Sr-Nd-Hf isotope composition of orangeites (formerly Group II kimberlites) are clearly different from those of kimberlites, implying different source regions (e.g., Becker and le Roex, 2006).

Kimberlites have been found in all Archean cratonic regions worldwide, but some areas have been studied far more than others, i.e., southern Africa, Canada, Russia and India. The Man Craton, West Africa, has seen far fewer studies, mostly due to inaccessibility. The known diamondiferous rocks of the Man Craton include a total of seven Jurassic-aged clusters (Koidu and Tongo clusters in Sierra Leone; Banankoro, Bouro and Droujba clusters in Guinea; Kumgbo and Mano Godua clusters in Liberia), one Neoproterozoic-aged cluster (Weasua cluster in Liberia), and the Camp Alpha cluster also in Liberia (e.g., Skinner et al., 2004) (Fig. 1). The exact age of the Camp Alpha cluster is unknown, however, Haggerty (2017) suggested that it might be Precambrian in age.

The West African diamondiferous rocks show unusual characteristics and are not easily classified as kimberlite or lamproite (e.g., Tongo; Howarth and Giuliani, 2020; Koidu; Taylor et al., 1994). The Tongo and Koidu rocks are micaceous and contain groundmass carbonate and are petrographically similar to orangeites. However, their trace element and Sr-Nd isotope compositions are similar to those of kimberlites or transitional towards the Aries olivine lamproite (Tongo; Howarth and Giuliani, 2020; Koidu; Taylor et al., 1994). The rocks from the Weasua cluster described by Skinner et al. (2004) are petrographically, mineralogically and geochemically similar to kimberlites (e.g., no evidence of primary diopside and bulk-rock geochemistry is similar to that of kimberlites). However, the Weasua rocks described by Howarth and Giuliani (2020) were petrographically and mineralogically similar to lamproites (i.e., micaceous and contain primary diopside).

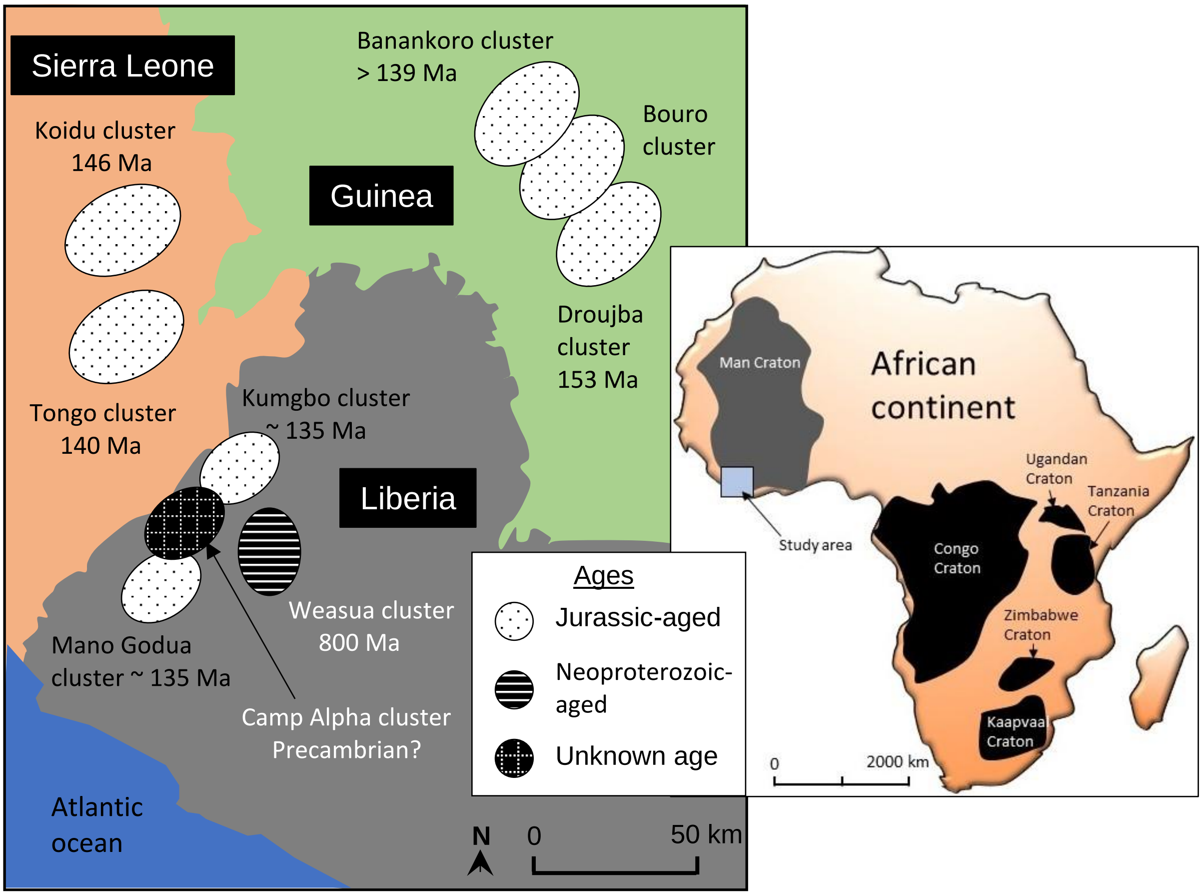

Fig. 1. Map showing the approximate distribution of West African kimberlites/lamproites, including the Camp Alpha and Weasua clusters. Modified after Skinner *et al.* (2004).

Based on mineralogy alone the West African diamondiferous rocks are not easy to classify as kimberlite or lamproite, however, their similar bulk-rock trace element suggests possible derivation from a common kimberlitic mantle reservoir. Thus, the diamondiferous rocks of the Man Craton are ideal for testing the hypothesis that kimberlites and lamproites can be derived from a common mantle source but undergo variable degrees of SCLM assimilation that result in the varying mineralogy and bulk-rock major element compositions.

One of the primary goals of this study is to address the classification issue for the West African diamondiferous rocks. Additionally, the link between kimberlites and lamproites occurring within the same cratonic region will be further evaluated to address the importance of understanding melt-SCLM interactions in controlling the composition of magmas erupting in cratonic regions.

1.1 Aims and Objectives

The Weasua and Camp Alpha clusters, both located in Liberia, are the chosen regions for this study (Fig. 1). The Camp Alpha rocks are relatively understudied, but the work of Haggerty (2017) suggested that the Camp Alpha region contains predominantly kimberlites. However, these Camp Alpha rocks are non-micaceous and petrographically different to the highly micaceous kimberlites from Tongo and Koidu. Camp Alpha, Tongo and Koidu clusters occur within the same Craton and are kimberlites, therefore, the main question is why do they appear mineralogically different?

Additionally, both kimberlites and lamproites are reported from Liberia (i.e., Weasua kimberlite; Skinner *et al.*, 2004; Weasua lamproite; Howarth and Giuliani, 2020). Skinner *et al.* (2004) reported bulk-rock trace element geochemistry for the kimberlitic rocks, however, no bulk-rock data is available for the lamproitic rocks. Thus, a second major goal of this work is to present estimates of the trace element compositions for the Weasua lamproites using perovskite to evaluate their origin and association with kimberlites in the region.

The main goal of this study is to:

- Constrain the petrogenesis and melt-SCLM interaction of the Weasua and Camp Alpha rocks (and other West African kimberlites and lamproites, in general), to understand the origin of these rocks in comparison with the micaceous kimberlites from Sierra Leone and kimberlites worldwide. The overall goal is to evaluate the link between kimberlites and lamproites in cratonic regions.

To achieve the main goal, the following approach will be used:

- Present the petrography, mineral chemistry (for Camp Alpha; phlogopite and spinel; for Weasua; perovskite) and bulk-rock geochemistry (for Camp Alpha).
- Compare and classify the Camp Alpha and Weasua rocks based on their petrography and mineral chemistry characteristics.
- Constrain the parent melt composition for both regions. The close to parent magma composition for the Camp Alpha rocks will be estimated using the bulk

rock geochemistry (major element concentrations will be taken from Haggerty (2017) and the trace elements will be analysed in this study).

- The formation of perovskite will be constrained with interest in using its trace element concentrations as a proxy for the parent melt composition of the Weasua rocks (only polished sections were available from this location, thus, the bulk-rock geochemistry analysis could not be conducted). Perovskite hosts incompatible trace elements (e.g., REE), is resistant to near-surface weathering and capable of recording primary isotopic and geochemical information of the kimberlitic magma (e.g., Castillo-Oliver *et al.*, 2016; Yang *et al.*, 2009). Therefore, this mineral is a good proxy for trace element concentrations of the parent melt from which it crystallised.

CHAPTER 2: Background

In this chapter:

a) The discovery of diamondiferous rocks and recognition of different types are briefly discussed.

b) The mineralogy, mineral chemistry (of phlogopite and spinel) and geochemistry of kimberlites, lamproites, and orangeites are discussed and compared in order to develop the best approach in discriminating between these diamondiferous rock types and in understanding their petrogenesis. Ultimately, the aim is to use the discrimination approach developed in section 2.2 on West African diamondiferous rocks analysed in this study.

c) Lastly, the occurrence, mineralogical and geochemical characteristics of diamondiferous rocks in the Man Craton, West Africa, are briefly discussed to illustrate their similarities and differences.

2.1 Kimberlite discovery and their brief history

Kimberlites, orangeites and olivine lamproites are ultramafic igneous rocks that result from the differentiation and crystallisation of magmas derived from the upper mantle (e.g., Mitchell, 2005). Kimberlites were first discovered in the Kaapvaal Craton in Dorstfontein and Bultfontein farms, which are located in Kimberley, South Africa (e.g., Mitchell, 1995). They were found through the recovery of diamonds and are currently considered the main source of diamonds worldwide (e.g., Mitchell, 1995). Diamonds in the Kimberley region were initially considered to be contained within alluvial deposits but through continuous excavation, funnel-like structures (Fig. 2) were found to be the primary sources of diamonds (e.g., Mitchell, 1995). In 1887, Henry Carvill Lewis named these funnel-like diamond-bearing structures “kimberlites”, from their occurrence in Kimberley, South Africa. Following their first discovery in the Kaapvaal Craton, kimberlites have been discovered on every continent and have been the subject of many studies (Wagner, 1914; Mitchell, 1970, 1995; Skinner and Clement, 1979; Smith, 1983; Clement et al., 1984; Fraser et al., 1985; Beard et al., 2000; Armstrong et al., 2004; Chalapathi Rao et al., 2004).

Kimberlites were petrologically described for the first time by Wagner (1914). Wagner (1914) observed two separate types of kimberlites within the Kaapvaal Craton and called them basaltic and micaceous kimberlites, but these observations were based on the macroscopic appearance of the rocks. Subsequently, Wagner (1928) referred to micaceous kimberlites as orangeites, in recognition of their initial discovery in the Orange Free State, South Africa. Skinner and Clement (1979) noted mineralogical differences between the two kimberlite groups, thus, their classification was initially based on primary groundmass modal mineralogy. Skinner and Clement (1979) classified the two types as *monticellite calcite serpentine kimberlite* (equivalent to Wagner's basaltic kimberlite) and *phlogopite kimberlite* (equivalent to Wagner's micaceous kimberlite). In 1983, Craig Smith observed differences in isotopic compositions in the two kimberlite types. Smith (1983) suggested that monticellite calcite serpentine kimberlite be called *group I kimberlites* and phlogopite kimberlites be called *group II kimberlites*.

Group I kimberlites contain less radiogenic $^{87}Sr/^{86}Sr$ and more radiogenic $^{143}Nd/^{144}Nd$ compositions compared to present-day Bulk silicate Earth (e.g., Smith, 1983; Becker and le Roex, 2006). In contrast, group II kimberlites contain more radiogenic $^{87}Sr/^{86}Sr$ and less radiogenic $^{143}Nd/^{144}Nd$ compositions compared to present-day Bulk Earth (Smith, 1983; Becker and le Roex, 2006). The classification by Smith (1983) was primarily based on isotopic grounds rather than the petrographic character of the rocks. Many studies have reported mineralogical and geochemical differences between group I and II kimberlites (e.g., Mitchell and Meyer, 1986; Dawson, 1987; Skinner, 1989; Tainton and Browning, 1991; Fraser and Hawkesworth, 1992; Skinner et al., 1994; Tainton and McKenzie, 1994; Mitchell, 1995). These studies concluded that group I and group II kimberlites come from different depths in the mantle and their magma sources are dissimilar. Skinner (1989) noted that group I kimberlites are distributed throughout the world whereas group II kimberlites are unique to the Kaapvaal Craton, South Africa. Mitchell (1991, 1995) and Mitchell and Bergman (1991) re-introduced the name *orangeite* to be used rather than group II kimberlites because they are mineralogically and geochemically distinct from kimberlites (group I) and more similar to lamproites (e.g., Mitchell, 1995). Group II kimberlites/orangeites are now recognised as a unique style of lamproite restricted to South Africa (e.g., Pearson et al., 2019). Pearson *et al.* (2019) recommended that orangeites should be termed “carbonate-rich olivine lamproite” or simply “lamproite” for orangeites with more evolved compositions. For simplicity and clarity, the term “*orangeite*” will be used throughout this thesis to refer specifically to occurrences in the Kaapvaal Craton. Orangeites are generally older than kimberlites in the Kaapvaal Craton and their emplacement ages range from 110 to 200 Ma (e.g., Smith, 1983; Mitchell, 1995). The emplacement ages of kimberlite predominantly range from 80 to 100 Ma (e.g., Smith et al., 1985; Mitchell, 1995), but significantly older kimberlites have been discovered in southern Africa: Kuruman Province (~1600 Ma), Premier (1150 Ma) and Venetia (520 Ma) (e.g., Mitchell, 1995; Donnelly et al., 2011; Griffin et al., 2014).

Lamproites were discovered by the first identified occurrence of leucite-bearing rocks (later became Leucite Hills lamproites) in the southwestern Wyoming region, North America (Emmons, 1877). In 1907, the recognition of similar leucite-bearing rocks in Western Australia led to the legitimisation of lamproites (Fitzgerald, 1907; Wade and Prider, 1940).

Kimberlites and orangeites are derived from within the diamond stability field (e.g., Fig. 3), thus, they can contain diamonds (e.g., Mitchell, 1995). However, they are not the only source of diamonds and diamondiferous lamproites have been found worldwide. Some examples of diamondiferous lamproites include the Prairie Creek intrusion in Arkansas, USA (e.g., Smith and Skinner, 1984), the Aries lamproite in Western Australia (e.g., Edwards et al., 1992; Downes et al., 2006) and the Ellendale lamproite pipe in Western Australia (e.g., Evans et al., 2013).

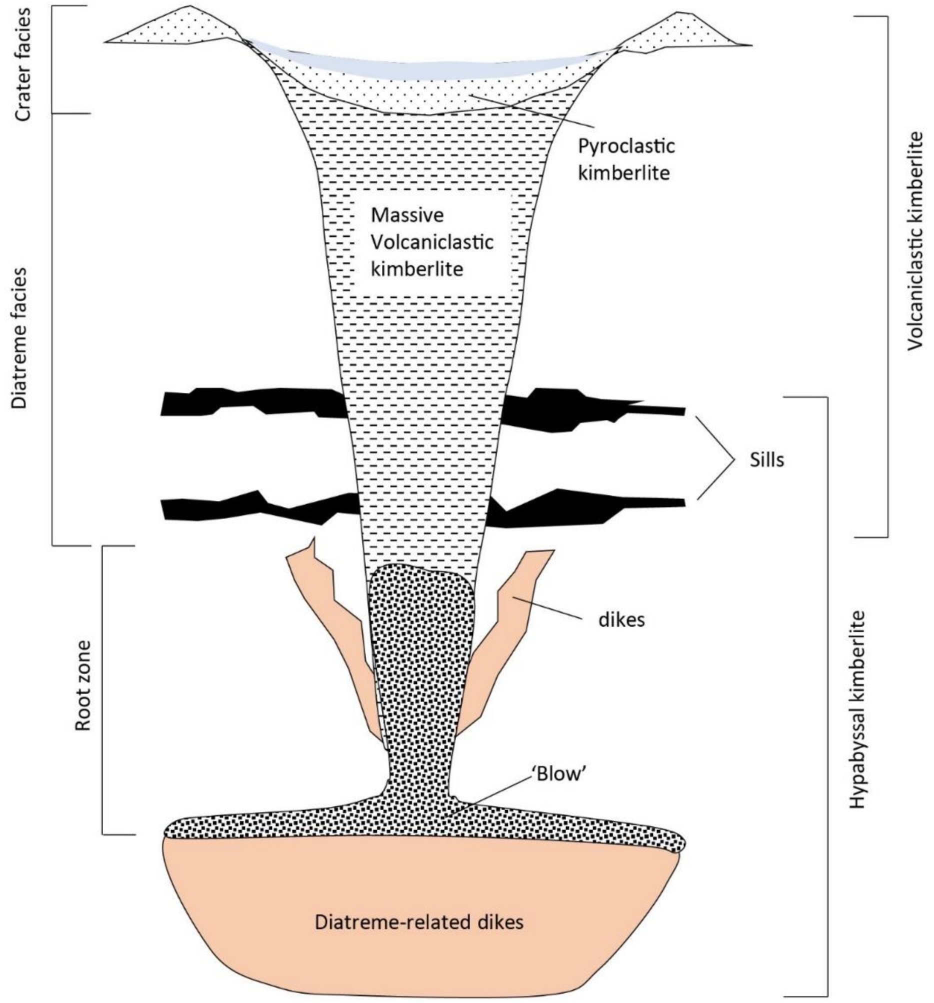

Fig. 2. A model of a kimberlite magmatic system, forming cylindrical funnel-like structures (adapted from Mitchell (1986)).

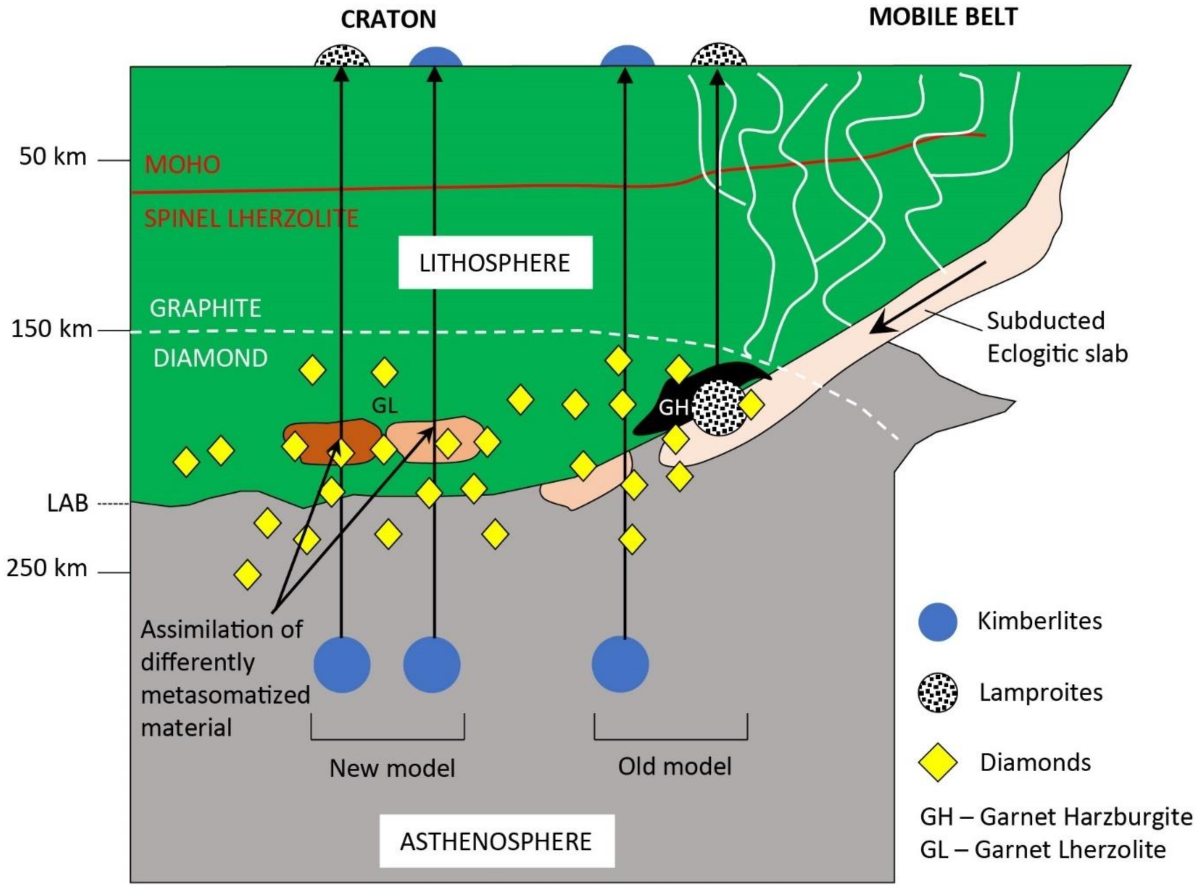

Fig. 3. A cross-section of an Archaean Craton next to a subduction zone and a mobile belt. The cross-section shows the origin of kimberlites and lamproites according to current hypotheses. Kimberlites are believed to be sourced from the convective asthenospheric mantle, whereas orangeites and lamproites are derived from the SCLM. A new hypothesis suggests that both kimberlites and lamproites are sourced from the convective asthenospheric mantle region (Adapted from Mitchell, 2005).

2.2 Characteristics of kimberlites, orangeites and lamproites

2.2.1 Mineralogy

A summary of mineralogical variation in kimberlites, orangeites and lamproites is shown in Table 1.

Kimberlites

Kimberlites are typically mica-poor and defined as potassic, volatile-rich (CO_2 predominant), ultramafic igneous rocks that are characterised by an inequigranular texture, as a result of mega/macrocrysts occurring in a fine-grained primary groundmass (e.g., Clement et al., 1984; Mitchell, 1995). The megacrysts (> 10 mm in size) and macrocrysts (0.5 – 10 mm in size) are anhedral mantle xenocrysts and are not genetically related to the kimberlite magma (e.g., Mitchell, 1995). Abundant olivine crystals, common Cr-poor mega/macrocryst suite (i.e., titanian pyrope, magnesian ilmenite, subcalcic diopside, enstatite and zircon), phlogopite and Ti-poor chromite constitute the mega/macrocryst assemblage (e.g., Mitchell, 1995). The groundmass assemblage comprises a second generation of euhedral to subhedral olivine occurring together with phlogopite (late-stage poikilitic micas that belong to the barian phlogopite-kinoshitalite series are common in most kimberlites), monticellite, spinel (ranging from Mg-Chromite to Mg-ulvöspinel; atoll spinel is also common), perovskite, apatite, carbonate (common calcite and rare dolomite), and serpentine (replacement of earlier formed olivine, monticellite, apatite and phlogopite by deuteric serpentine is common) (Clement et al., 1984; Mitchell, 1995; Batumike et al., 2019; Giuliani et al., 2017).

An important feature is that kimberlites may contain subcalcic diopside (which is xenocrystic) but primary groundmass diopside (which is magmatic) is absent (e.g., Mitchell, 1995). When diopside is present in the kimberlite groundmass, it is a secondary phase (i.e., an alteration product) and is caused by the assimilation of silica-rich xenoliths (e.g., Mitchell, 1995; Mitchell et al., 2009). In contrast, orangeites and lamproites, as described in detail below, can contain primary groundmass diopside (e.g., Mitchell and Bergman, 1991; Mitchell, 1995). Additionally, phases such as sanidine, K-richterite, aegirine and leucite are absent in kimberlites but present in lamproites and some more evolved orangeites (e.g., Mitchell and Bergman, 1991; Mitchell, 1995).

Lamproites

Lamproites are characterised by the presence of anhedral forsteritic olivine macrocrysts and phlogopite microcrysts, occurring in a fine-grained matrix (e.g., Mitchell and Bergman, 1991). The groundmass comprises common titanian poikilitic phlogopite (ranging from phlogopite to tetraferriphlogopite), K-richterite, leucite, sanidine, secondary serpentine, apatite and Al-poor primary diopside (magmatic). The minor groundmass minerals include spinel (compositional zoning from chromite to magnetite; atoll spinel absent), Sr-rich perovskite, priderite, aegirine and jeppeite (e.g., Mitchell and Bergman, 1991). In comparison to kimberlites, lamproites contain primary diopside (magmatic) but groundmass phases such as monticellite and carbonate are absent (e.g., Mitchell and Bergman, 1991). Additionally, lamproites are characterised by the absence of primary plagioclase (although late-stage albite can be formed), nepheline, melilite, kalsilite (SiO_2 activity is much higher in lamproites) and Al-rich augite (e.g., Bergman, 1987; Mitchell and Bergman, 1991).

The above-mentioned minerals are not all required to be present for the rock to be classified as a lamproite and one or more of them can be dominant. As a result, lamproites show an exceedingly wide range in mineralogy from olivine-rich, through olivine-phlogopite-rich and phlogopite-leucite-rich, to leucite-rich lamproites (e.g., Mitchell and Bergman, 1991; Mitchell, 1995). Additionally, lamproites contain phlogopite with different textures and compositions, and this has petrogenetic significance. Rocks with microcrystal phlogopite are termed '*phlogopite lamproites*' (e.g., Olivine-phlogopite lamproites; Ellendale field, West Kimberley Province; Mitchell and Bergman, 1991) and rocks containing poikilitic groundmass phlogopite are termed '*madupitic lamproites*' (e.g., leucite-madupitic lamproites; Leucite Hills lamproites; Mitchell and Bergman, 1991; Mirnejad and Bell, 2006).

Orangeites

Orangeites are restricted to the Kaapvaal Craton. Orangeites comprise two endmembers (i.e., unevolved and evolved) based on the degree of evolution (e.g., Mitchell, 1995).

Unevolved endmembers

Unevolved orangeites are mineralogically more similar to kimberlites. The groundmass comprises abundant phlogopite, spinel (Mg-chromite to Ti-magnetite) and serpentine, common olivine, monticellite (very rare, only reported by Howarth et al., 2011), perovskite, melilite, apatite, carbonate (common calcite and rare dolomite) and most importantly they may or may not contain diopside (e.g., Mitchell, 1995). Primary magmatic diopside best distinguishes unevolved orangeites from kimberlites (i.e., the latter does not contain primary diopside), however, where diopside is absent it can be difficult to discriminate orangeite from kimberlite based on mineralogy alone (e.g., Mitchell, 1995). Unevolved orangeites lack phases such as sanidine, K-richterite and leucite (which are all present in evolved orangeites) but contain abundant carbonate (a phase that is absent in lamproites). As a result, the term '*carbonate-rich lamproites*' has been suggested for unevolved orangeites (or similar occurrences) (Pearson *et al.*, 2019).

Evolved endmembers

Evolved orangeites exhibit similar characteristics to lamproites. The groundmass comprises common titanian poikilitic phlogopite (ranging from phlogopite to tetraferriphlogopite), K-richterite, leucite, sanidine, secondary serpentine, apatite and Al-poor primary diopside (magmatic). The minor groundmass minerals include spinel, Sr-rich perovskite, priderite, aegirine and jeppeite (e.g., Mitchell and Bergman, 1991). Evolved orangeites are simply termed '*lamproites*' (Pearson *et al.*, 2019)

Table 1. Mineralogical variation in kimberlites, orangeites and lamproites. The table is after Mitchell (1995).

	Kimberlites	Orangeites		Lamproites
		Unevolved	Evolved	
Megacrysts	Characteristic	Rare to absent	Rare to absent	Rare to absent
Olivine				
Macrocrysts	Abundant	Common	Rare	Rare
Microcrysts	Common, euhedral to subhedral	Common to minor, euhedral to subhedral dog's tooth	Minor, euhedral to subhedral dog's tooth	Minor, euhedral to subhedral
Mica				
Macrocrysts	Minor, phlogopite	Common, phlogopite	Common, phlogopite	Common, phlogopite
Microcrysts	Rare, phlogopite	Common, phlogopite	Common, phlogopite	Common, phlogopite
Groundmass	Common, phlogopite - kinoshitalite laths	Common, phlogopite - kinoshitalite laths	Common, phlogopite - tetraferriphlogopite (poikilitic plates)	Common, phlogopite - tetraferriphlogopite (poikilitic plates)
Spinel	Abundant, Mg-chrome to Mg-ulvosinel (Trend 1), atoll spinel is common	Abundant	Minor to rare, Mg-chrome to Ti-magnetite (Trend 2)	Minor to rare, Mg-chrome to Ti-magnetite (Trend 2)
Carbonate	Common calcite, rare dolomite	Common calcite, rare dolomite	Common calcite, rare dolomite	Absent

Table 1. *Continues*

	Kimberlites	Orangeites		Lamproites
		Unevolved	Evolved	
Diopside	Primary diopside is absent, may occur as a secondary phase (in contaminated groundmass)	Common to absent, Microcrysts	Common	Common
Monticellite	Common, may be pseudomorphed by carbonate	Common, may be pseudomorphed by carbonate	Absent	Absent
Apatite	Common to rare	Common to rare	Common	Common
Perovskite	Common	Rare	Rare	Rare
Serpentine	Abundant, secondary and primary segregations	Common, secondary	Common, secondary	Common, secondary
Melilite	Common	Common	Common	Absent
K-richterite	Absent	Absent	Common, groundmass	Common, groundmass
Leucite	Absent	Absent	Common, groundmass	Common, groundmass
Sanidine	Absent	Absent	Common, groundmass	Common, groundmass
Mn-ilmenite	Rare	Rare	Common	Common
Aegirine	Absent	Absent	Common, groundmass	Common, groundmass
K-Ba hollandite	Rare	Rare	Common	Common
Zr-silicates	Rare	Rare	Common	Common
Barite	Rare	Rare	Common	Common

2.2.2 Mineral chemistry

The compositional variations of minerals such as spinel and phlogopite are useful when discriminating kimberlites from lamproites and other ultrapotassic rocks (e.g., Mitchell, 1995; Roeder and Schulze, 2008; Shaikh et al., 2018; Howarth and Giuliani, 2020; Dalton et al., 2019; Mitchell et al., 2019). Lamproites are characterised by phlogopite that ranges in composition from phlogopite to tetraferriphlogopite (tetraferriphlogopite is uncommon in kimberlites) (e.g., Mitchell, 1995). Kimberlites are characterised by spinel with compositional zoning from Mg-chromite to Mg-ulvöspinel-magnetite, whereas lamproites contain Mg-chromite to Ti-magnetite spinel (e.g., Mitchell, 1995; Roeder and Schulze, 2008). However, there are many examples where mica and spinel that are unlike typical kimberlites do occur in bona-fide kimberlites (e.g., Premier, Jagersfontein, Tongo) (e.g., Taylor, 1998; Mitchell, 1995).

Phlogopite

To assess the compositional variation of phlogopite, major elements Al_2O_3, FeO and TiO_2 are analysed, and their relationships are then plotted on variation diagrams. As shown in Fig. 4, the phlogopite composition of kimberlites is characterised by enrichment (relative to orangeites and lamproites) in Al_2O_3 (from the core to rim) without significant variation in TiO_2 and FeO. The phlogopite in lamproites and orangeites show depletion (in comparison to kimberlites) in Al_2O_3 (from the core to rim) with a constant increase in TiO_2 and FeO.

Spinel

The compositional variation of spinel in kimberlite and lamproites can be used to distinguish these two rock types (e.g., Roeder and Schulze, 2008). This variation in composition is a result of major growth stages and zoning trends during the crystallisation of spinel (e.g., Roeder and Schulze, 2008). Mitchell (1986) and Roeder and Schulze (2008) identified six spinel stages and eight zoning trends. These are:

- Xenocrystic spinel (Xen) – the earliest spinel grains derived from peridotitic material.
- Metasomatized xenocryst peridotite spinel (Xen´)
- Chromite spinel (Chr) – small grains that usually dominate the groundmass. The first (primary) spinel to form directly from the kimberlitic/lamproitic magma.
- Pleonaste spinel (Ple)
- Magnesio – ulvöspinel – magnetite (MUM) spinel
- Magnetite spinel (Mag)

The Xen spinel is entrained during the ascent of a kimberlitic magma to the Earth's surface (Mitchell, 1986; Roeder and Schulze, 2008). The exposure of Xen spinel to the kimberlite magma results in overgrowth by Chr spinel and the majority of Chr spinel evolves to MUM and Mag spinels (e.g., Mitchell, 1986; Roeder and Schulze, 2008). Mitchell (1986) and Roeder and Schulze (2008) identified Chr to MUM and Chr to Mag zoning patterns as Trend 1 and Trend 2, respectively.

Titanium and chromium (reduced prism) or ferric iron (oxidised prism) are used as vertical axes to build spinel prisms that show the compositional variation of spinel (e.g., Roeder and Schulze, 2008). These spinel prisms are usually projected onto the three bounding planes (e.g., Roeder and Schulze, 2008) because it is difficult to visualise the spinel variations in a 3D prism (e.g., Mitchell, 1986). Two trends (trend 1 and trend 2) describe how ferric iron (Fe^{3+}; Fig. 5a) and chromium (Cr; Fig. 5b) ratios behave relative to ferrous iron (Fe^{2+}) ratios during Chr-MUM and Chr-Mag growth stages of spinels in different diamondiferous rock types (e.g., Mitchell, 1986; Roeder and Schulze, 2008). Kimberlites and lamproites are associated with trend 1 and trend 2, respectively (e.g., Mitchell, 1986; Roeder and Schulze, 2008).

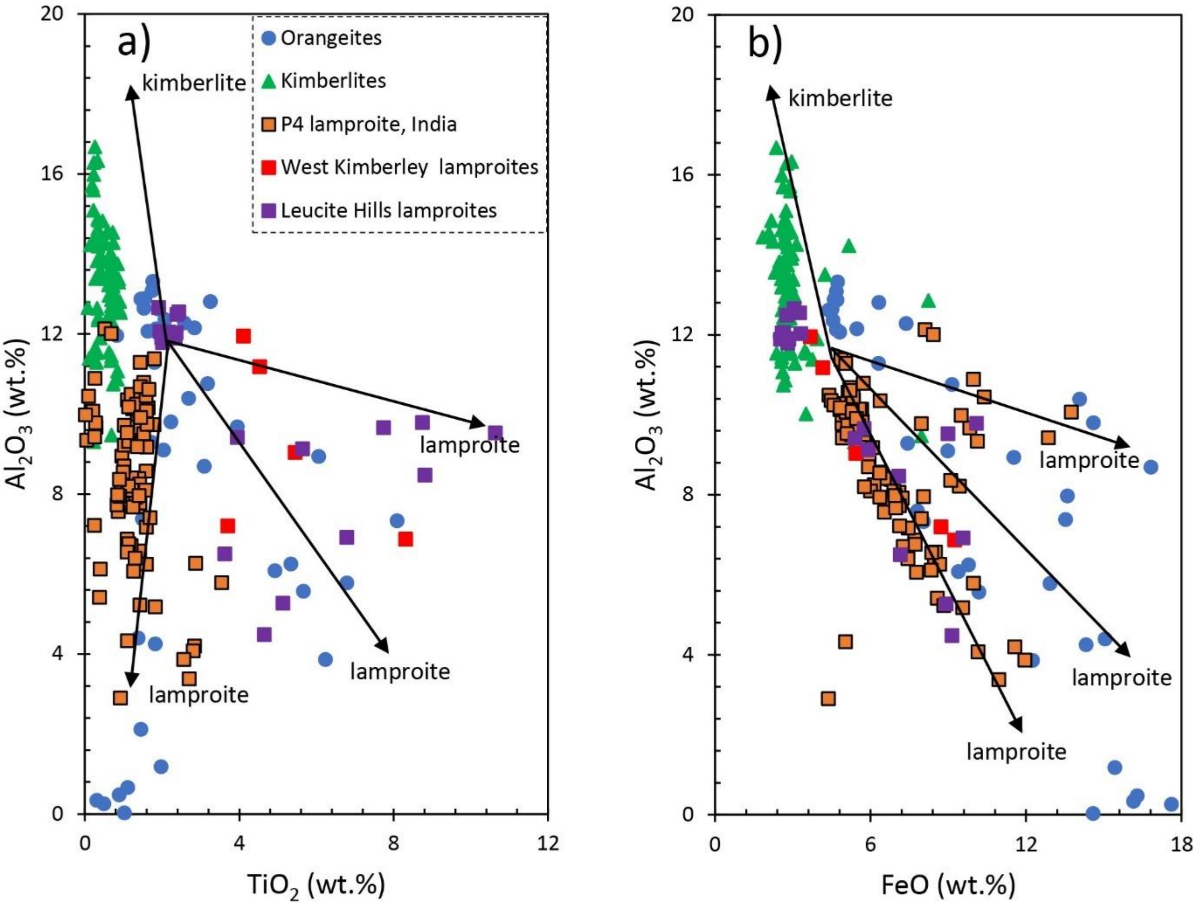

Fig. 4. Graphs showing compositional variations of phlogopite for major elements Al_2O_3, FeO and TiO_2 in kimberlites, lamproites and orangeites. (a) Al_2O_3 vs TiO_2. (b) Al_2O_3 vs FeO. The phlogopite literature data are from; kimberlites: P3 kimberlite, India (Shaikh *et al.*, 2018); orangeites: (Mitchell, 1995); lamproites: P4 lamproite, India (Shaikh *et al.*, 2018); West Kimberley and Leucite Hills lamproites (Mitchell and Bergman, 1991).

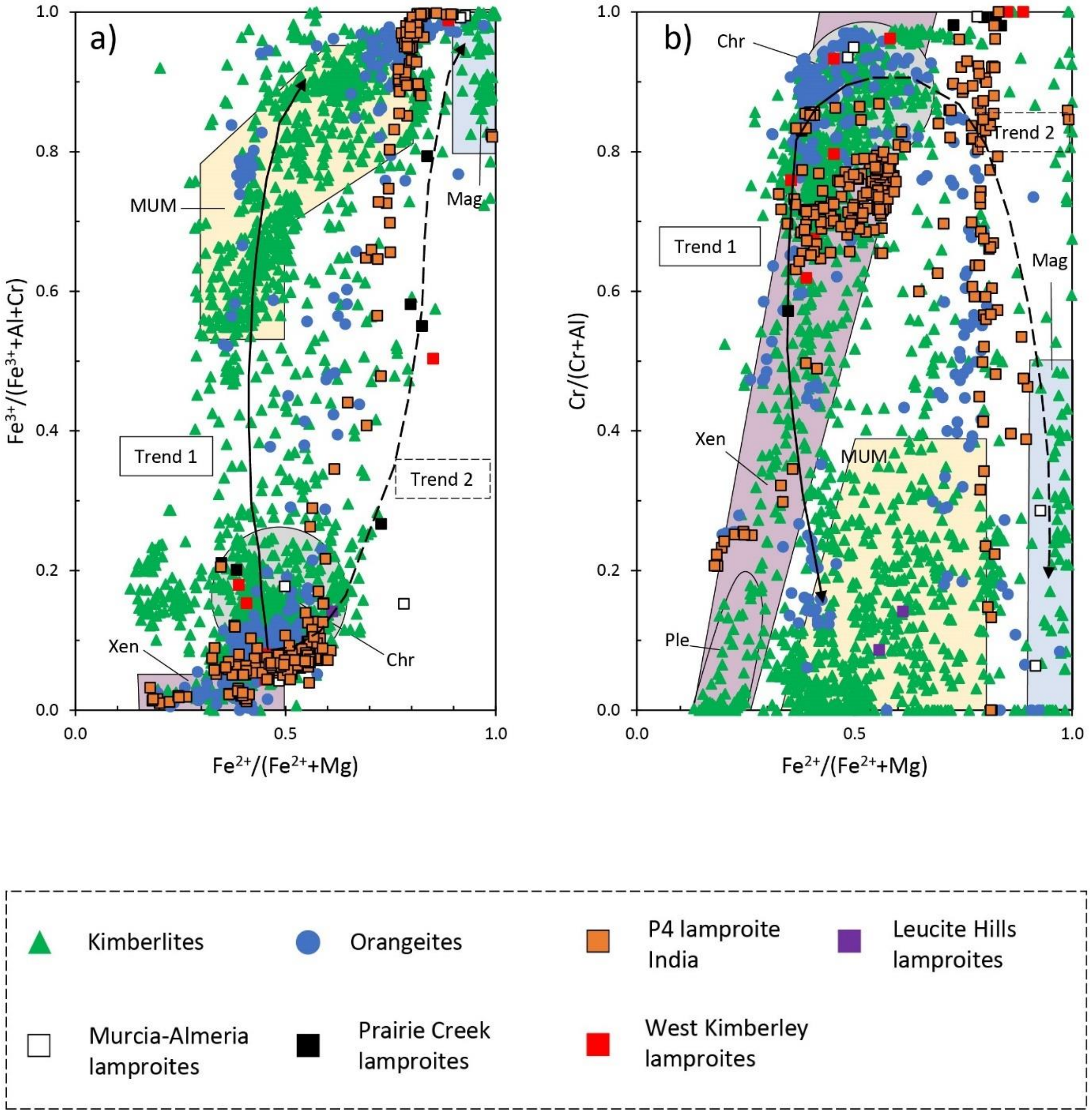

Fig. 5. Compositional variation of spinel in kimberlites, orangeites and lamproites. (a) $Fe^{3+}/(Fe^{3+}+Al+Cr)$ vs $Fe^{2+}/(Fe^{2+}+Mg)$ (oxidised spinel prism). (b) $Cr/(Cr+Al)$ vs $Fe^{2+}/(Fe^{2+}+Mg)$ (reduced prism). The spinel literature data are from: kimberlites (Roeder and Schulze, 2008) and P3 kimberlite (Shaikh *et al.*, 2018); orangeites (Roeder and Schulze, 2008); P4 lamproite (Shaikh *et al.*, 2018); Leucite Hills, Murcia-Almeria, Prairie Creek and West Kimberley lamproites (Mitchell and Bergman, 1991).

2.2.3 Geochemistry

Kimberlites

Kimberlites show a wide range in their major element contents and are enriched in incompatible trace elements (e.g., Mitchell, 1995; Becker and le Roex, 2006). In comparison to orangeites and lamproites, kimberlites are typically enriched in MgO (due to abundant olivine mega/macrocrysts) and TiO_2 (due to abundant groundmass Ti-rich spinel and perovskite) but depleted in K_2O (reflective of the mica-poor nature) and SiO_2 contents (e.g., le Roex et al., 2003; Harris et al., 2004; Becker and le Roex, 2006)

Kimberlites are highly enriched in incompatible trace elements. Kimberlites show smooth sub-parallel chondrite normalised REE patterns (Fig. 7a) and enrichment in light REE relative to heavy REE (e.g., LREE; La ~ 300 – 1400 × chondrite, HREE; Lu ~ 4 – 10 × chondrite. La/Yb_N ~ 45 – 267). Kimberlites show smooth sub-parallel primitive mantle normalised trace element patterns (Fig. 7b) and strong enrichment in highly incompatible elements (e.g., Nb; ~ 150 – 600 × primitive mantle) with HREE showing the least enrichment (e.g., Er to Lu; ~ 1 – 2 × primitive mantle). Kimberlites are characterised by depletion (negative anomaly) in Rb, K, Sr, Hf-Zr and Ti. The negative Rb and K anomalies tend to be the largest and partial melting in the presence of carbonate more than zircon megacryst fractionation results in a strong negative Hf-Zr anomaly (e.g., Becker and le Roex, 2006).

The La/Yb, Gd/Yb and La/Sm ratios of kimberlites typically fall within the ranges 62.3 – 373, 6.67 – 20.6 and 6.64 – 11.2, respectively (Fig. 8a & b). In comparison to orangeites, kimberlites are typically characterised by lower Ba/Nb (<11.5), La/Nb (<1.10) and higher Ce/Pb (>22) ratios (Fig. 8c & d).

The Sr-Nd isotopic composition was primarily used to distinguish kimberlites from orangeites (and lamproites) (e.g., Smith, 1983). In comparison to orangeites and lamproites, kimberlites are characterised by positive εNd_i and lower initial $^{87}Sr/^{86}Sr$ ratios (~ 0.70328 to 0.70537) (Fig. 9; however, this only applies to southern African Cretaceous occurrences) (Smith, 1983; Becker and le Roex, 2006).

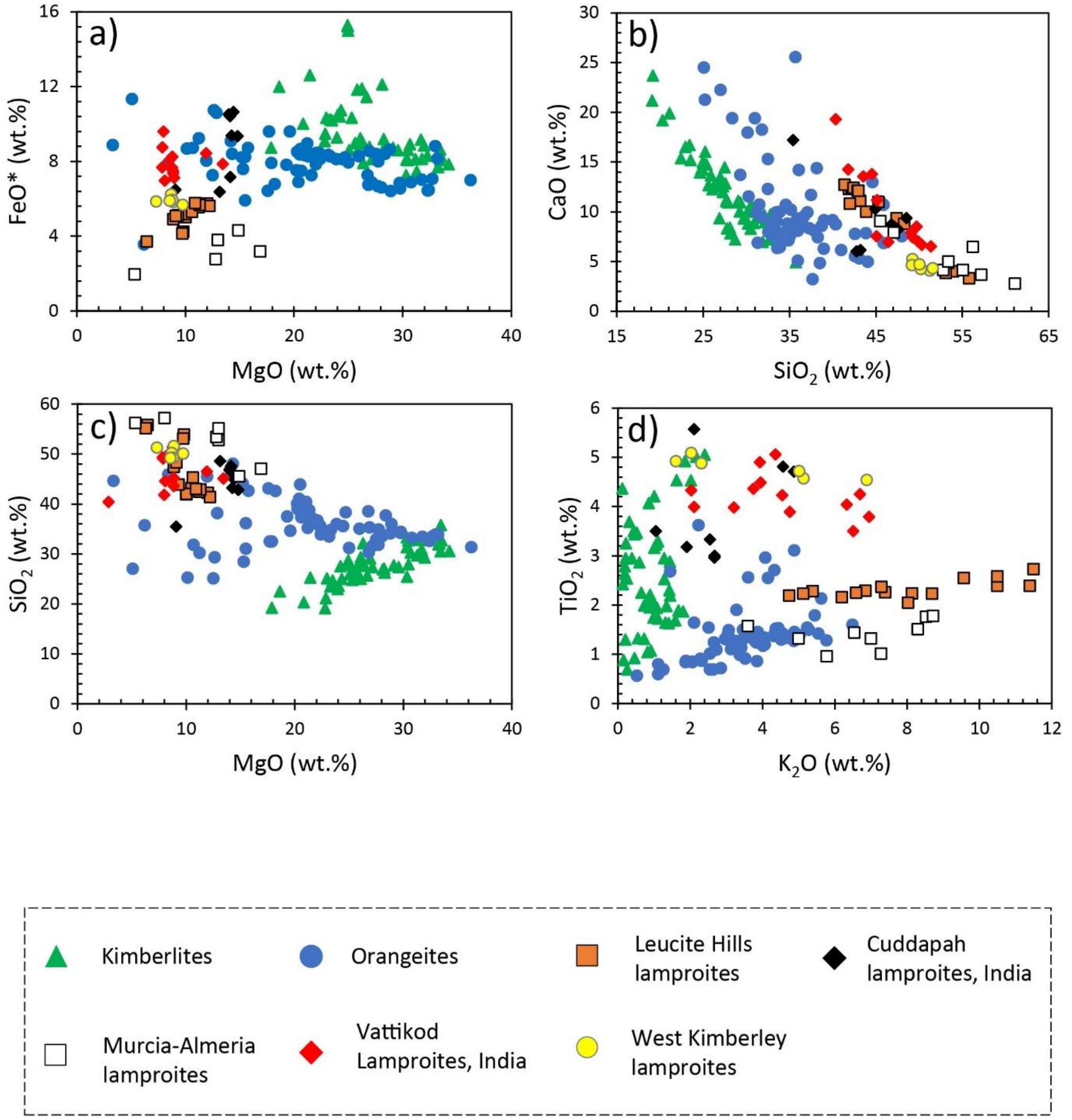

Fig. 6. Compositional variation of some major elements in kimberlites, orangeites and lamproites. (a) FeO* (recalculated Fe^{2+} from Fe_{total}) vs MgO (b) CaO vs SiO_2 (c) SiO_2 vs MgO and (c) TiO_2 vs K_2O. The bulk-rock literature data are from: kimberlites (Becker and Le Roex, 2006; Harris *et al.*, 2004; le Roex *et al.*, 2003); orangeites (Becker and le Roex, 2006; Coe et al., 2008; Howarth et al., 2011); Leucite Hills lamproites (Mirnejad and Bell, 2006); Cuddapah lamproites, India (Chalapathi Rao et al., 2004); Murcia-Almeria lamproites (Mitchell and Bergman, 1991); Vattikod lamproites, India (Talukdar et al., 2018); West Kimberley lamproites (Hwang et al., 1994).

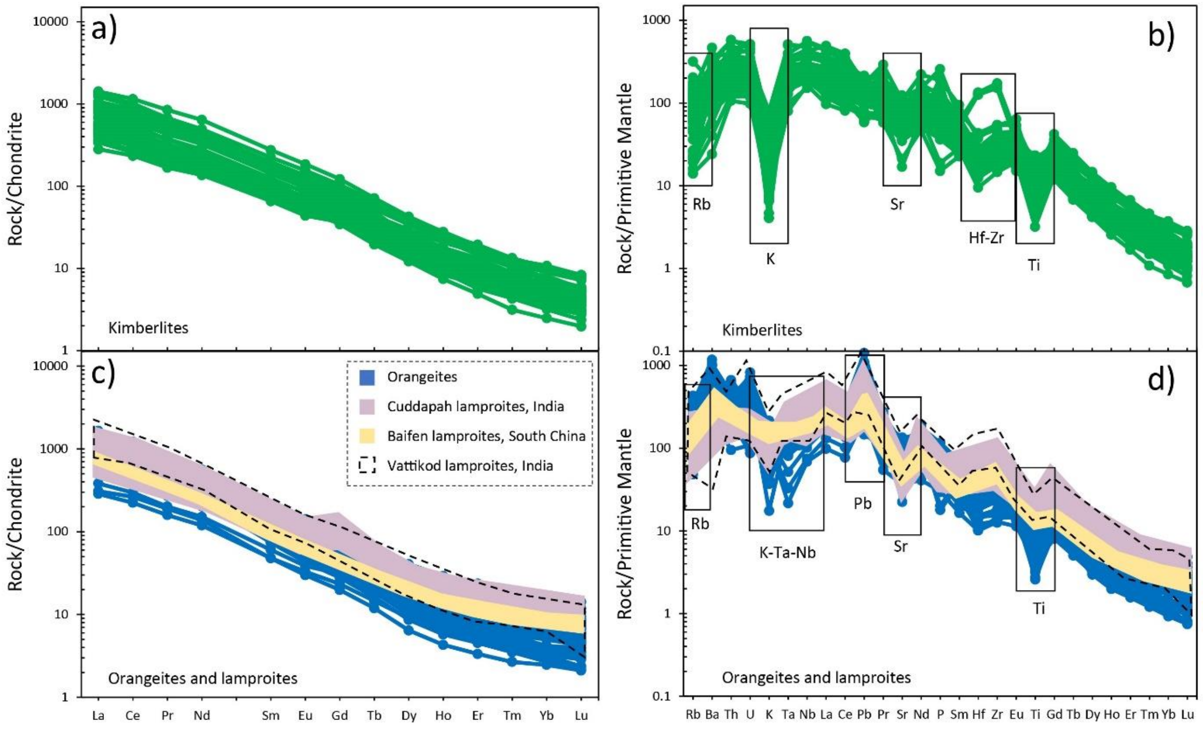

Fig. 7. Chondrite-normalised REE (kimberlites; plot a; orangeites and lamproites; plot c) and Primitive mantle-normalised trace element (kimberlites; plot b; orangeites and lamproites; plot d) patterns, normalised to the values of Sun and McDonough (1989) . The bulk-rock literature data are from: kimberlites (le Roex et al., 2003; Harris et al., 2004; Becker and le Roex, 2006); orangeites (Becker and Le Roex, 2006; Coe *et al.*, 2008); Cuddapah lamproites, India (Chalapathi-Rao *et al.*, 2004); Baifen lamproites, South China (Xiang et al., 2020); Vattikod lamproites, India (Talukdar et al., 2018).

Orangeites and lamproites

Lamproites and orangeites exhibit somewhat similar geochemical characteristics, which are different from those of kimberlites. The similarity in their (orangeites and lamproites) major and trace element composition is demonstrated in Fig. 6, 7 & 8. For example, in comparison to kimberlites, both orangeites and lamproites are typically enriched in K_2O (reflective of the mica-rich nature) and SiO_2 (e.g., Mitchell and Bergman, 1991; Chalapathi Rao et al., 2004; Becker and le Roex, 2006; Mirnejad and Bell, 2006; Coe et al., 2008; Xiang et al., 2020) (Fig. 6). The SiO_2 correlates negatively with CaO and the K_2O content correlates positively with TiO_2. Additionally, both orangeites and lamproites show smooth sub-parallel chondrite normalised REE patterns (Fig. 7c) and enrichment in light REE relative to heavy REE (e.g., LREE; La ~ 300 – 1600 × chondrite, HREE; Lu ~ 2 – 10 × chondrite. La/Yb_N ~ 44 – 300). The primitive mantle normalised trace element patterns (Fig. 7d) are sub-parallel and show strong enrichment in highly incompatible elements (e.g., Nb; ~ 110 – 800 × primitive mantle) with HREE showing the least enrichment (e.g., Er to Lu; ~ 1 – 2 × primitive mantle). Both orangeites and lamproites are characterised by negative Rb, K-Ta-Nb (instead of K as observed in kimberlites), Sr and Ti anomalies, as well as a positive Pb anomaly (not observed in kimberlites). Due to the absence of zircon megacrysts in orangeites and lamproites, the strong Hf-Zr anomaly is not observed (e.g., Becker and le Roex, 2006).

However, lamproites can show significant compositional variation from craton to craton. For example, the West Kimberley lamproites and Indian lamproites (Vattikod lamproites; Cuddapah lamproites) are enriched in TiO_2 relative to orangeites, Leucite Hills and Murcia-Almeria lamproites (Fig. 6d). Orangeites together with Vattikod, Cuddapah and West Kimberley lamproites contain similar trace element ratios (e.g., higher La/Sm ~ 9.07 – 19; Ba/Nb ~ >11.5; La/Nb ~ >1.10; and lower Gd/Yb ~ 3.50 – 16; Ce/Pb ~ <22, in comparison to kimberlites). Notably, the Leucite Hills lamproites contain much higher trace element ratios (e.g., Ba/Nb ~ 53 – 168; La/Nb ~ 2.36 – 4.10; Gd/Yb ~ 14.4 – 43.9), in comparison to orangeites, kimberlites and the above-mentioned lamproites (Fig. 8).

In contrast to kimberlites, both orangeites and lamproites are characterised by negative εNd_i and higher initial $^{87}Sr/^{86}Sr$ ratios (orangeites ~ 0.70720 – 0.71050; Leucite Hills lamproites ~ 0.70556 – 0.70586; Prairie Creek lamproites ~ 0.70670 – 0.70700; Vattikod lamproites, India ~ 0.70370 – 0.70870). However, the significant compositional variation within the lamproite clan is additionally observed in the strontium isotopic composition. The West Kimberley lamproites contain much higher initial $^{87}Sr/^{86}Sr$ ratios (0.71100 – 0.72070), relative to orangeites and the above-mentioned lamproites (Fig. 9).

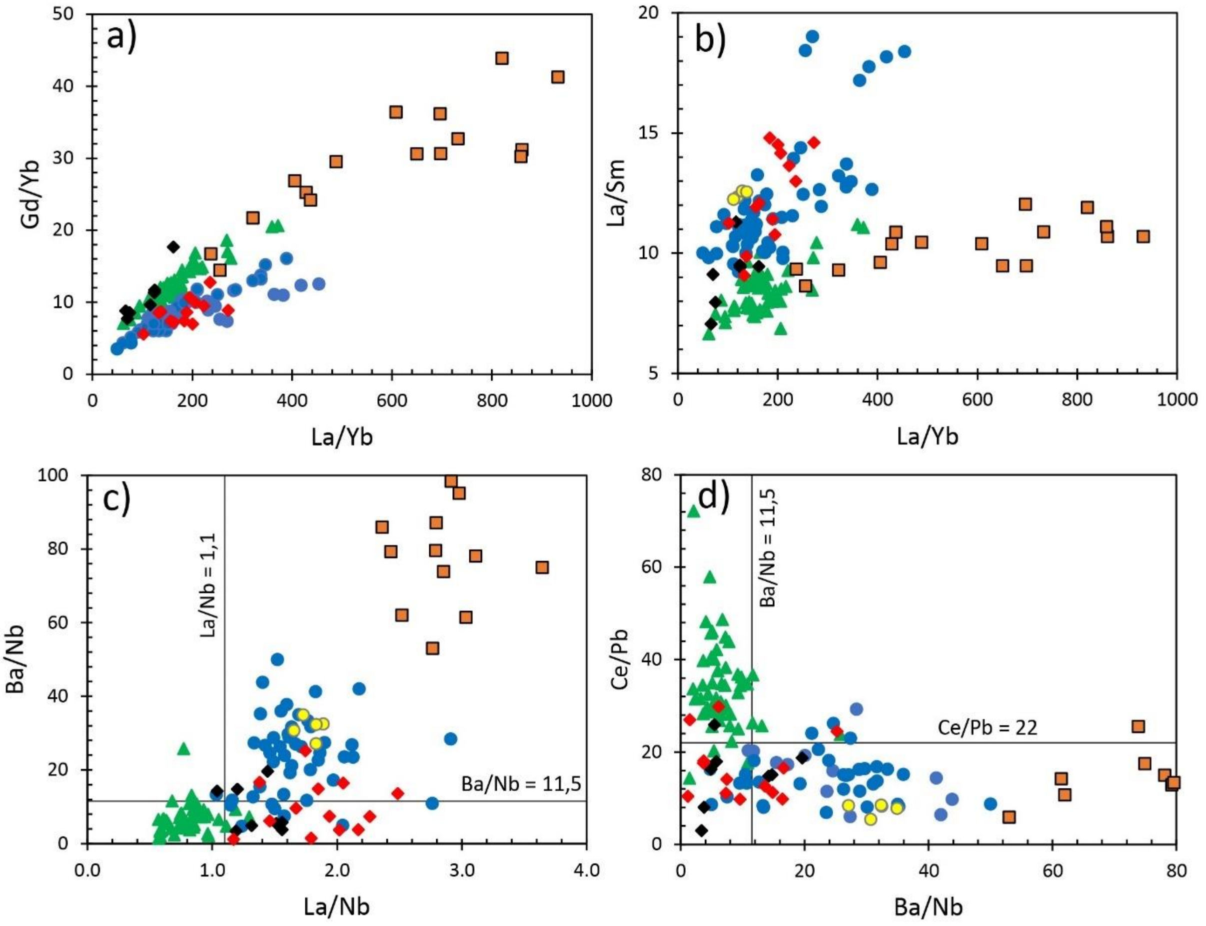

Fig. 8. Compositional variation of some trace element ratios in kimberlites, orangeites and lamproites. (a) Gd/Yb vs La/Yb (b) La/Sm vs La/Yb (c) Ba/Nb vs La/Nb and (c) Ce/Pb vs Ba/Nb. The legend and literature where the bulk-rock data were taken from, are the same as in **Fig. 6.**

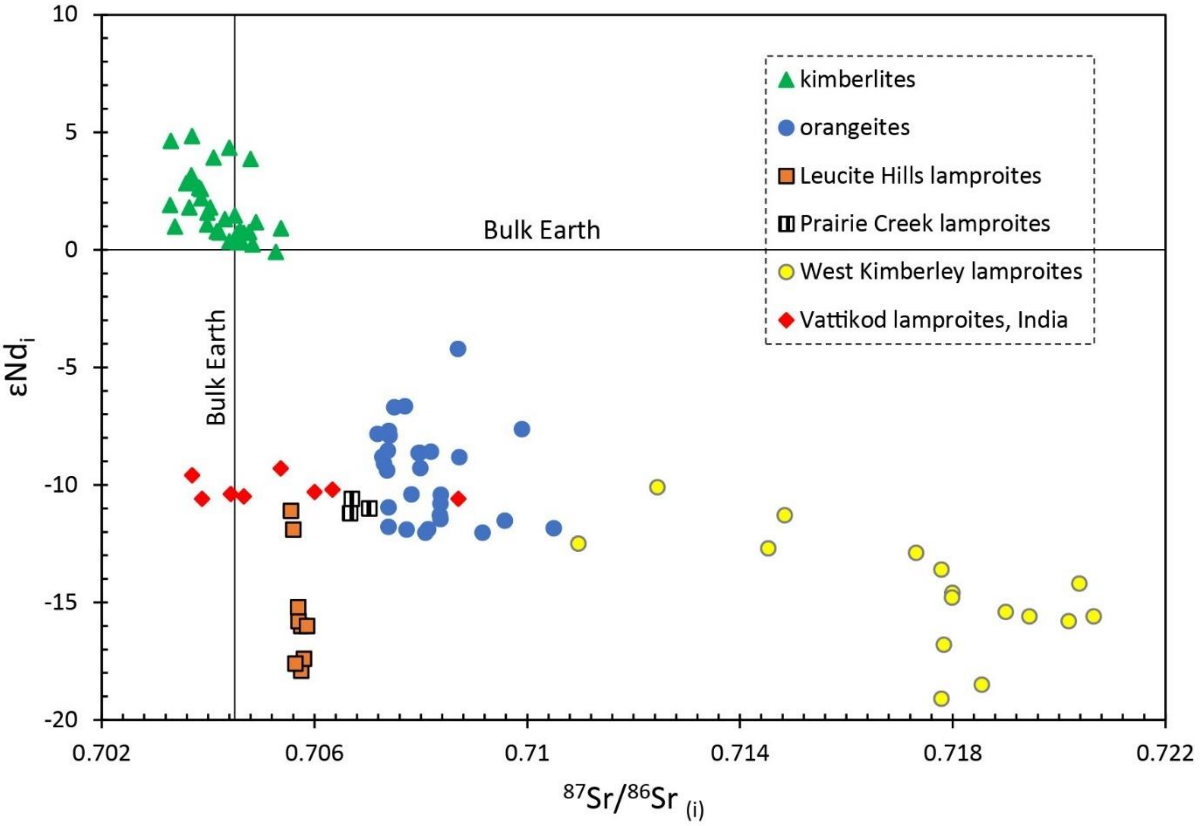

Fig. 9. Variation of Sr-Nd isotopic composition in kimberlites, orangeites and lamproites. The εNd$_i$ is plotted against the initial $^{87}Sr/^{86}Sr$ ratio. The Sr-Nd isotopic composition literature data are from: kimberlites (Becker and Le Roex, 2006; Smith, 1983); orangeites (Becker and Le Roex, 2006; Coe *et al.*, 2008; Smith, 1983); Leucite Hills, Prairie Creek and West Kimberley lamproites (Fraser, 1988); Vattikod lamproites, India (Talukdar *et al.*, 2018).

2.3 West African diamondiferous rocks

2.3.1 Distribution and local geology

The Man Craton is located in the southern part of the West African Shield and was formed during the Archaean (e.g., Haggerty, 1982). In the Mesozoic (~ 140 Ga), the Craton was rifted apart during the opening of the Atlantic Ocean, and its counterpart, the Guyana Craton, is found in South America (e.g., Haggerty, 1982; Skinner *et al.*, 2004). The Man Craton consists of Archaean granitic-gneiss basement rocks together with multiple

Paleoproterozoic domains made of greenstone belts, sedimentary basins, regional granitoid-tonalite-trondhjemite-granodiorite (TTG) plutons, and large shear zones (e.g., Skinner *et al.*, 2004; Taylor *et al.*, 1994). The craton is overlain by Neoproterozoic and younger sedimentary basins (e.g., Taylor *et al.*, 1994).

The Man Craton consists of numerous primary diamond deposits with characteristics similar to those of kimberlites and lamproites (e.g., Howarth and Giuliani, 2020; Skinner *et al.*, 2004; Taylor *et al.*, 1994). The kimberlites/lamproites that have been discovered in the Man Craton include a total of seven Jurassic-aged clusters (Koidu and Tongo clusters in Sierra Leone; Banankoro, Bouro and Droujba clusters in Guinea; Kumgbo and Mano Godua clusters in Liberia), and one Neoproterozoic-aged cluster (Weasua cluster in Liberia) (e.g., Skinner *et al.*, 2004) (Fig. 1). The exact age of the Camp Alpha cluster is unknown, however, Haggerty (2017) suggested that it might be Precambrian-aged. The West African kimberlites/lamproites are predominately dikes whereas pipes are less common. The dikes are noted in two distinct orientations that have been termed the Sierra Leone trend (i.e., Koidu and Tongo dikes) and the Liberian trend (i.e., Camp Alpha dike). The trends are different in ages and associated with fracture structures that were reactivated during Mesozoic (Sierra Leone trend) and Precambrian (Liberian trend) events (e.g., Haggerty, 2017).

There has been a large amount of diamond mining activity within the Man Craton. The West African diamonds contribute one per cent towards global production. West Africa consists of both alluvial and *in situ* primary diamond deposits, located mainly in Ghana, Sierra Leone, Guinea, Liberia, and Tongo. In Liberia, the alluvial placers are the only sources of diamonds and about fourteen million carats of diamonds have been produced over the last 50 years. This region is still under exploration and more diamond sources may be discovered in the future (Haggerty, 2017).

2.3.2 Mineralogy

Liberia

Kimberlite pipes and dikes have recently been described by Haggerty (2017) in Camp Alpha, NW Liberia, and the region is still under exploration. These Camp Alpha rocks exhibit a range of textures (Haggerty, 2017). The kimberlite pipes are mostly hypabyssal facies, and the dikes range from aphanitic to coarse-grained macrocrystic rocks (Haggerty, 2017). The dikes in the Camp Alpha region are characterised by xenoliths/xenocrysts of ilmenite, pyroxene, eclogites, altered fragments of harzburgite, and intergrowths of ilmenite-clinopyroxene (Haggerty, 2017).

Taylor *et al.* (1994) described Liberian diamondiferous rocks but mainly focused on samples collected from the Sample Creek pipe (as part of the Camp Alpha cluster). These rocks consist of abundant ilmenite, Cr-poor garnet and clinopyroxene megacrysts, as well as serpentinised olivine macrocrysts occurring in a finer kimberlite groundmass (Taylor *et al.*, 1994). The groundmass includes phlogopite, serpentine, Cr-spinel with titanomagnetite rims and perovskite with magnetite or titanate rims (Taylor *et al.*, 1994).

The Weasua rocks described by Howarth and Giuliani (2020) and Skinner *et al.* (2004) are characterised by olivine and phlogopite macro/microcrysts (Weasua rocks from Howarth and Giuliani (2020) did not contain phlogopite macrocrysts) occurring in a fine-grained groundmass. The groundmass consists of phlogopite, primary diopside, perovskite, apatite, spinel, calcite, and serpentine (Howarth and Giuliani, 2020; Skinner *et al.*, 2004). The Weasua samples described by Skinner *et al.* (2004) contain metasomatic diopside which replaces the primary phases of phlogopite, olivine and perovskite. Skinner *et al.* (2004) classified their rocks as phlogopite kimberlites. The samples described by Howarth and Giuliani (2020) contain magmatic diopside which strongly suggested that the rocks are lamproites. This means that both kimberlites and lamproites are present within the Weasua region.

Sierra Leone

The Koidu (Taylor *et al.*, 1994) and Tongo (Howarth and Giuliani, 2020) dike clusters are phlogopite-rich (similar to orangeites) and consist of aphanitic (<< 5% olivine macrocrysts) and macrocrystic varieties. The Koidu rocks are characterised by olivine (completely replaced by serpentine and calcite) and phlogopite macrocrysts, set in a groundmass of phlogopite, spinel, perovskite and calcite (Taylor *et al.*, 1994). The Tongo rocks are characterised by olivine (relatively fresh) and phlogopite macrocrysts, set in a groundmass of phlogopite, spinel, perovskite, dolomite and calcite (Howarth and Giuliani, 2020). Both Koidu and Tongo dikes are phlogopite-rich but lack monticellite and magmatic diopside, and their classification is not straightforward (e.g., Taylor *et al.*, 1994; Howarth and Giuliani, 2020). They are mineralogically classified as phlogopite-rich kimberlites (Howarth and Giuliani, 2020).

<u>Guinea</u>

The rocks occurring in Guinea (Banankoro, Bouro and Droujba) are macrocrystic kimberlites and are dominated by macrocrysts of serpentinized olivine, ilmenite and rare phlogopite and garnet (Skinner *et al.*, 2004). The macrocrysts are set in a groundmass of phlogopite, apatite, perovskite, calcite, monticellite and serpentine (Skinner *et al.*, 2004). The Guinea area consists of kimberlite occurrences (Skinner et al., 2004).

2.3.3 Geochemistry

Only a few studies on West African kimberlites have been conducted, thus, the geochemical data are limited. Taylor *et al.* (1994) reported the bulk rock geochemistry data for the Sample Creek and Koidu rocks, Skinner *et al.* (2004) for the Weasua rocks, Mathafeng (2021) for the Tongo dike, and Haggerty (2017) for the Camp Alpha rocks. The data from the above-mentioned studies were used to construct co-variation diagrams (i.e., major elements; FeO* vs MgO, CaO vs SiO_2, SiO_2 vs MgO and TiO_2 vs K_2O; Fig. 10a, b, c & d; trace element ratios; Ba/Nb vs La/Nb and Ce/Pb vs Ba/Nb; Fig. 10e & f). The SiO_2, MgO, TiO_2 and CaO major element composition, as well as the Ba/Nb, La/Nb and Ce/Pb ratios of the Koidu, Tongo, Weasua and Camp Alpha rocks are within the ranges that define kimberlites. In comparison to the other West African kimberlites, the Tongo dike contains higher K_2O (within the orangeite range and towards the Murcia-Almeria and Leucite Hills lamproites composition; reflective of mica-rich nature), CaO and lower MgO contents (Fig. 10). In comparison to the other West African kimberlites, the Sample Creek (Taylor *et al.*, 1994) and Camp Alpha (Haggerty, 2017) rocks contain very low K_2O (reflective of mica-poor nature) and CaO contents. However, the Camp Alpha (Haggerty,

2017) rocks contain higher FeO* content relative to the Sample Creek (Taylor *et al.*, 1994) rocks.

No Sr-Nd-Pb isotope geochemistry data have been reported for the Liberian rocks. The Tongo rocks are characterised by positive εNd_i (1.6 – 2.2) and an initial $^{87}Sr/^{86}Sr$ ratio that ranges from 0.70377 to 0.70575 (re-calculated at 140 Ma; Mathafeng, 2021). The two isotopic analyses reported by Taylor *et al.* (1994) for Koidu, have $\varepsilon_{Nd}(t)$ of −0.8 and +3.0 and initial $^{87}Sr/^{86}Sr$ ratios of 0.70391 and 0.70422, respectively (re-calculated at 146 Ma).

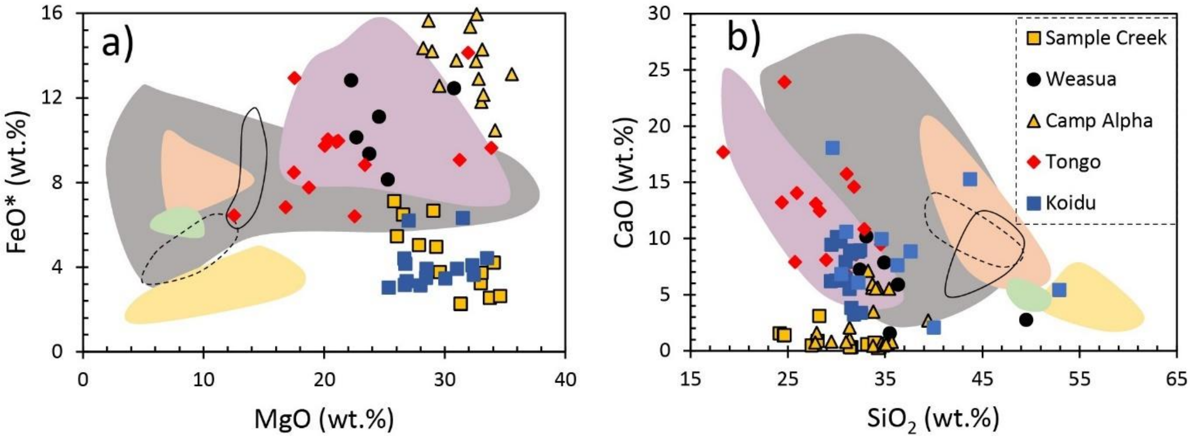

Fig. 10. Compositional variation of some major and trace elements in West African diamondiferous rocks. (a) FeO* (recalculated Fe^{2+} from Fe_{total}) vs MgO (b) CaO vs SiO_2 (c) SiO_2 vs MgO (d) TiO_2 vs K_2O (e) Ba/Nb vs La/Nb and (f) Ce/Pb vs Ba/Nb. The bulk-rock literature data are from: Sample Creek (rocks sampled from the Camp Alpha region) and Koidu (Taylor *et al.*, 1994); Weasua kimberlite (Skinner *et al.*, 2004); Camp Alpha (Haggerty, 2017); Tongo (Mathafeng, 2021). The bulk-rock literature data used to construct the fields are the same as in **Fig. 6**.

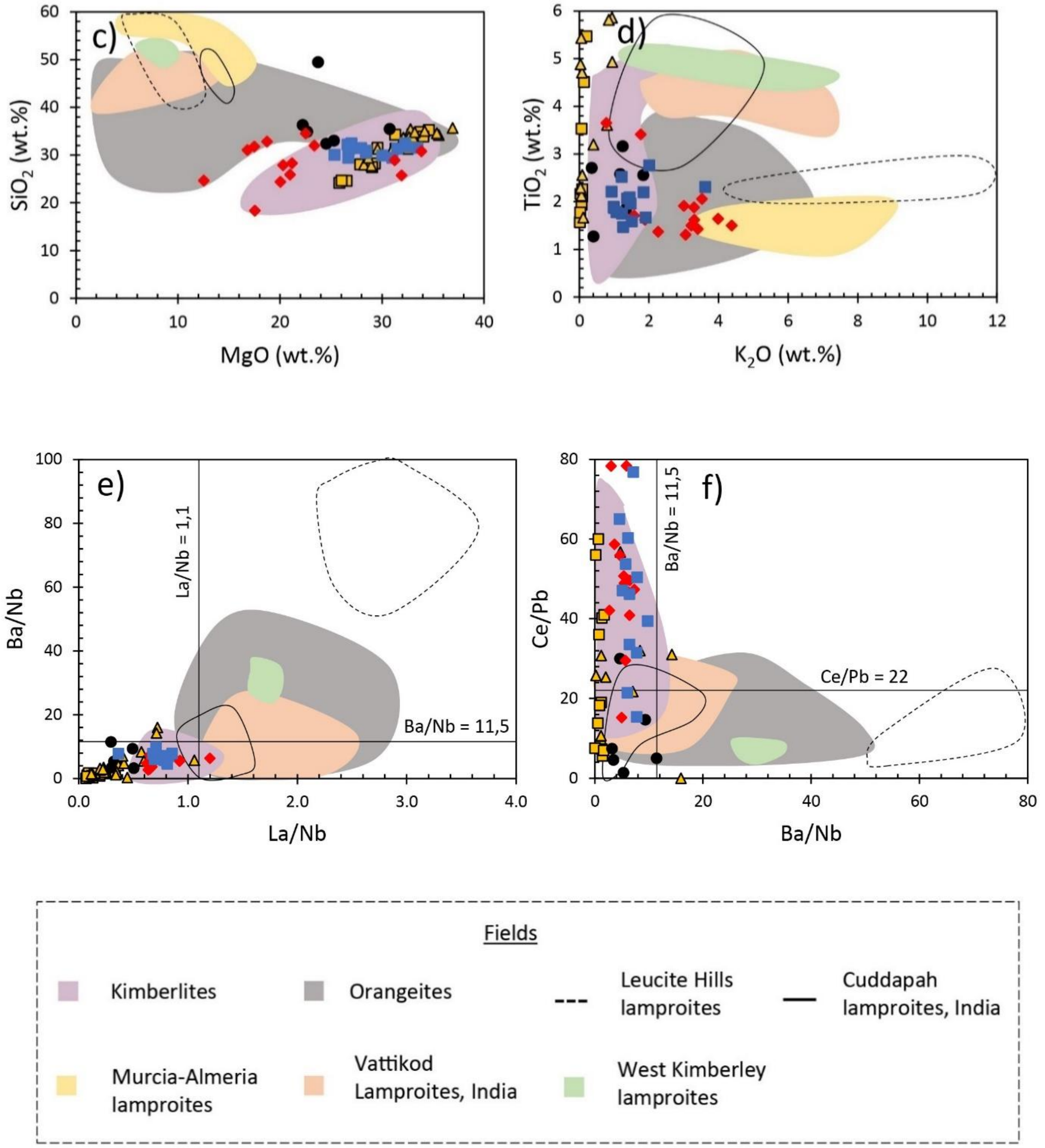

Fig. 10. *Continues*

CHAPTER 3: Samples and analytical techniques

3.1 Sample collection and preparation

A total of 15 representative samples from the Camp Alpha cluster were obtained from Professor Steve Haggerty (i.e., ten dike samples in the form of fragments and small chips; SC11 A1, SC11 A2, SC11 A4b, SC11 A6, SC11 B1, SC11 B2, SC11 B3b, SC11 B4, SC11 B5 and SC11 B6a, and five pipe samples in the form of fragments; SC80 2-1, SC80 3-2, SC80 5-2, SC80 8-2 and SC80 14-1). The samples were collected from 8 dikes (~ 10 m wide) and one *en echelon* pipe discovered by Haggerty (2017). The 8 separate dikes and one pipe were recovered in the Gola National Forest, Camp Alpha, NW Liberia. A thin section (4.5 cm long and 2.5 cm wide) for each representative Camp Alpha sample, was prepared at the University of Cape Town. The Camp Alpha representative thin sections were examined using a Zeiss Petrographic Microscope, housed at the University of Cape Town.

For bulk-rock geochemical analyses, small chips of fresh rock samples (each mm sized) were handpicked to carefully avoid any contamination by ilmenite macrocrysts (as they are abundant) and crustal xenoliths (less abundant to absent in most samples). The handpicked fresh rock grains were then crushed using a Siebtechnik carbon steel swing mill, producing 20 to 25 g of powder.

A suite of 8 samples (i.e., Y5747, Y5752, Y5755, Y5759, Y5767, 2-10-3, 2-12-2 and 2-12-3) collected from a coherent rock body from the Weasua cluster, were obtained from Mike Skinner. The exact location from where these samples were collected within the Weasua region, is unknown. Two fresh representative samples, Y5747 and Y5759, were selected from the suite for perovskite analysis in this study. Only thin sections were obtained and no rock samples were available for the Weasua samples.

3.2 Electron probe micro analysis (EPMA)

Phlogopite and spinel analyses

The Camp Alpha phlogopite and spinel analyses were conducted at the University of Johannesburg using a Cameca SX 100 Electron Microprobe that is equipped with four wavelength dispersive spectrometers. The following analytical conditions were common for both phlogopite and spinel analyses: Calibration standards; Na (Kα, jadeite), Mg (Kα, olivine), Al (Kα, almandine), Si (Kα, diopside), K (Kα, orthoclase), Ti (Kα, TiO_2), Cr (Kα, Cr_2O_3), Mn (Kα, rhodonite), Fe (Kα, hematite), Ca (Kα, wollastonite) and beam accelerating voltage of 15 kV.

The beam current for the phlogopite analysis was 15 nA, with a beam diameter of 2 μm and the on-peak counting time per element of 10 – 50 s, depending on the element. The elements, F (Kα, fluorite), Cl (Kα, NaCl), Ca (Kα, wollastonite) and Ba (Lα, barite), were used in addition (to the common elements mentioned above) for calibration. The beam current for the spinel analysis was 20 nA, with a beam diameter of 1 μm and the on-peak counting time per element was 30 s. The element Ni (Kα, NiO) was used in addition (to the common elements mentioned above) for calibration.

Perovskite analysis

Perovskite analysis was performed for the two Weasua samples, Y5747 (11 grains analysed) and Y5759 (12 grains analysed). Analysis for perovskite major elements was conducted at the University of Cape Town using a JEOL Superprobe JXA-8100 Electron Microprobe that is equipped with four wavelength dispersive spectrometers, a range of crystals (LDE1, LDE2, PETJ, PETH, TAP, LIF, LIFH), fitted with two gas-flow proportional and two sealed Xenon detectors. The electron beam was set to an accelerating potential of 15 kV, a beam current of 20 nA, and a diameter of 1-3 μm. Measurements were performed with counting times of 10 seconds on peak and 2 x 5 seconds on the background. The following standards were used for calibration: Pyrope (Si, Al, Fe), Ce Metal (Ce), La Metal (La), Rhodonite (Mg), Rutile (Ti), Clinopyroxene (Ca), Chromite (Ni), Hornblende (Na).

3.3 Inductively coupled plasma-mass spectrometry (ICP-MS) analysis

A total of 10 representative samples from Camp Alpha (i.e. SC11 A1, SC11 A2, SC11 A4, SC11 A6, SC11 B1, SC11 B2, SC11 B3b, SC11 B4, SC11 B5 and SC11 B6) plus the SARM-39 standard, were analysed for a suite of trace element (e.g., Li, Sc, Sr, Zr, the 14 REE, Hf, Pb, Th, U etc.) concentrations using the Thermo Fisher iCAP-RQ quadrupole ICP-MS, housed in the Department of Geological Sciences at the University of Cape Town. To prepare the samples to be analysed, 0.05 g of sample powder was weighed out into 3 ml Teflon vials to which 2 ml of a 4:1 mixture of concentrated hydrofluoric (HF) and nitric acids (HNO_3) were added. The Teflon vial was capped and placed into a Teflon capsule of a steel Parr digestion vessel. In order to decrease the pressure difference between the outer Teflon and inner Teflon vials, 2 ml of pure water was added to the outer vessel. The digestion vessels were firmly sealed and put into a 200°C oven for a period of 24 hours to allow for complete digestion. After 24 hours, the 3 ml Teflon vial was removed from the capsule and the cap was carefully removed. The vial was put on a hot plate of 100°C to allow the acid mixture to evaporate, followed by the addition and subsequent evaporation of 2 ml of pure nitric acid (HNO_3). The samples were then diluted using a stock solution of 5% HNO_3. In, Re, Rh and Bi were used as internal standards. Calibration curves were obtained from standards made from synthetic solutions.

3.4 Sr and Nd isotope analysis

The Sr and Nd elemental separation and isotope analyses of the Camp Alpha samples were performed as per Howarth et al. (2019). The analyses were performed using the Nu Instruments NuPlasma HR Multicollector Inductively Coupled Plasma Mass Spectrometer (HR MC-ICP-MS) housed in the Department of Geological Sciences at the University of Cape Town. To prepare the samples, about 50 mg of sample powder was digested in concentrated 2M HNO_3 at 140° C for 48 hours in closed 7 ml Teflon beakers.

Subsequently, the samples were dried down and redissolved in 1.7 ml of 2M HNO_3 for Sr and Nd elemental separation. To separate Sr and Nd, the sequential column chemistry outlined by Mikova and Denkova (2007) was followed.

The Sr isotope ratios were analysed as 200 ppb 0.2% HNO_3 solutions, using NIST SRM987 and an $^{87}Sr/^{86}Sr$ normalising value of 0.710255 as reference standards. The exponential law and an $^{86}Sr/^{88}Sr$ value of 0.1194 were used for the correction of instrumental mass fractionation. The Nd isotope ratios were analysed as 50 ppb 2% HNO_3 solutions, using JNdi-1 and a $^{143}Nd/^{144}Nd$ normalising value of 0.512115 as reference standards. All Nd isotope data were corrected for Sm and Ce interference using the natural Sm and Ce isotope abundances and measured signals for 147Sm and 140Ce. The exponential law and a $^{146}Nd/^{144}Nd$ value of 0.7219 were used for the correction of instrumental mass fractionation.

3.5 Laser ablation ICP-MS analysis

The concentrations of trace elements for Weasua perovskite grains were analysed using the Thermo-Fisher X-Series II quadrupole ICP-MS with a New Wave UP213 solid-state laser ablation system housed in the Department of Geological Sciences at the University of Cape Town. The following elements were analysed: ^{7}Li, ^{45}Sc, ^{55}Mn, ^{60}Ni, ^{85}Rb, ^{88}Sr, ^{89}Y, ^{90}Zr, ^{93}Nb, ^{137}Ba, ^{139}La, ^{140}Ce, ^{141}Pr, ^{144}Nd, ^{152}Sm, ^{153}Eu, ^{159}Tb, ^{160}Gd, ^{163}Dy, ^{165}Ho, ^{166}Er, ^{169}Tm, ^{174}Yb, ^{175}Lu, ^{178}Hf, ^{181}Ta, ^{208}Pb, ^{232}Th and ^{238}U. The standard bracketing was carried out using the calibration materials (NIST 612 and 610) measured at the beginning and the end of each session, and at regular intervals during the session (after ~12 analyses). Helium gas was used as a carrier, while Argon gas was used as the plasma. The laser beam settings for all spots were as follows: beam size - 40 microns, frequency - 10Hz, and fluence - ~24 J/cm^2. The reduction of the data was carried out using the Thermo Plasma Lab software, and ^{49}Ti was used at the internal standard.

CHAPTER 4: Results

4.1 Rocks from Camp Alpha

To obtain precise modal abundances of minerals, point counting (300 points per sample) was performed using a mechanical point counting stage mounted to a petrographic microscope. The modal abundances are shown in Table 2. The phases that form part of the interstitial material (i.e., calcite, serpentine) are fine-grained and difficult to tell apart in most samples, thus were grouped together during point counting as interstitial material.

In the following petrographic descriptions, the terms macrocryst, microcryst and groundmass are used to describe the mineral grain sizes. Macrocryst refers to a grain that is > 0.5 mm in size. Microcryst and groundmass refer to grains that are 0.5 – 0.3 mm and < 0.3 mm in size, respectively.

4.1.1 Petrography

Dike samples

The Camp Alpha dike samples contain euhedral olivine macrocrysts (up to 11 mm), subhedral-anhedral microcrysts (0.32 to 0.36 mm) and rounded ilmenite macrocrysts (1.48 to 4 mm), set in a finer groundmass (Fig. 11a). The olivine macrocrysts and microcrysts are completely altered and pseudomorphed by serpentine and are recognised by grain morphology only (Fig. 11b). Some of the microcrysts are barely distinguishable from the groundmass and are part of the calcite-serpentine interstitial material. As a result, the macrocryst and microcryst abundance ranges from 27 to 63 vol.%, and the lower range might be underestimated where alteration content is high and microcrysts blend into the interstitial material. The olivine macrocrysts are rounded and elongated whereas the microcrysts occur as sub-rounded grains. The ilmenite macrocrysts (2 – 8 vol.% for most samples and two samples contain a high 11 and 17 vol.%, i.e., SC11 A4b and SC11 B3b, respectively) are opaque and rounded in shape. In reflected light, the ilmenite shows a three-layer zonation (i.e., darker cores, lighter rims and more brighter middle zone) (Fig. 11c).

Phlogopite (trace – 9 vol.% for most samples and a high 22 vol.% for sample SC11 A1) forms part of the groundmass assemblage and occurs as fine-grained interlocking laths (0.06 to 0.29 mm) (e.g., Fig. 11d & e). The phlogopite is colourless and mostly pale green. The partial alteration where green colours are observed indicates the chloritization of phlogopite. Commonly, the laths contain inclusions of opaque spinel and dark-brown perovskite (Fig. 11e & f).

Spinel (0.02 – 0.1 mm) is the dominant fresh groundmass mineral (9 – 17 vol.% for most samples and a low 2 vol.% for sample SC11 A6) and is scattered throughout the rock samples. The grains are euhedral and mostly have a cubic shape. Spinel is closely associated with the less abundant perovskite (trace – 5 vol.% for most samples and two samples contain a high abundance of 7 vol.%, i.e., SC11 A1 and SC11 B1). Perovskite (0.06 to 0.08 mm; one sample, SC11 A6, contains coarser perovskite up to 0.15 mm) occurs as subrounded to cubic euhedral grains. The perovskite has a very dark brown colour and is near-opaque. This makes it difficult to distinguish perovskite from spinel (e.g., Fig. 11d). However, in reflected light, the difference is clearly observed. Spinel grains usually have little holes almost resembling a poikilitic texture, whereas perovskite is smooth and clear (Fig. 11e & g). The spinel also displays clear core-rim zonation observed in reflected light with darker cores and brighter rims (Fig. 11h) whereas no zonation is observed for perovskite in reflected light.

Apatite (0.1 mm) is rare (trace amounts) but present as lath shaped groundmass grains. The spaces between macrocrysts and groundmass is filled by the interstitial material (26 – 37 vol.% for most samples). Usually, the samples with high olivine abundance contain a low abundance of interstitial material, i.e., 16 vol.%; SC11 A4b, 21 vol.%; SC11 B5, 22 vol.%; SC11 B3b), which includes calcite (colourless material occupying spaces between phlogopite and opaques, Fig. 11d) and serpentine.

Table 2. Modal abundances of primary minerals and alteration material in dike and pipe samples.

No.	Sample	Mineral abundance (%)					
		olivine	ilmenite	phlogopite	spinel	perovskite	alteration
	Dike samples						
1	SC11 A1	27	2	22	13	7	30
2	SC11 A2	56	5	2	9	2	26
3	SC11 A4b	63	11	1	9	trace	16
4	SC11 A6	53	8	trace	2	trace	37
5	SC11 B1	40	2	9	15	7	27
6	SC11 B2	36	5	9	17	5	28
7	SC11 B3b	43	17	3	10	5	22
8	SC11 B4	35	3	8	14	4	36
9	SC11 B5	51	7	3	13	5	21
10	SC11 B6a	-	-	-	-	-	-
	Average	45	7	6	11	4	27
	Pipe samples						
11	SC80 2-1	73	10	2	1	2	12
12	SC80 3-2	62	4	trace	7	1	26
13	SC80 5-2	49	18	8	11	3	12
14	SC80 8-2	80	6	1	3	trace	10
15	SC80 14-1	51	14	5	5	2	22
	Average	63	10	3	5	2	16

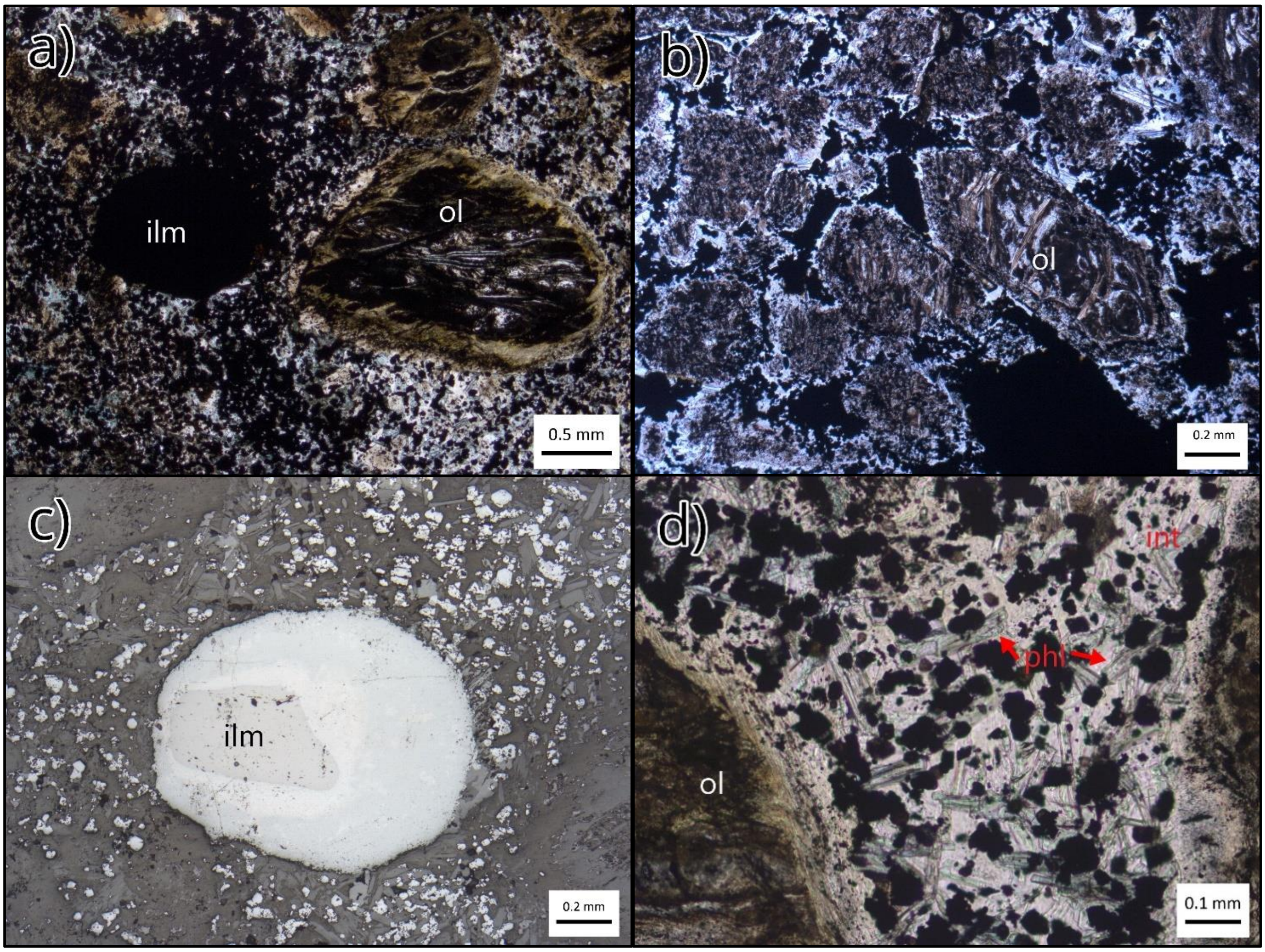

Fig. 11. Photomicrographs showing textural characteristics of the Camp Alpha dike samples in this study. (a) Olivine and ilmenite macrocrysts occurring in a spinel dominated groundmass. (b) Completely altered olivine macrocrysts occur as elongated and rounded grains. (c) Reflected light image of ilmenite macrocryst with a three-layer zonation (i.e., darker cores, lighter rims and more lighter middle layer). (d) A zoomed-in image of the groundmass phases; phlogopite, spinel, perovskite and alteration material. The perovskite has a very dark-brown colour and is near-opaque. This makes it difficult to distinguish perovskite from spinel. (e) Reflected light image showing the groundmass phases; phlogopite, spinel, perovskite. The spinel grains usually have little holes almost resembling a poikilitic texture, whereas perovskite is smooth and clear. (f) Reflected light image showing groundmass phlogopite with poikilitic texture. (g) Spinel and perovskite under reflected light. The groundmass is phlogopite-poor in this sample. (h) Reflected light image showing a core to rim zonation in spinel. The zonation is characterized by a darker core and a lighter rim. (**Note**: *phl = phlogopite, prv = perovskite, sp = spinel, ol = olivine, ilm = ilmenite, int = interstitial material*).

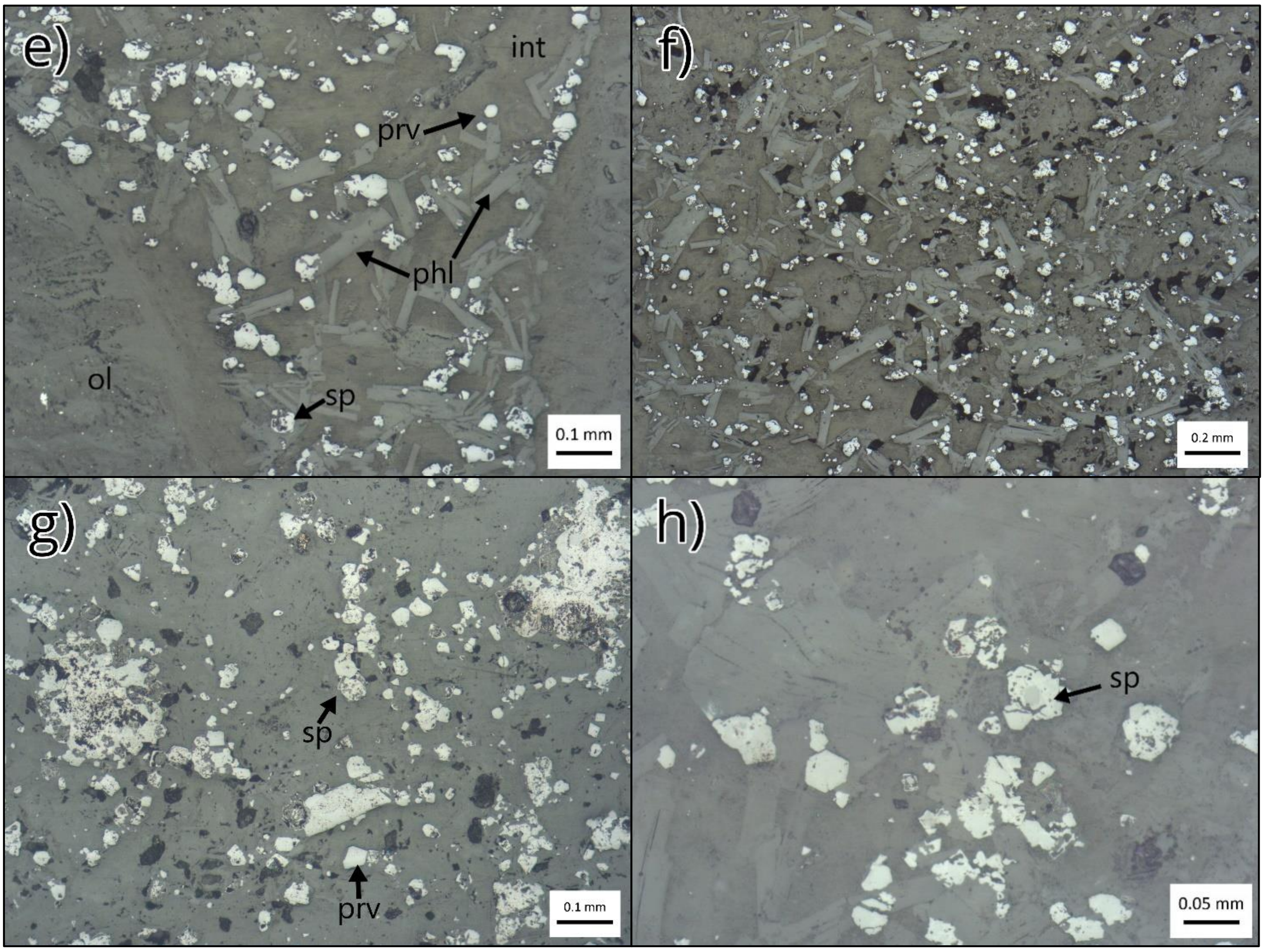

Fig. 11. *Continues*

<u>Pipe samples</u>

In comparison to dike samples, the pipe samples generally have greater abundances of ilmenite and olivine macrocrysts (Fig. 12a), and lower proportions of interstitial material (Table 2).

The original microcryst morphologies are still preserved (Fig. 12b), and the abundance of olivine macrocrysts and microcrysts is higher compared to the dike samples (49 to 62 vol.% for most samples and two samples contain unusually high olivine content of 73 and 80 vol.%, i.e., SC80 2-1 and SC80 8-2, respectively).

In contrast to the dike samples, the ilmenite does not show any zonation in reflected light microscopy (Fig. 12c). The size and abundance of ilmenite vary noticeably between dike and pipe samples. The ilmenite macrocrysts in pipe samples are larger and more abundant (i.e., up to 6 mm; 18 vol.%; sample SC80 5-2) in comparison to dike samples (i.e., <4 mm; 5 vol.%; sample SC11 B2).

The phlogopite abundance is lower than in dike samples.

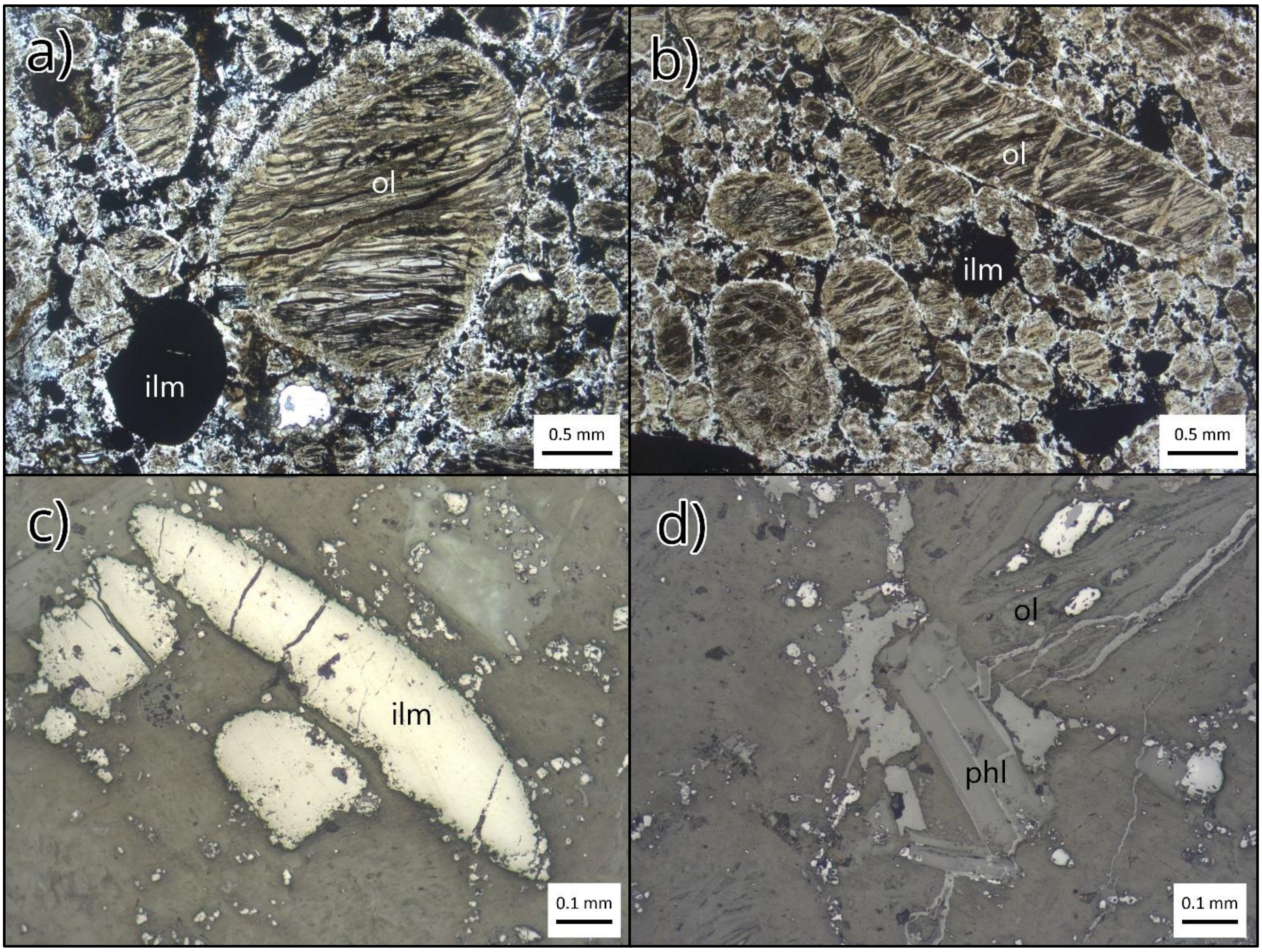

Fig. 12. Photomicrographs showing textural characteristics of the Camp Alpha pipe samples in this study. (a) Olivine and ilmenite macrocrysts occurring in a finer-grained matrix. (b) Rounded and elongated olivine macrocrysts that are completely altered. The microcrysts are still preserved. (c) Reflected light image of an elongated ilmenite. (d) Euhedral phlogopite microcryst under reflected light. (e) Groundmass phlogopite with spinel and perovskite inclusions. (f) Spinel and perovskite under reflected light. The groundmass is phlogopite-poor in this sample. (***Note***: *phl = phlogopite, prv = perovskite, sp = spinel, ol = olivine, ilm = ilmenite, int = interstitial material*).

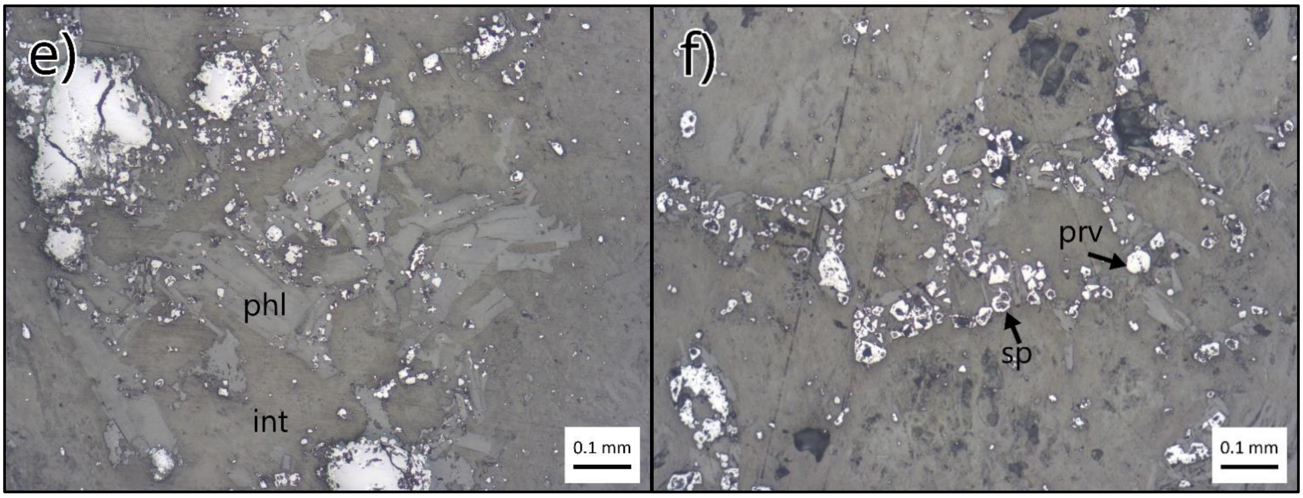

Fig. 12. *Continues*

4.1.2 Mineral chemistry

4.1.2.1 Phlogopite groundmass chemistry

The full dataset of phlogopite compositions is presented in Appendix 1A. The phlogopite analyses were performed on 4 representative dike samples (i.e., SC11 A1, SC11 B1, SC11 B2 and SC11 B3b) and at least 10 grains were analysed per sample. The phlogopite composition is similar in all samples and the grains are strongly zoned. Most of the phlogopites show compositional variations across the grains (many zones similar to what previously documented in other kimberlites, e.g., Giuliani et al., 2016), however, some grains show two zone, i.e., darker zone 1 and lighter zone 2. Occasionally, the grains have cores and rims that are characterised by darker zone 1 and lighter zone 2, respectively (Fig. 13a & c). Mostly, the zonation is random where zone 1 covers most of the grain and zone 2 occurs as patches (Fig. 13b & d). Zone 1 and zone 2 were analysed separately in some of the grains, however, zone 2 could not be analysed in most grains due to its thickness relative to the beam diameter. The width of the analysed phlogopites ranges from 20 to 30 µm and the diameter of the beam in the EPMA analysis was 2 µm. The thickness of zone 2 ranges from 1.5 to 10 µm (but mostly < 2 µm).

Zone 1 is characterised by an Al_2O_3 content that ranges from 2.84 to 17.5 wt.%, BaO (below detection limit – 3.17 wt.%) and TiO_2 (0.02 – 0.96 wt.%). In comparison to zone 1, the lighter zone 2 is characterised by a higher Al_2O_3 content that ranges from 13.7 to 19.4 wt.%, BaO (below detection limit – 8.51 wt.%), TiO_2 (0.06 – 1.47 wt.%) and lower CaO (0.01 – 0.27 wt.%). For both zones, the TiO_2 content shows no variation with varying Al_2O_3 (Fig. 14a). There is a slight negative correlation between Al_2O_3 and FeO, where FeO varies slightly with significantly varying Al_2O_3 (Fig. 14b).

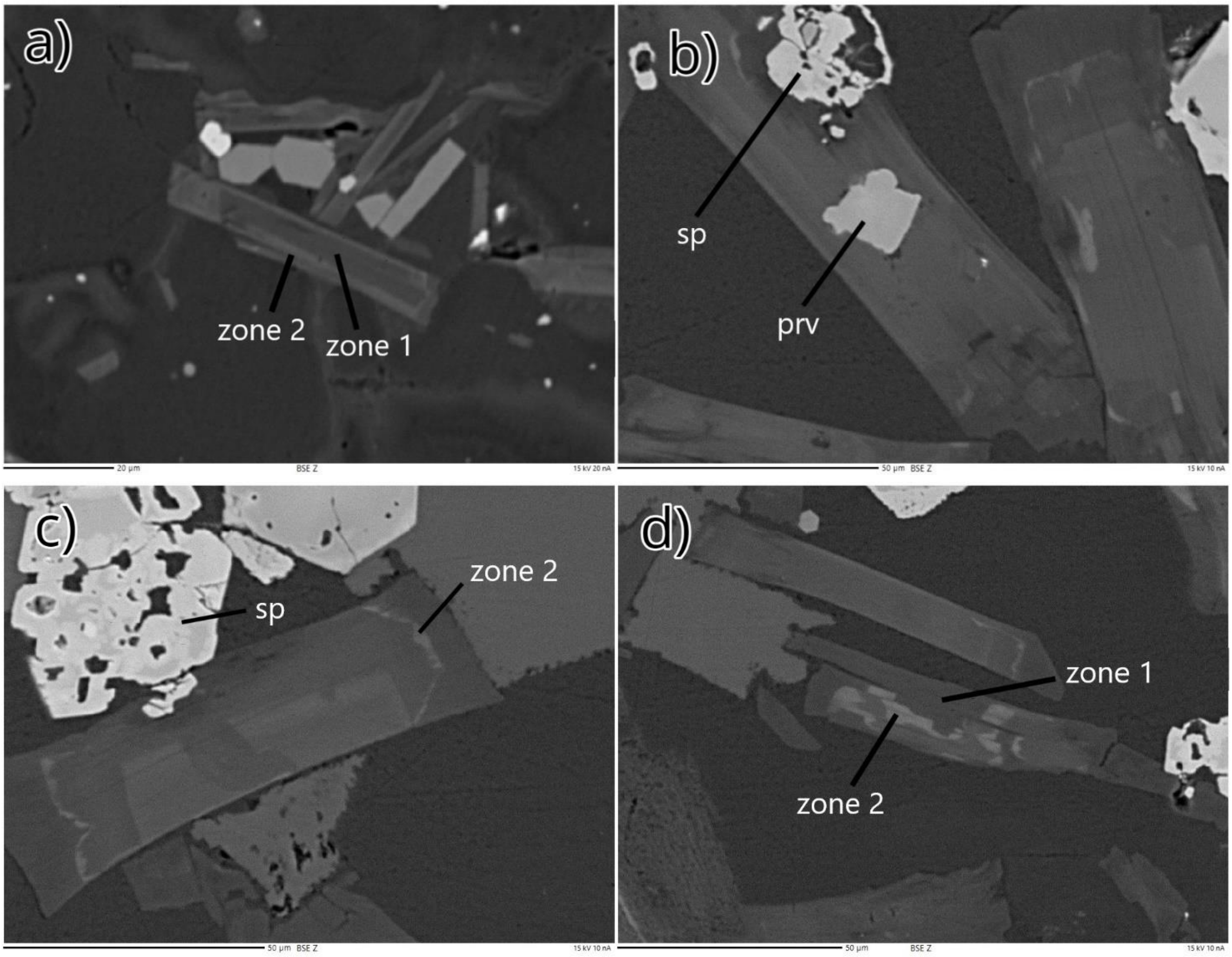

Fig. 13. Back-scattered electron (BSE) images of phlogopites from Camp Alpha dike. (a) Phlogopite with core and rim that are characterised by darker zone 1 and lighter zone 2, respectively. (b) Poikilitic phlogopite with spinel and perovskite as chadacrysts. The zoning is random and complicated in this grain. (c) Thin layer of zone 2 occurring towards the rims. (d) Random zonation where zone 1 covers most of the grain and zone 2 occurs as patches. *The small thin lines underneath each image represent the scales (20 µm for image (a) and 50 µm for the rest of the images).*

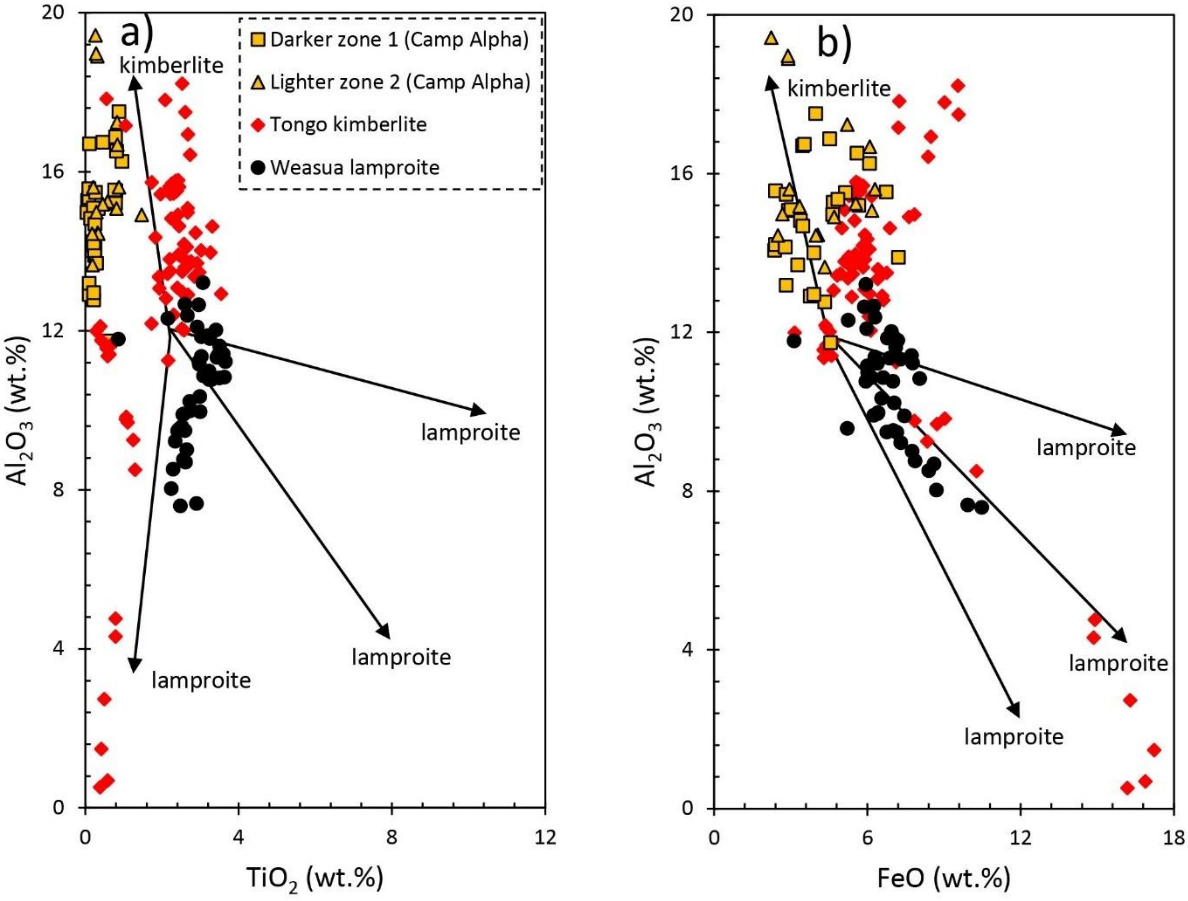

Fig. 14. Variation plots of phlogopite from Camp Alpha dike (this study), Tongo kimberlite and Weasua lamproite (Howarth and Giuliani, 2020). (a) Al_2O_3 vs TiO_2 (b) Al_2O_3 vs FeO. The arrows represent trends of phlogopites from literature data in **Fig. 4**.

4.1.2.2 Spinel groundmass chemistry

The full dataset of spinel compositions is presented in Appendix 1B. The spinel analyses were performed on 4 representative dike samples (i.e., SC11 A1, SC11 B1, SC11 B2 and SC11 B3b) and at least 10 grains were analysed per sample. The spinel composition is similar in all samples and the grains are strongly zoned. Two zones were identified in BSE images, i.e., a darker zone 1 and lighter zone 2, which were analysed separately. Zone 1 and zone 2 occur randomly as patches throughout the grains (Fig. 15).

The spinels contain Al_2O_3 that ranges from 0.03 to 13.9 wt.%, Cr_2O_3 (0.03 – 12 wt.%), MgO (0.03 – 19.7 wt.%), Fe_2O_3 (below detection – 71.7 wt.%) and FeO (2.29 – 20.0 wt.%). The darker zone 1 is enriched in Al_2O_3 (0.03 – 13.9 wt.%) and Cr_2O_3 (0.03 – 12.1 wt.%), in comparison to the lighter zone 2 (0.09 – 5.82 wt.%: Al_2O_3; 0.16 – 2.66 wt.%: Cr_2O_3). As a result of this Al_2O_3 and Cr_2O_3 enrichment, zone 1 generally has lower $Fe^{3+}/(Fe^{3+}+Al+Cr)$ and Cr/(Cr+Al) ratios, in comparison to zone 2.

For both zones, the spinel exhibits compositional zoning from chromite towards the MUM field (trend 1) but with slightly higher Fe^{3+}, as observed in Fig. 16. Most of the analyses lie on the MUM field because only a few Cr-rich spinel cores were found.

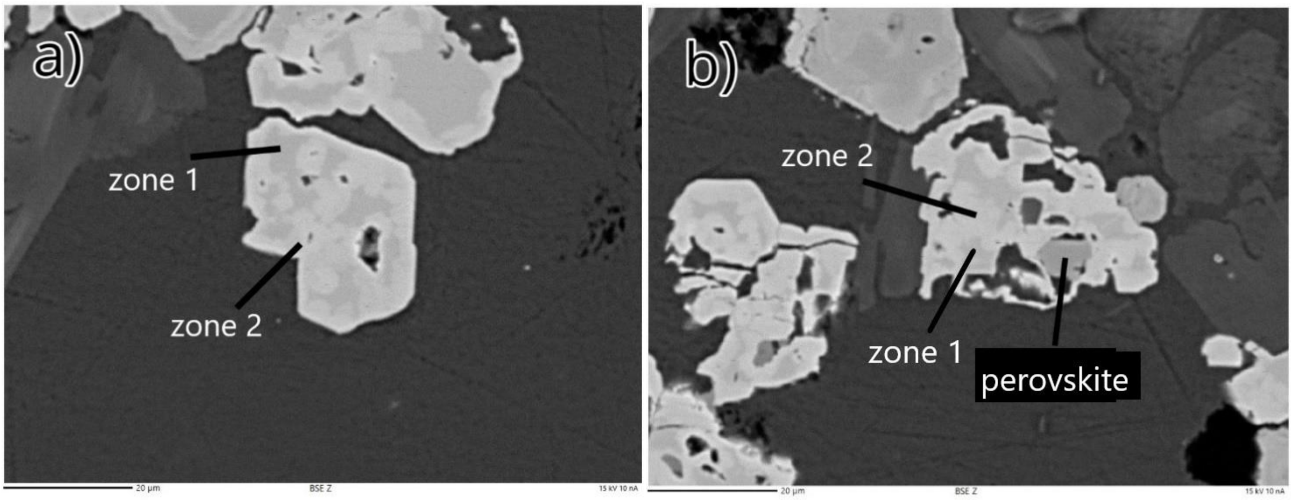

Fig. 15. Back-scattered electron (BSE) images of spinels from Camp Alpha dike. Zone 1 and zone 2 occur randomly as patches throughout the grains.

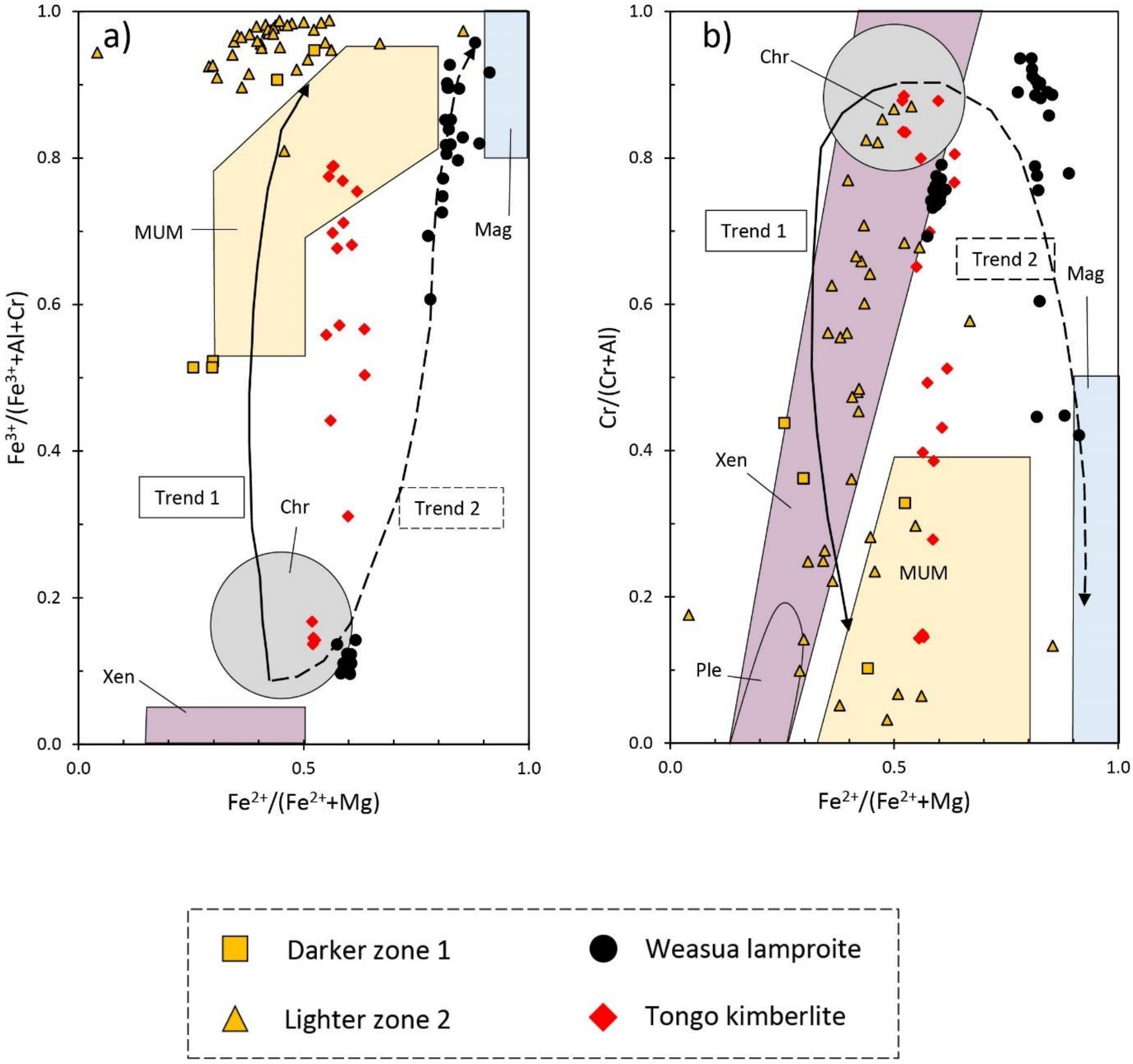

Fig. 16. Variation plots of spinel (darker zone 1 and lighter zone 2) from Camp Alpha dike (this study), Tongo kimberlite and Weasua lamproite (Howarth and Giuliani, 2020). (a) $Fe^{3+}/(Fe^{3+}+Al+Cr)$ ratio vs $Fe^{2+}/(Fe^{2+}+Mg)$ ratio. (b) $Cr/(Cr+Al)$ ratio vs $Fe^{2+}/(Fe^{2+}+Mg)$ ratio. The arrows represent compositional trends of spinels from literature data in **Fig. 5**.

4.1.3 Bulk rock geochemistry

A total of 10 representative samples (i.e., SC11 A1, SC11 A2, SC11 A4, SC11 A6, SC11 B1, SC11 B2, SC11 B3b, SC11 B4, SC11 B5 and SC11 B6) of the dikes from the Camp Alpha region were selected for trace element geochemical analysis. The selected samples were also analysed for Sr-Nd isotope geochemistry, apart from samples SC11 A6 and SC11 B6. The trace element and Sr-Nd isotope compositions are reported in Tables 3 & 4, respectively. The major element compositions of the selected samples are reported by Haggerty (2017) and briefly discussed in section 2.3.3.

4.1.3.1 Trace elements composition

The Camp Alpha dike samples are enriched in LREE (Ce > La ≥ Nd > Pr), Nb, Sr and Th, relative to HREE. The concentrations of Ce ranges from 28.1 to 543 ppm, La (13.2 – 277 ppm), Nd (9.89 – 205 ppm), Pr (3.20 – 64.5), Nb (99.5 – 470 ppm), Sr (85.4 – 789 ppm) and Th (5.40 – 29.3 ppm). The trace element ratios La/Yb, Gd/Yb and La/Sm of the Camp Alpha dike samples have ranges of 43.1 – 254, 2.81 – 16.8 and 8.96 – 13.7, respectively (Fig. 18a & b). These rocks are characterised by Ba/Nb ratios that range from 0.91 to 9.55 (<11.5), La/Nb (0.12 – 1.22; mostly <1.10) and Ce/Pb (6.77 – 99.2; mostly >22) (Fig. 18c & d).

To plot the distribution patterns shown in Fig. 17, the Camp Alpha REE data were normalised using chondrite values reported by Sun and McDonough (1989), i.e., equation (1).

$$\text{Normalised value} = \frac{\text{rare earth element concentration in rock}}{\text{chondrite value}} \tag{1}$$

The rest of the trace element data were normalised using primitive mantle values also reported by Sun and McDonough (1989), i.e., equation (2).

$$\text{Normalised value} = \frac{\text{trace element concentration in rock}}{\text{primitive mantle value}} \tag{2}$$

The Camp Alpha samples show smooth sub-parallel chondrite normalised REE patterns and enrichment in light REE relative to heavy REE (e.g., LREE; La ~ 200 – 1200 × chondrite, HREE; Lu ~ 3 – 6 × chondrite. La/Yb_N ~ 31 – 182). The chondrite normalised REE profiles are similar to those of kimberlites (Fig. 17a). The Camp Alpha samples show smooth sub-parallel primitive mantle normalised trace element patterns and strong enrichment in highly incompatible elements (e.g., ~ 150 – 600 × primitive mantle) with the HREE showing least enrichment (e.g., Er to Lu; ~ 1 – 2 × primitive mantle). The Camp Alpha rocks are characterised by negative anomalies in Rb, K, Sr, and P (Fig. 17b).

4.1.3.2 Radiogenic Sr and Nd isotope composition

The average measured $^{87}Sr/^{86}Sr$ and $^{143}Nd/^{144}Nd$ ratios of the Camp Alpha samples are 0.706683 ± 0.000013 and 0.512073 ± 0.000012, respectively.

Rb, Sr, Sm and Nd naturally occur in different stable isotopic forms (i.e., ^{85}Rb, ^{87}Rb; ^{84}Sr, ^{86}Sr, ^{87}Sr, ^{88}Sr; ^{144}Sm, ^{147}Sm, ^{148}Sm, ^{149}Sm, ^{150}Sm, ^{152}Sm, ^{154}Sm; ^{142}Nd, ^{143}Nd, ^{144}Nd, ^{145}Nd, ^{146}Nd, ^{148}Nd, ^{150}Nd). The ICP-MS analysis produced total concentrations of Rb, Sr, Sm and Nd, thus, the proportions of the isotopes ^{87}Rb, ^{86}Sr, ^{147}Sm and ^{144}Nd were calculated from the total concentrations. To calculate the concentrations of the previously mentioned isotopes, equation (3) was used.

$$\text{Concentration}_{\text{x}} = \text{Total concentration}_{\text{E}} \times \text{Natural occurrence}_{\text{x}} \tag{3}$$

Where:

- x = isotope of interest (e.g., ^{87}Rb; ^{86}Sr; ^{147}Sm; ^{144}Nd)
- E = element of interest (e.g., Rb, Sr, Sm, Nd)
- Natural occurrences: ^{87}Rb = 27.8%, ^{86}Sr = 9.86%, ^{147}Sm = 15% and ^{144}Nd = 23.8%

The epsilon neodymium (εNd_i) values (i.e., equation 6) and the initial $^{87}Sr/^{86}Sr$ (i.e., equation 4) and $^{143}Nd/^{144}Nd$ (i.e., equation 5) ratios were calculated using the following equations:

$$\left(\frac{^{87}\text{Sr}}{^{86}\text{Sr}}\right)_m = \left(\frac{^{87}\text{Sr}}{^{86}\text{Sr}}\right)_i + \left(\frac{^{87}\text{Rb}}{^{86}\text{Sr}}\right)\left(\text{e}^{\lambda \text{t}} - 1\right) \tag{4}$$

$$\left(\frac{^{143}\text{Nd}}{^{144}\text{Nd}}\right)_m = \left(\frac{^{143}\text{Nd}}{^{144}\text{Nd}}\right)_i + \left(\frac{^{147}\text{Sm}}{^{144}\text{Nd}}\right)\left(\text{e}^{\lambda \text{t}} - 1\right) \tag{5}$$

$$\varepsilon\mathrm{Nd_i} = \left[\frac{\left(\frac{^{143}\mathrm{Nd}}{^{144}\mathrm{Nd}}\right)_i}{I^{\mathrm{t}}{}_{\mathrm{CHUR}}} - 1\right] \times 10\ 00 \qquad (6)$$

$$\left(\frac{^{143}\mathrm{Nd}}{^{144}\mathrm{Nd}}\right)_{\mathrm{CHUR,t}} = \left(\frac{^{143}\mathrm{Nd}}{^{144}\mathrm{Nd}}\right)_{\mathrm{CHUR,today}} + \left(\frac{^{147}\mathrm{Sm}}{^{144}\mathrm{Nd}}\right)_{\mathrm{CHUR,today}} \left(\mathrm{e}^{\lambda\mathrm{t}} - 1\right) \qquad (7)$$

Where:

- m is the measured ratio at the present time
- i is the initial ratio at the time of crystallization (at t)
- t is the age of the Camp Alpha dike
- λ is the decay constant from parent to daughter
- $\lambda = 1.42 \times 10^{-11}\ a^{-1}$ for the breakdown of ^{87}Rb to ^{87}Sr
- $\lambda = 6.54 \times 10^{-12}\ a^{-1}$ for the breakdown of ^{147}Sm to ^{143}Nd
- $\varepsilon\mathrm{Nd_i}$ is the epsilon value of Nd (to express the degree of Nd enrichment)
- $\mathrm{I^t}_{\mathrm{CHUR}}$ is the ratio of (^{143}Nd/^{144}Nd) for the chondrite uniform reservoir (CHUR) at the time of rock formation (t). This is calculated using equation 7.

The Camp Alpha dike occurs in close proximity to both the Jurassic aged Kumgbo and Mano Godua clusters and the Neoproterozoic Weasua cluster. The Kumgbo and Mano Godua clusters are suggested to be approximately 135 Ma, and the Weasua cluster ~ 800 Ma (e.g., Skinner *et al.*, 2004). The exact age of the Camp Alpha rocks is unknown. According to Haggerty (2017), the Camp Alpha dikes lie along fracture structures that were reactivated during Precambrian events and suggested that the Liberian trend dikes are of Precambrian age. Because of the close occurrence to Kumgbo, Mano Godua and Weasua clusters, both 135 Ma and 800 Ma were used to calculate the initial Sr and Nd ratios of the Camp Alpha dike and illustrated in Fig. 19. At 135 Ma, the initial ^{87}Sr/^{86}Sr ratio ranges from 0.70353 – 0.70998. The initial ^{143}Nd/^{144}Nd ratio and εNd value have a range of 0.51163 – 0.51208 and -16.3 to -7.44, respectively. At 800 Ma, the initial ^{87}Sr/^{86}Sr ratio ranges from 0.70265 – 0.70436. The initial ^{143}Nd/^{144}Nd ratio and εNd value have a range of 0.51118 – 0.51169 and 0.17 to 1.65 (two outliers -2.33 and -8.41), respectively (Fig. 19). The two ages, 135 and 800 Ma, produce very different initial ratios and trends. The most likely age of the Camp Alpha dike will be discussed in section 5.2.

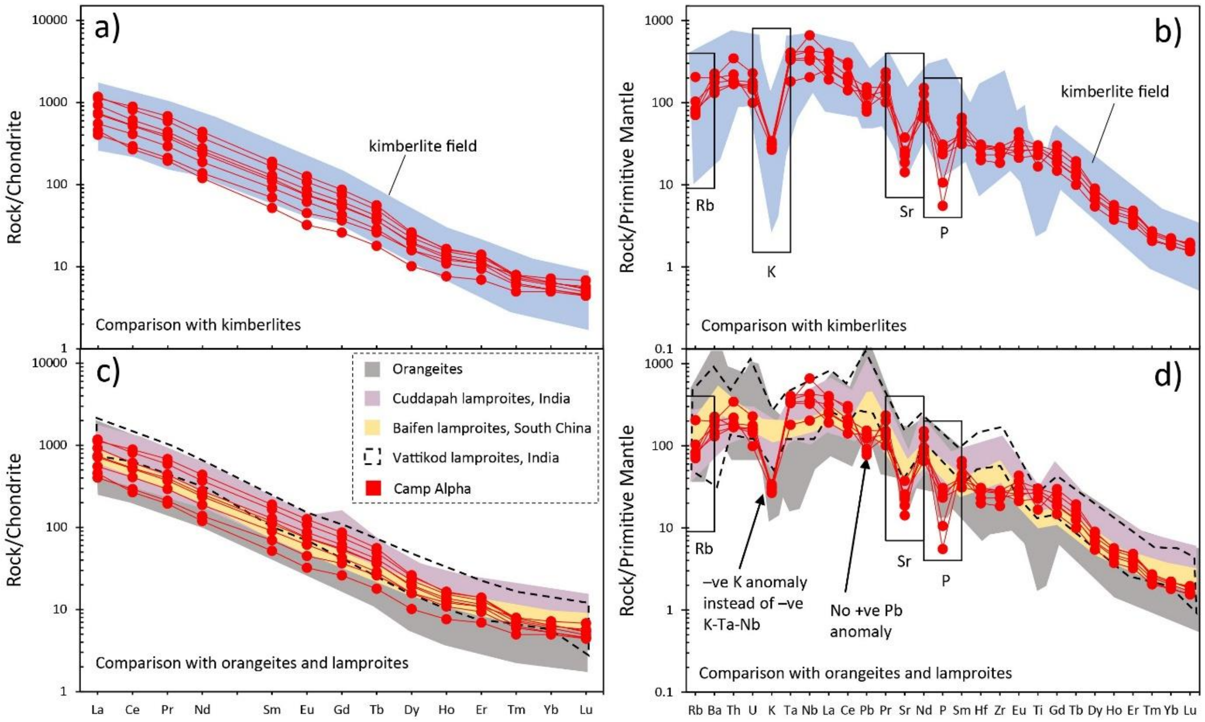

Fig. 17. Chondrite-normalised REE (in comparison with kimberlites; plot a; in comparison with orangeites and lamproites; plot c) and primitive mantle-normalised trace element (in comparison with kimberlites; plot b; in comparison with orangeites and lamproites; plot d) patterns for the Camp Alpha dike, normalised to the values of Sun and McDonough (1989). The bulk-rock literature data used to construct the kimberlite, orangeite and lamproite fields are the same as in **Fig. 7**.

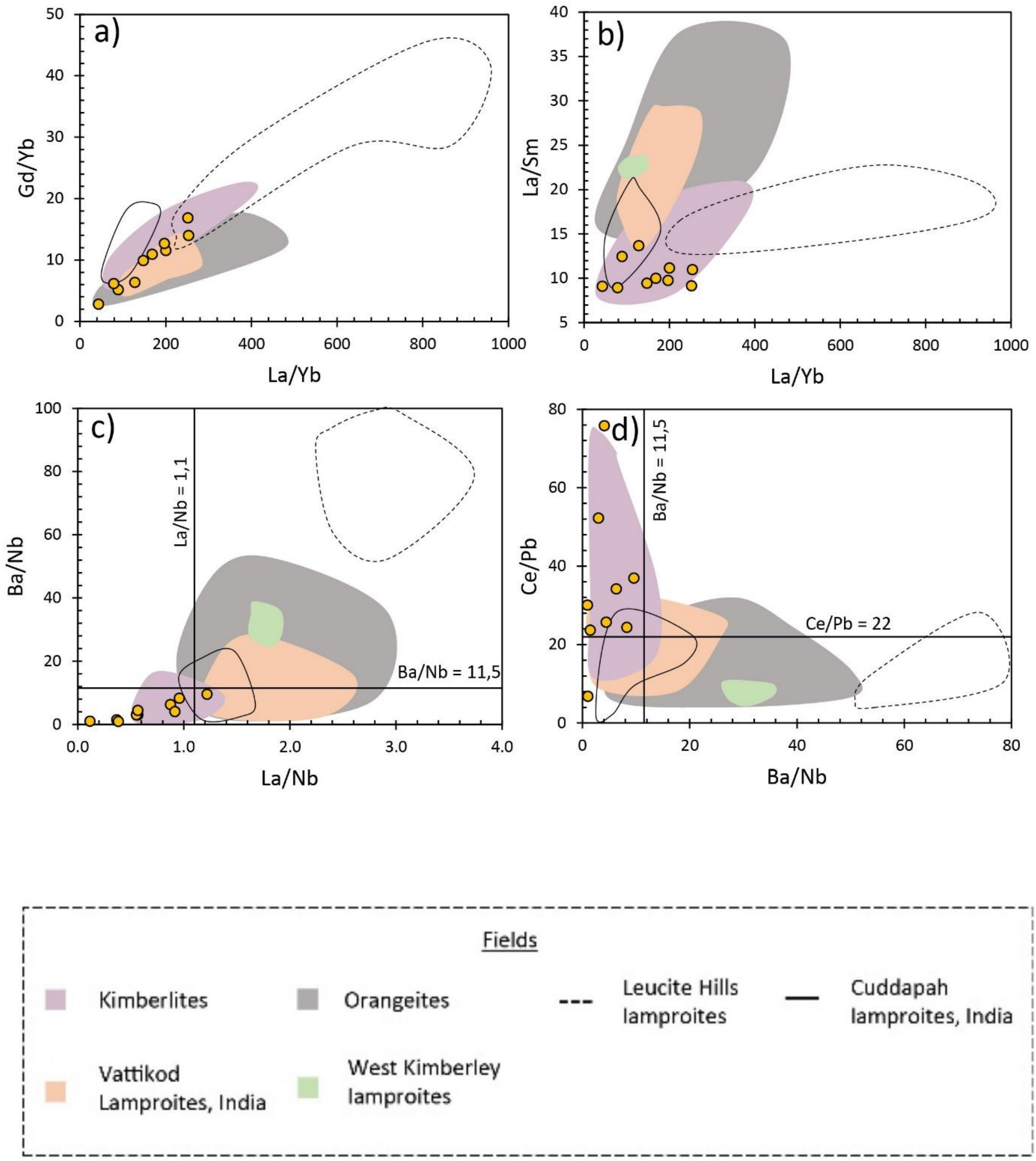

Fig. 18. Compositional variation of (a) Gd/Yb vs La/Yb (b) La/Sm vs La/Yb (c) Ba/Nb vs La/Nb and (d) Ce/Pb vs Ba/Nb for the Camp Alpha dike. The bulk-rock data used to construct the fields were taken from the same literature as in **Fig. 6**.

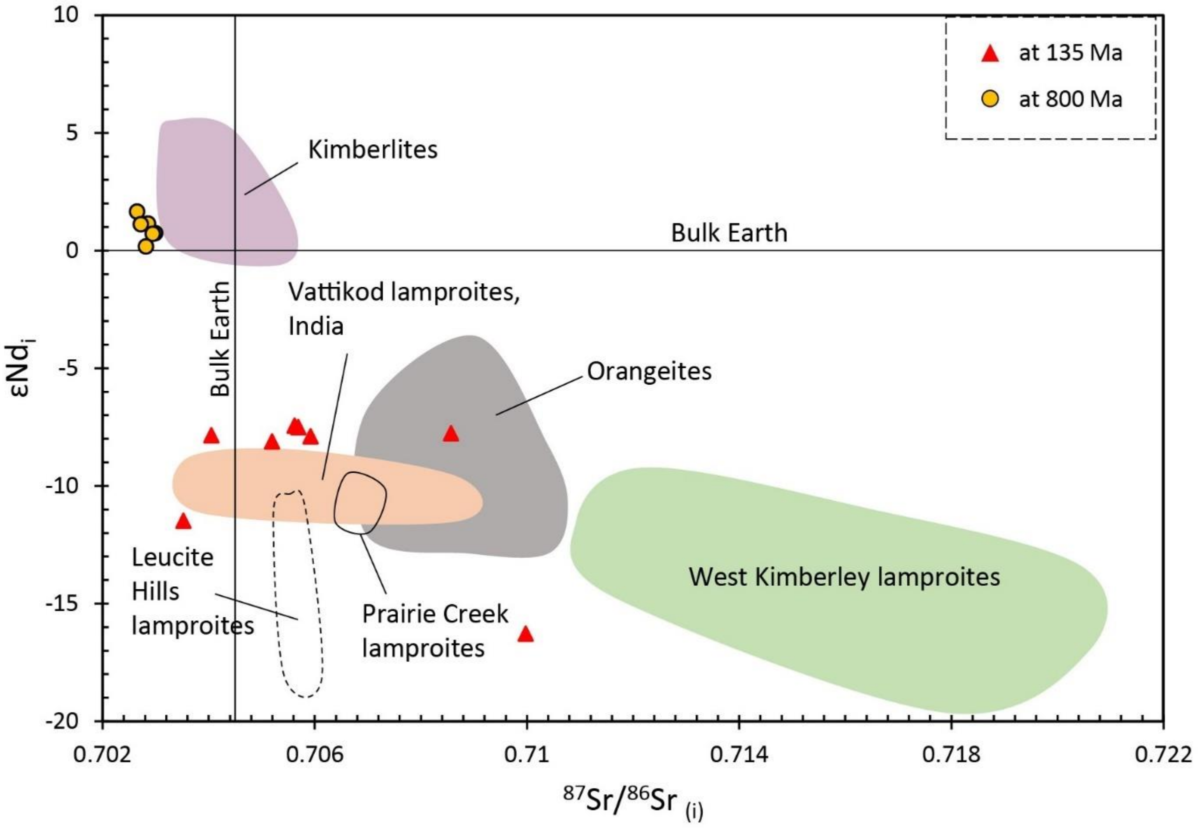

Fig. 19. Variation of Sr-Nd isotopic composition in Camp Alpha dike samples. The εNd$_i$, at 135 Ma and 800 Ma, is plotted against the initial $^{87}Sr/^{86}Sr$ ratio. The Sr-Nd isotopic composition literature data used to construct the fields are the same as in **Fig. 9.**

Table 3. Bulk-rock trace element composition for the Camp Alpha dike.

Trace element	SC11-A1	SC11-A2	SC11-A4b	SC11-A6	SC11-B1	SC11-B2	SC11-B3b	SC11-B4	SC11-B5	SC11-B6a
ppm										
Li	1.09	1.07	1.31	1.38	10.4	1.46	1.97	2.94	2.07	8.39
Sc	21.3	21.9	30.8	15.4	19.5	17.4	17.7	16.3	17.7	13.1
V	95.6	160	233	108	189	169	194	194	166	224
Cr	1392	1878	2445	1128	662	1269	1105	1079	1247	660
Co	80.2	114	124	98.2	50.9	98.6	97.8	91.6	94	56.2
Ni	962	1429	1445	1601	496	1059	1096	1033	1043	514
Cu	32.1	48.7	87.6	13.7	54.5	124	125	98.9	123	92
Zn	55.7	53.7	100	43.2	50.6	54.4	69.7	52.5	64.7	58.1
Rb	44.6	3.39	2.08	3.47	88.4	52.7	52.9	48.3	65.3	130
Sr	392	85.4	105	116	421	510	475	543	299	789
Y	17.3	7.95	12.5	2.17	17.2	19	21.6	15.4	21.4	16.3
Zr	206	403	583	166	178	313	301	293	319	259
Nb	470	154	281	114	99.5	305	251	231	303	145
Ba	1408	218	255	114	822	910	1575	1024	1223	1382

Table 3. *Continues*

Trace element	SC11-A1	SC11- A2	SC11-A4b	SC11-A6	SC11-B1	SC11-B2	SC11-B3b	SC11-B4	SC11-B5	SC11-B6a
ppm										
La	266	56.5	108	13.2	95.4	169	219	131	277	176
Ce	543	93.9	164	28.1	179	317	372	250	496	322
Pr	64.5	9.75	18.4	3.21	20.1	35.4	41.9	27.7	56	37.8
Nd	205	29.7	55.8	9.89	64.2	111	129	87.6	172	119
Sm	29	4.53	7.89	1.45	10.6	16.9	19.7	13.8	25.2	18
Eu	7.29	1.18	1.86	0.43	2.65	4.27	5.05	3.56	6.20	4.36
Tb	2.08	0.43	0.67	0.11	0.97	1.36	1.55	1.07	1.85	1.37
Gd	17.8	3.28	5.34	0.86	7.49	11	12.6	8.78	15.3	11.4
Dy	6.62	1.82	2.57	0.46	4.04	5.01	5.71	3.99	6.39	4.86
Ho	0.91	0.31	0.43	0.08	0.68	0.77	0.86	0.61	0.93	0.72
Er	2.3	0.82	1.14	0.26	1.79	1.91	2.13	1.55	2.31	1.79
Tm	0.19	0.10	0.13	0.04	0.20	0.18	0.20	0.15	0.20	0.16
Yb	1.06	0.63	0.84	0.31	1.21	1.01	1.10	0.89	1.09	0.90
Lu	0.15	0.08	0.11	0.05	0.17	0.12	0.14	0.11	0.14	0.12

Table 3. *Continues*

Trace element	SC11-A1	SC11-A2	SC11-A4b	SC11-A6	SC11-B1	SC11-B2	SC11-B3b	SC11-B4	SC11-B5	SC11-B6a
ppm										
Hf	6.14	11.7	17.2	4.75	5.13	9.30	8.94	8.63	9.49	7.13
Ta	14.2	17.4	24.4	7.71	5.36	16.7	13.9	13.5	15.1	7.40
Pb	5.48	3.97	5.45	4.15	7.36	6.07	10.9	9.72	6.54	8.73
Th	29.3	5.40	24.6	9.08	8.74	14.3	14.4	14.2	15.8	18.7
U	4.79	2.26	6.72	1.02	1.45	3.26	3.43	3.02	3.72	2.08

Table 4. Measured (m) and calculated initial (i) Sr-Nd isotope ratios for the Camp Alpha dike.

	SC11 A1	SC11 A2	SC11 A4b	SC11 B1	SC11 B2	SC11 B3b	SC11 B4	SC11 B5
Rb (ppm)	44.6	3.39	2.08	88.4	52.7	52.9	48.3	65.3
Sr (ppm)	393	85.4	105	421	510	475	543	299
$^{87}Rb/^{86}Sr$	0.3202	0.1119	0.0562	0.5915	0.2913	0.3139	0.2507	0.6159
$(^{87}Sr/^{86}Sr)_m$	0.706304	0.704268	0.703633	0.711117	0.706182	0.706528	0.705678	0.709753
SD	0.000012	0.000017	0.000014	0.000015	0.000011	0.000015	0.000012	0.000011

Table 4. *Continues*

	SC11 A1	SC11 A2	SC11 A4b	SC11 B1	SC11 B2	SC11 B3b	SC11 B4	SC11 B5
Sm (ppm)	29.01	4.53	7.89	10.6	16.9	19.7	13.8	25.2
Nd (ppm)	205	29.7	55.8	64.2	111	129	87.6	171.6
^{147}Sm/^{144}Nd	0.0894	0.096	0.0891	0.1043	0.096	0.0958	0.0996	0.0926
(^{143}Nd/^{144}Nd)$_m$	0.512159	0.512147	0.511955	0.511723	0.512168	0.512144	0.512137	0.512149
SD	0.000011	0.000012	0.000011	0.000014	0.000012	0.000012	0.000012	0.000012
				at 135 Ma				
(^{87}Sr/^{86}Sr)$_i$	0.70569	0.70405	0.70353	0.70998	0.70562	0.70593	0.7052	0.70857
(^{143}Nd/^{144}Nd)$_i$	0.51208	0.51206	0.51188	0.51163	0.51208	0.51206	0.51205	0.51207
εNd$_i$	-7.49	-7.84	-11.48	-16.26	-7.44	-7.89	-8.1	-7.75
				at 800 Ma				
(^{87}Sr/^{86}Sr)$_i$	0.70265	0.70299	0.70299	0.70436	0.70285	0.70294	0.70281	0.70272
(^{143}Nd/^{144}Nd)$_i$	0.51169	0.51164	0.51149	0.51118	0.51166	0.51164	0.51162	0.51166
εNd$_i$	1.65	0.74	-2.33	-8.41	1.14	0.7	0.17	1.11

4.2 Rocks from Weasua

Eight samples from this location are described in this study (i.e., Y5747, Y5752, Y5755, Y5759, Y5767, 2-10-3, 2-12-2 and 2-12-3) and were all sampled from a coherent textured rock body. The samples are all relatively similar in mineralogy and are described together in this study. Weasua is located in Liberia, West Africa, however, the exact rock body from within the cluster from where the representative samples were taken is unknown.

Only polished sections were available for these Weasua rocks, and no bulk samples were left. As a result, the perovskite trace elements were analysed as a proxy for bulk rock trace element geochemistry and will be compared with the Camp Alpha samples. The phlogopite and spinel chemistry for these samples will be incorporated from Howarth and Giuliani (2020) to compare with the Camp Alpha samples.

4.2.1 Petrography

The Weasua samples contain abundant subhedral olivine macrocrysts (up to 13 mm) and subhedral to anhedral microcrysts (0.32 to 0.40 mm), set in a fine-grained groundmass.

The olivine grains are serpentinized, but the degree varies even within the same sample. Mostly, the macrocrysts are partially altered on the margins only with fresh cores (Fig. 20a), but occasionally, the olivine macrocrysts are completely altered (i.e., samples Y5747, 2-10-3) (Fig. 20b). Occasionally, the microcrysts are partially altered on the margins with fresh cores (i.e., samples Y5759, 2-12-3, 2-12-2) but mostly, the microcrysts are completely serpentinized. The macrocrysts are generally elongated whereas the microcrysts are generally rounded. Spinel can be observed as chadacrysts within the margins of the olivine grains but never in the core.

Phlogopite dominates (0.16 – 0.48 mm) the groundmass and occurs as patches, and sometimes observed as interlocking laths (Fig. 20c & d) (i.e., samples Y5752 and Y5767), that are pleochroic dark brown to light brown (i.e., samples Y5747 and 2-12-2). Poikilitic phlogopite is observed in some samples (i.e., Y5747, Y5759 and 2-12-3) (Fig. 20e) where the chadacrysts are diopside, spinel and perovskite. The poikilitic phlogopite appears light orange in colour and is pleochroic (light orange to light brown). Diopside is present in Weasua samples and occurs as euhedral blocky crystals (Fig. 20f). Mostly, the diopside appears colourless to pale green (0.25 – 0.54 mm in size) but occasionally light yellow in sample Y5759 (up to 0.80 mm in size) (Fig. 20g). The light yellow diopside contains inclusions of olivine, spinel and perovskite. Colourless apatite (up to 0.11 mm elongated prismatic crystals) is rare and occurs in the groundmass as an interstitial phase, identified by its low birefringence (1st order grey) and straight extinction.

Spinel and perovskite are present in the groundmass as fine grains and are evenly distributed throughout the samples. Spinel (ranging from 0.10 to 0.25 mm) is opaque and occurs as euhedral grains. Perovskite (ranging from 0.025 to 0.20 mm) is near opaque, dark brown in colour and occurs as euhedral grains. The perovskite occasionally encloses the spinel (Fig. 20h), indicating later crystallisation relative to the spinel. In reflected light, both perovskite and spinel have zonation with darker cores and brighter rims.

The interstitial spaces between macrocrysts and the groundmass grains are occupied by late-stage calcite, serpentine and green chlorite.

4.2.2 Perovskite chemistry

Two representative samples, Y5747 and Y5759, were selected for the analysis of perovskite chemistry (the full set of perovskite chemistry is presented in the Appendices chapter, i.e., major elements in Appendix 2A and trace elements in Appendix 2B). These samples are less altered and have greater perovskite abundance, relative to the rest of the Weasua collection of this study. The two samples, Y5747 and Y5759, were also analysed by Howarth and Giuliani (2020) for their olivine, phlogopite and spinel mineral chemistry. The phlogopite and spinel chemistry is illustrated in Fig. 14 & 16, respectively, relative to the Camp Alpha samples.

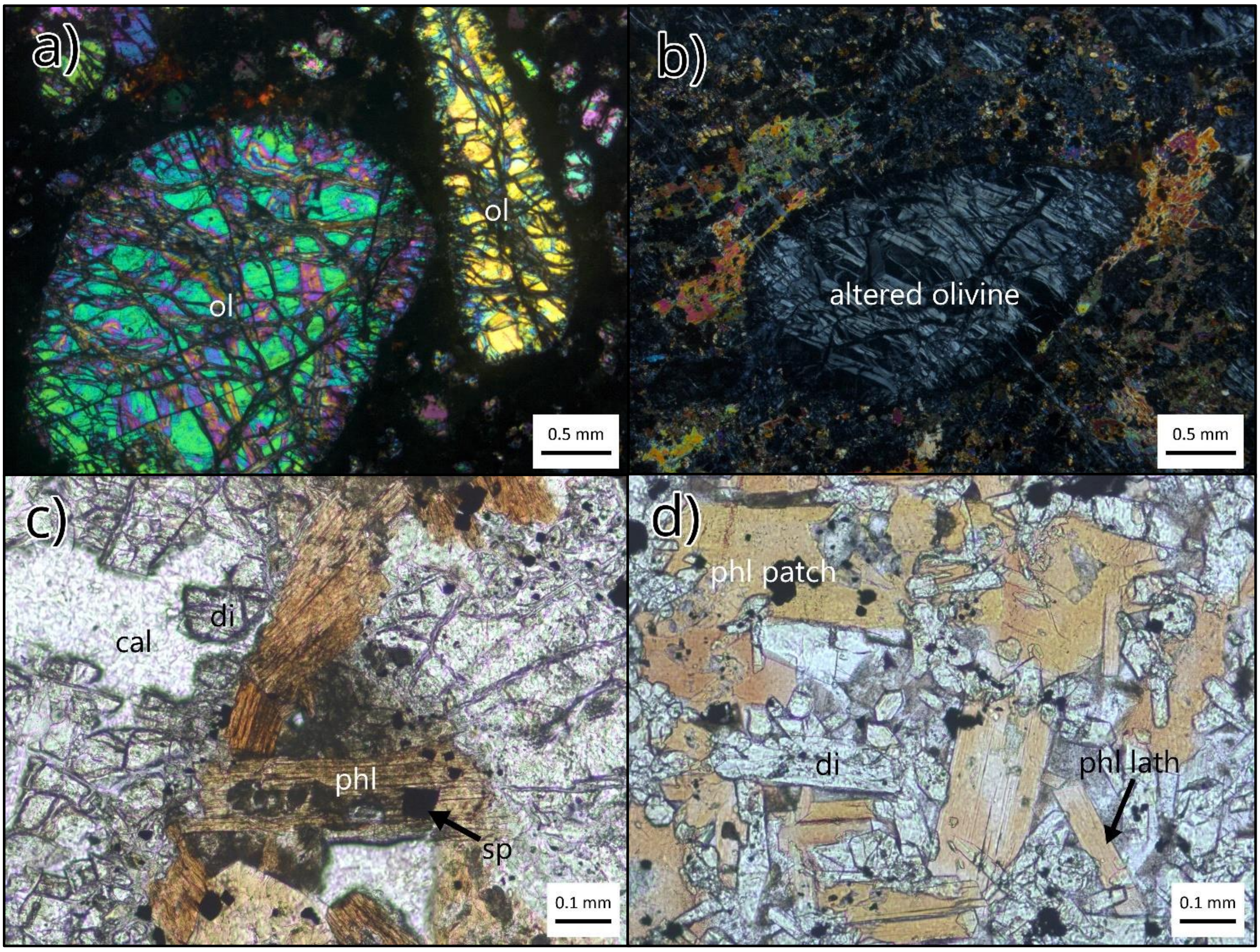

Fig. 20. Photomicrographs showing textural characteristics of the Weasua rocks studied in this project. (a) Rounded and elongated olivine macrocrysts. The olivine in this sample is relatively fresh. (b) Completely serpentinized olivine macrocryst. (c) Subhedral phlogopite microcryst with spinel inclusions. (d) Groundmass phlogopite which occurs as patches and euhedral laths. (e) Poikilitic groundmass phlogopite (orange-brown colour) containing inclusions of spinel and perovskite. (f) Groundmass phlogopite, diopside, and late-stage chlorite and calcite. (g) Light yellow diopside in sample Y5759 containing inclusions of spinel and perovskite. (h) Euhedral perovskite enclosing spinel. (**Note**: phl = phlogopite, di = diopside, chl = chlorite, cal = calcite, prv = perovskite, sp = spinel, ol = olivine, serp = serpentine).

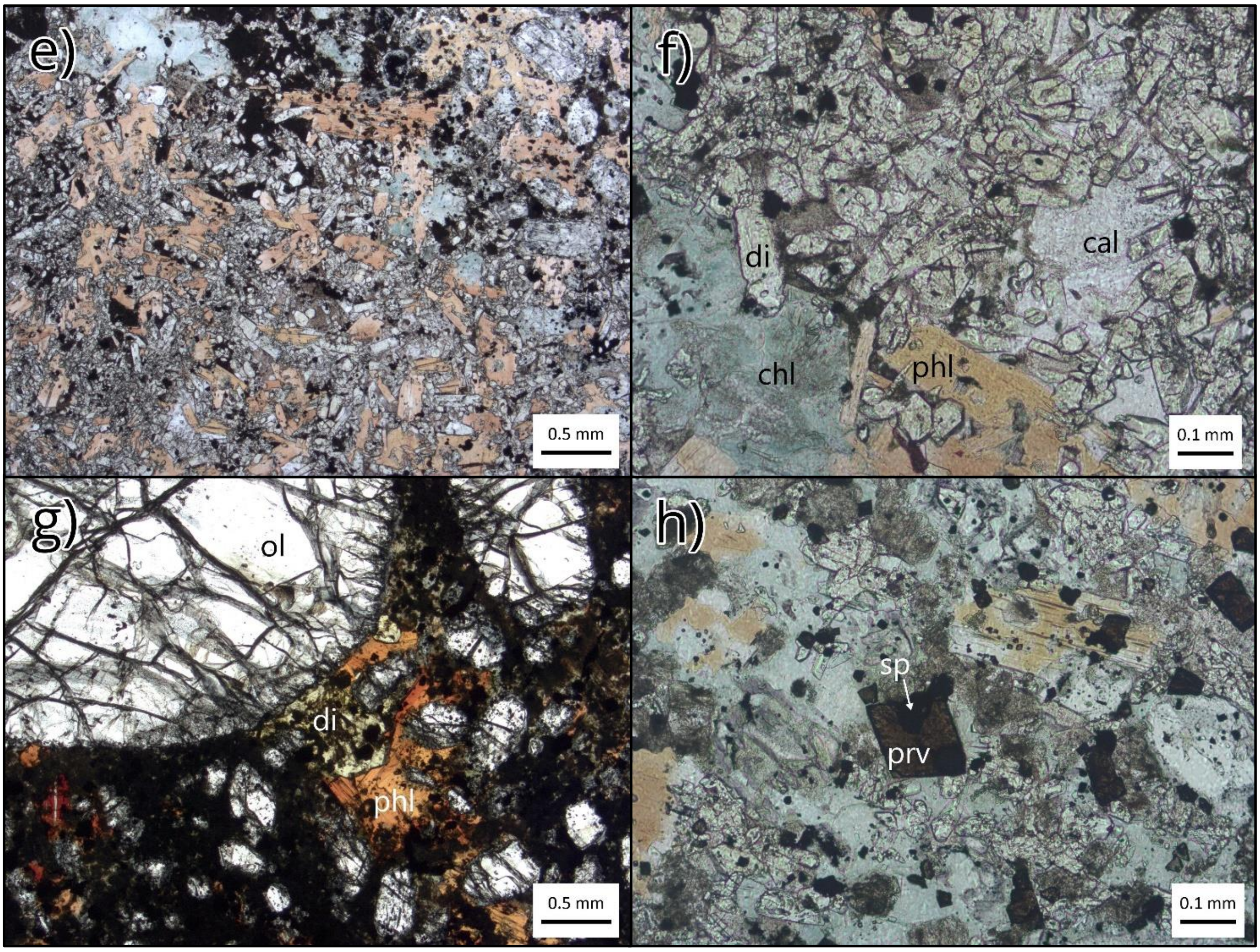

Fig. 20. *Continues*

4.2.2.1 Major-element composition

Perovskite crystals in both samples that were analysed, display zoning as a result of variations in major element composition. In both samples, Y5747 and Y5759, the perovskite grains exhibit complex oscillatory zoning patterns where the darker and brighter zones are alternating from the core to rims, with individual zones ranging from 0.4 – 10 µm in thickness. The number of zones observed ranges from 4 – 10 per grain. This oscillatory zoning typically has rounded concentric patterns with no sharp edges (e.g., Fig. 21a, b, c & e).

The zoning in perovskites is defined by variations in the rare earth elements (REE) and FeO contents. The concentrations of REE (La_2O_3 and Ce_2O_3) vary between light and dark regions. The lighter regions are characterised by higher REE contents, whereas the darker regions contain lower REE concentrations. The variation in Ce_2O_3 content occurs from core to rim, whereas the La_2O_3 content only shows variation within the rim (e.g., Fig. 21d & f). The concentrations of the elements, Al_2O_3 and Na_2O, show slight variation from core to the rim but never between the light and dark regions.

The perovskites from both samples consist mainly of TiO_2 (~ 54 wt%) and CaO (~ 36 wt%), which is close to the ideal composition ($CaTiO_3$). The concentration of TiO_2 ranges from 54.6 to 56.7 wt% and CaO ranges from 36.9 to 39.8 wt%. The grains contain minor concentrations of FeO (0.78 – 1.76 wt%), Ce_2O_3 (below EPMA detection and up to 0.84 wt%), La_2O_3 (0.16 – 0.77 wt%; $Ce_2O_3+La_2O_3 < 2$ wt%), Na_2O (0.19 – 1.05 wt%), and Al_2O_3 (0.01 – 0.44 wt%). There are positive correlations of FeO and TiO_2 against CaO, as shown in Fig. 22a & b. Na_2O and LREE correlate negatively against CaO (Fig. 22c & d). The cores are slightly enriched in $(LREE)_2O_3$ (Fig. 22d) but depleted in FeO (Fig. 22a) compared to the rims.

4.2.2.2 Trace element composition

As mentioned in section 4.2.2.1., the individual zones observed in the EPMA analyses range from 0.4 – 10 µm in thickness. The beam size used in the Laser Ablation analyses was 40 µm and is too big relative to the individual zones to get trace element concentrations of individual zones. Two spots per grain, one in the core (~ 40 µm in diameter) and one in the rim (~ 40 µm in diameter), were analysed for comparison. Each spot was across multiple zones (approximately 4 zones, each with a thickness between 0.4 to 10 µm). The spot diameter is ~ 4 times bigger than the thickness of each zone. Despite the strong zoning patterns observed in EPMA analyses, there is no significant difference in trace element composition observed between the cores and the rims in the Laser Ablation analyses (e.g., Fig. 23).

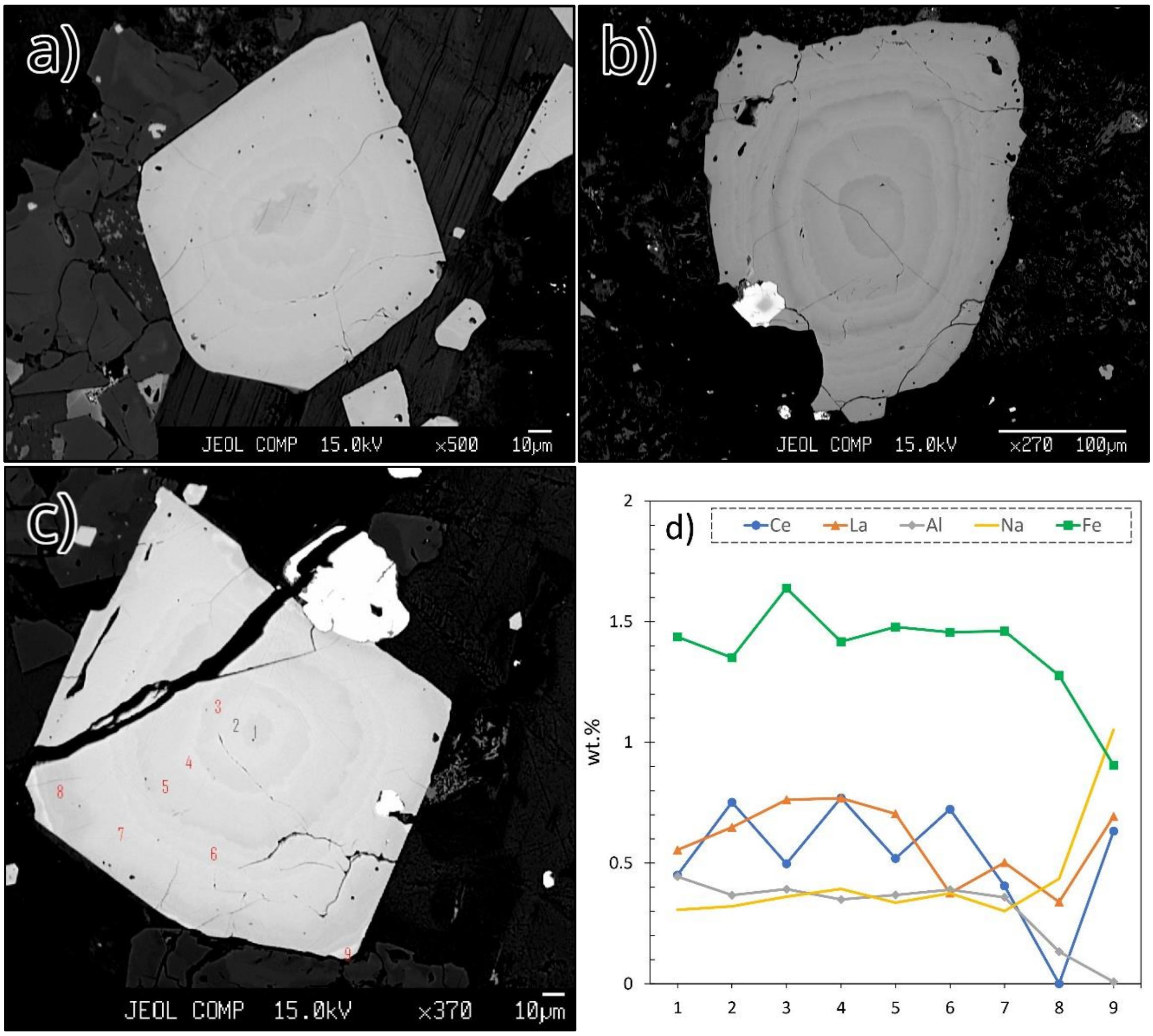

Fig. 21. Back-scattered electron (BSE) images of Weasua perovskite grains. (a) Perovskite from sample Y5747 showing complex oscillatory zoning. (b) Perovskite from sample Y5759 showing complex oscillatory zoning. (c) Perovskite from sample Y5747 with lighter and darker zoning pattern. The zoning is defined by variations in REE and Fe contents. (d) Major-element (Ce, La, Al, Na & Fe) profile for the grain shown in **Fig. 21**c. (e) Perovskite from sample Y5759 with lighter and darker zoning pattern. (f) Major-element (Ce, La, Al, Na & Fe) profile for the grain shown in **Fig. 21**e.

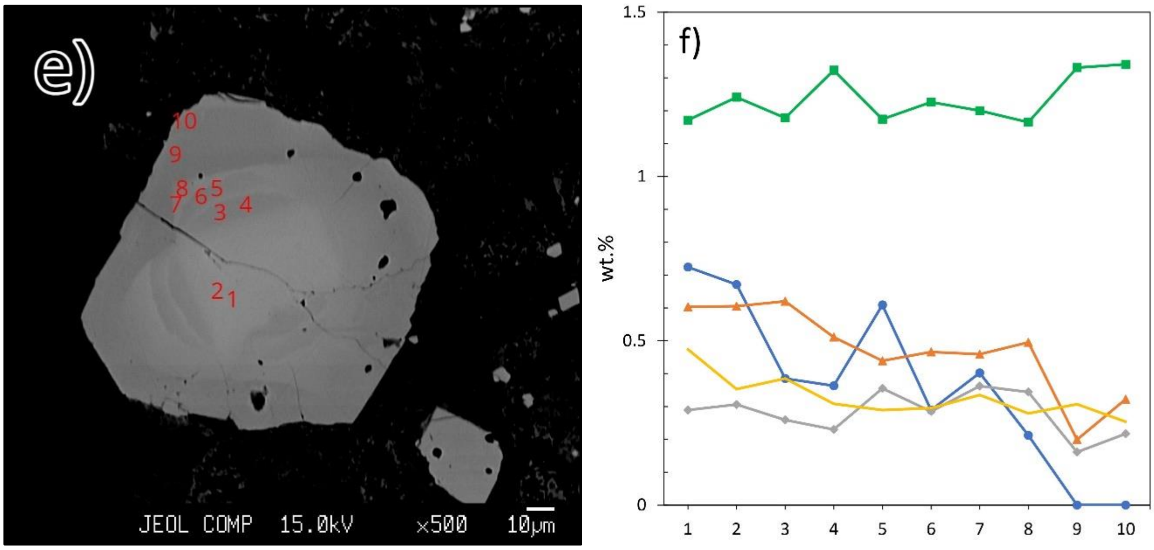

Fig. 21. *Continues*

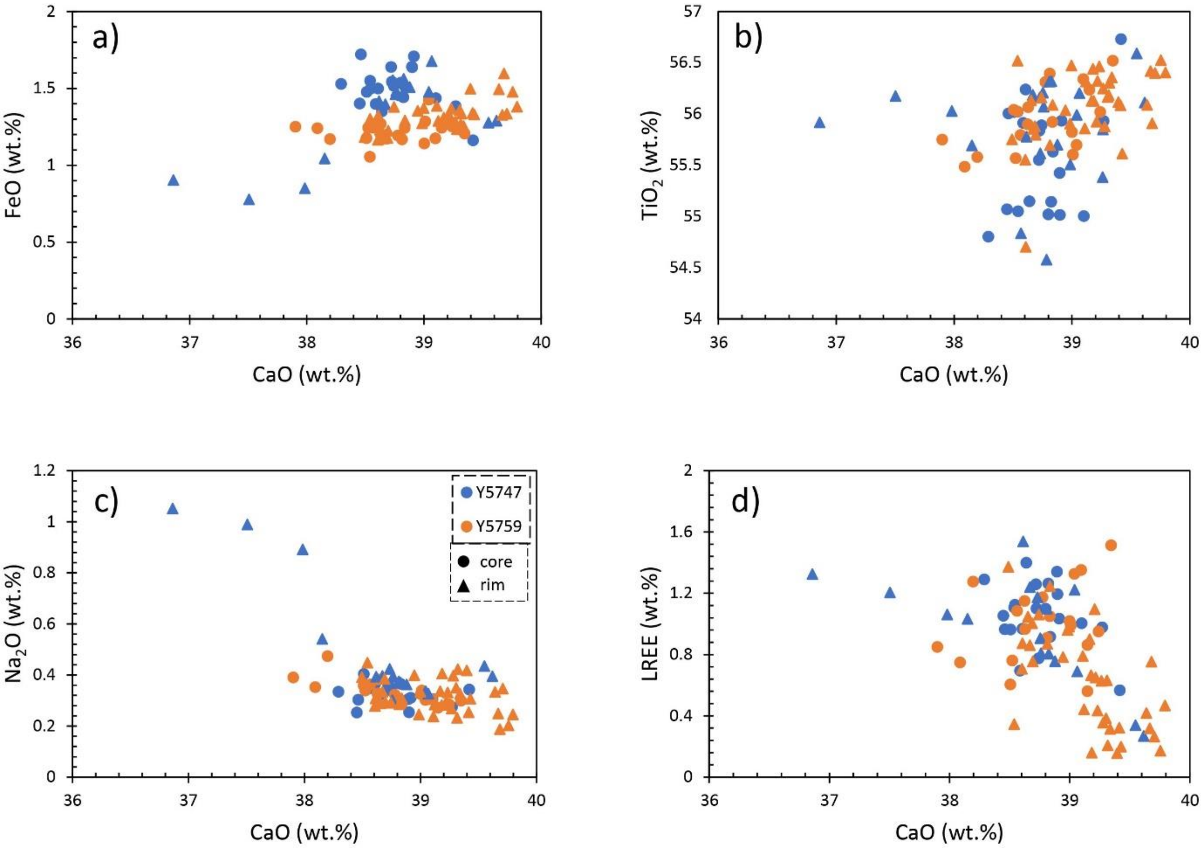

Fig. 22. Binary diagrams showing major element variations of the perovskites from Weasua, West Africa. CaO is plotted against FeO, TiO_2, Na_2O and LREE (as oxides). The FeO vs CaO (a) and TiO_2 vs CaO (b) diagrams show positive correlations, while Na_2O vs CaO (c) and LREE vs CaO (d) diagrams show negative correlations.

The perovskites from both samples are strongly enriched in LREE (Ce > La ≥ Nd > Pr), Nb, Sr and Th. In sample Y5747, Ce ranges from 13790 to 20020 ppm, La (6672 – 8330 ppm), Nd (5854 – 8318 ppm), Pr (1517 – 2142 ppm), Nb (4519 – 7130 ppm), Sr (2910 – 3320 ppm) and Th (1012 – 1743 ppm). These elements have the following ranges in sample Y5759; Ce (10820 – 19050 ppm), La (5860 – 8456 ppm), Nd (4030 – 9195 ppm), Pr (1085 – 2322 ppm), Nb (4245 – 5567 ppm), Sr (2794 – 6341 ppm) and Th (319 – 3024 ppm).

To plot the distribution patterns shown in Fig. 23, the perovskite REE data was normalised using chondrite values reported by Sun and McDonough (1989), i.e., equation (1).

The rest of the trace element data were normalised using primitive mantle values also reported by Sun and McDonough (1989), i.e., equation (2).

The REE distribution profiles (Fig. 23a) show smooth patterns enriched in LREE relative to HREE. The primitive mantle normalised trace element patterns (Fig. 23b) show negative anomalies of Ba, K, Pb, Sr and Zr-Hf. In sample Y5747, the La/Sm and Gd/Yb ratios for normalised data range from 5.41 to 6.35 and 23.7 to 51.9, respectively. In sample Y5759, the La/Sm and Gd/Yb ratios range from 5.29 to 6.93 and 19.70 to 46.4, respectively.

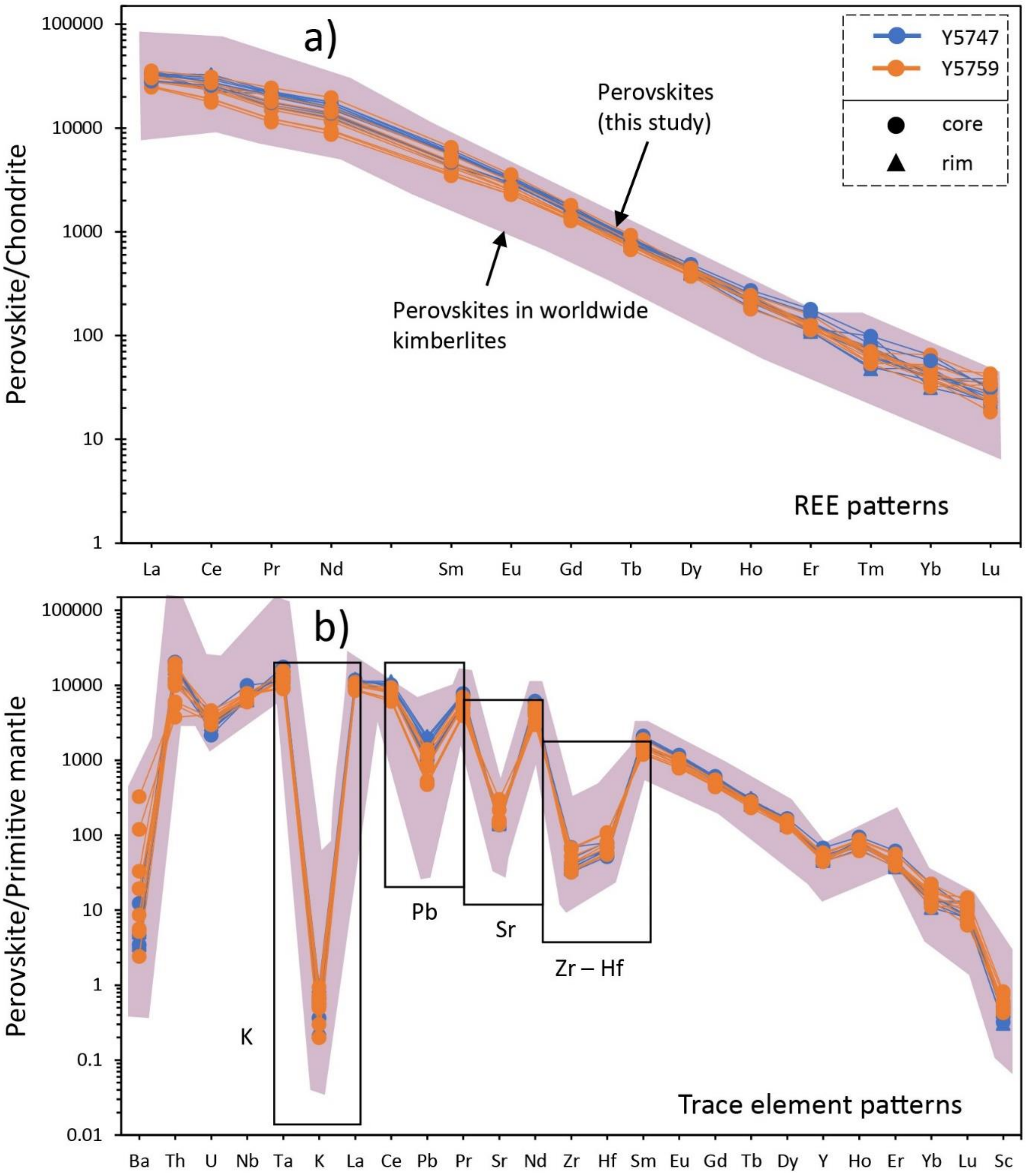

Fig. 23. Trace element composition of perovskite. (a) REE distribution patterns normalised to the chondrite values of Sun and McDonough (1989). (b) Trace element patterns normalised to the primitive mantle of Sun and McDonough (1989). The perovskite literature data are from: Lunda Norte kimberlites, NE Angola (Castillo-Oliver et al., 2016); Chicken Park, Iron Mountain, Udachnaya and Grizzly kimberlites (Chakhmouradian et al., 2013).

CHAPTER 5: Discussion

The previous section provided the petrography and bulk-rock geochemistry, as well as the chemistry of phlogopite, spinel (for Camp Alpha) and perovskite (for Weasua). In this section:

- The Camp Alpha and Weasua rocks will be classified based on mineralogy and mineral chemistry. The classification will aid in suggesting the more likely age for the Camp Alpha rocks.
- The parent magma compositions for Camp Alpha will be constrained (using the bulk-rock geochemistry), with interest in making a major element comparison with other West African diamondiferous rocks and worldwide kimberlites.
- Since no bulk-rock analysis was performed for the Weasua rocks, perovskite will be used as a proxy to calculate the trace element composition of the Weasua parent melt. The aim is to compare the trace element composition of Camp Alpha, Weasua and other West African diamondiferous rocks and kimberlites worldwide.
- Ultimately, the aim is to constrain the petrogenesis of West African diamondiferous rocks and evaluate the link between kimberlites and lamproites in cratonic regions.

5.1 Classification of the Camp Alpha and Weasua rocks

5.1.1 Camp Alpha

The Camp Alpha rocks in this study are mica-poor (relative to the Weasua rocks and nearby Tongo/Koidu kimberlites) and contain olivine and ilmenite macrocrysts, set in a groundmass of abundant spinel and primary calcite. There is no evidence of diopside (both primary and secondary) in any of the Camp Alpha samples. The mica-poor nature, presence of abundant ilmenite macrocrysts, groundmass calcite, and the absence of diopside strongly suggests that these Camp Alpha rocks are kimberlites, consistent with previous suggestions of Haggerty (2017).

In addition to the petrography, the Camp Alpha phlogopite is significantly enriched in Al_2O_3 but slightly depleted in FeO and TiO_2, exhibiting a kimberlite evolutionary trend (e.g., Fig. 14). The Camp Alpha spinel exhibits compositional zoning from chromite towards MUM (i.e., trend 1; Fig. 16). The spinel trends towards Fe^{3+}-enrichment and Cr-depletion. Trend 1 spinel compositional evolution is associated with kimberlites (e.g., Roeder and Schulze, 2008). Evidently, the mineral chemistry strongly suggests that the Camp Alpha rocks are kimberlites, further supporting petrographic observations.

5.1.2 Weasua

The Weasua rocks, in this study, are micaceous (phlogopite-rich) and contain primary groundmass diopside and calcite. The diopside is poikilitic and contains inclusions of groundmass olivine, spinel and perovskite. Additionally, the diopside is contained as inclusions in phlogopite, indicating a primary origin rather than replacing the groundmass phases. The petrography of the Weasua rocks resembles unevolved orangeites of the Kaapvaal Craton (i.e., primary diopside and calcite present, no evidence of sanidine, K-richterite, aegirine or leucite). Orangeites are unique to the Kaapvaal Craton and similar rocks are simply termed 'carbonate-rich olivine lamproites' (e.g., Pearson *et al.*, 2019). Therefore, the Weasua rocks are classified as carbonate-rich olivine lamproites, consistent with the classification suggested by Howarth and Giuliani (2020). Contrastingly, the Weasua rocks described by Skinner *et al.* (2004) did not contain magmatic diopside. Instead, the groundmass contained metasomatic diopside, occurring as a secondary phase and replacing original serpentinized olivine, phlogopite, opaque minerals and perovskite (Skinner *et al.*, 2004). As a result, Skinner *et al.* (2004) classified the rocks as kimberlites. Thus, it is likely that both kimberlites and lamproites are present within the Weasua cluster. Similar kimberlite-lamproite associations are observed elsewhere in the world. For example, the Wajrakarur Kimberlite Field in southern India comprises both kimberlites and lamproites (e.g., P3 kimberlite and P4 lamproite; Shaikh *et al*, 2018).

The mineral chemistry (phlogopite and spinel) reported by Howarth and Giuliani (2020) (for the exact same samples, Y5747 and Y5759) further support the lamproitic petrographic observations. The Weasua rocks in this study are, in conclusion, classified as carbonate-rich olivine lamproites.

5.2 Age of the Camp Alpha cluster

As previously mentioned, the exact age of the Camp Alpha cluster is unknown. The Weasua rocks are 800 Ma in age (e.g., Skinner *et al.*, 2004) and Haggerty (2017) suggested a Precambrian age for the Camp Alpha rocks. The other Liberian clusters, Kumgbo and Mano Godua, are suggested to be approximately 135 Ma in age (e.g., Skinner *et al.*, 2004). To evaluate if the Camp Alpha kimberlite and Weasua lamproite share a common asthenospheric source, their magmas need to be coeval (similar ages). Therefore, the age of the Camp Alpha kimberlite was approximated using both 135 Ma and 800 Ma.

The two ages, 135 Ma and 800 Ma, produce completely different εNd_i values (i.e., -16.3 to -7.44 at 135 Ma; 0.17 to 1.65 with two outliers, -2.33 and -8.41, at 800 Ma). If the age of the Camp Alpha dike is estimated at 135 Ma, the initial $^{87}Sr/^{86}Sr$ and εNd_i ranges are similar to those of the Vattikod lamproites (Fig. 19). Conversely, at 800 Ma the εNd_i values are similar to those of kimberlites ($\varepsilon Nd_i > 0$) and the initial $^{87}Sr/^{86}Sr$ ratio has a confined range (0.70265 – 0.70436; within the kimberlite range) (Fig. 19).

As discussed before (e.g., sections 4.1 and 5.1), the petrography and phlogopite/spinel chemistry of the Camp Alpha rocks are similar to those of kimberlites. These characteristics support the conclusion that the Camp Alpha rocks were generated from a kimberlite magma source rather than a lamproite source. Therefore, ~800 Ma is more likely the closest approximation of the age for the Camp Alpha cluster.

Much older kimberlites (Precambrian in age) usually have initial $^{87}Sr/^{86}Sr$ that is lower than present-day Bulk Silicate Earth (~0.7045); for example, Eastern Dharwar Craton kimberlites, India, with an age of 1083 ± 12 Ma to 1141 ± 14 (Chalapathi-Rao et al., 2013); Premier/Cullinan kimberlite with an age of 1150 ± 16 Ma (Wu et al., 2013). Conversely, younger kimberlites (few examples of mica-rich kimberlites) generally have initial $^{87}Sr/^{86}Sr$ ratios that are higher than Bulk Earth; for example, South African Cretaceous kimberlites (Becker and le Roex, 2006; Smith, 1983); Udachnaya kimberlite, Siberia, with an age of 347 ± 5 Ma (Maas et al., 2005); Tongo dike with an age of 140 Ma (Mathafeng, 2021) (Fig. 24a). The initial ^{87}Sr/^{86}Sr ratio (at 800 Ma) of the Camp Alpha cluster is lower than Bulk Earth and this strongly supports the older Precambrian age (800 Ma) for these rocks. The Precambrian age (800 Ma) for the Camp Alpha rocks implies that the Liberian kimberlite dike trend is much older than the Sierra Leone trend (Tongo ~ 140 Ma; Koidu ~ 146 Ma; Skinner *et al.*, 2004). The initial ^{143}Nd/^{144}Nd of Camp Alpha (800 Ma) and Tongo (140 Ma) kimberlites is higher than CHUR (e.g., Fig. 24b), suggesting a more depleted source (than CHUR) for these West African kimberlites.

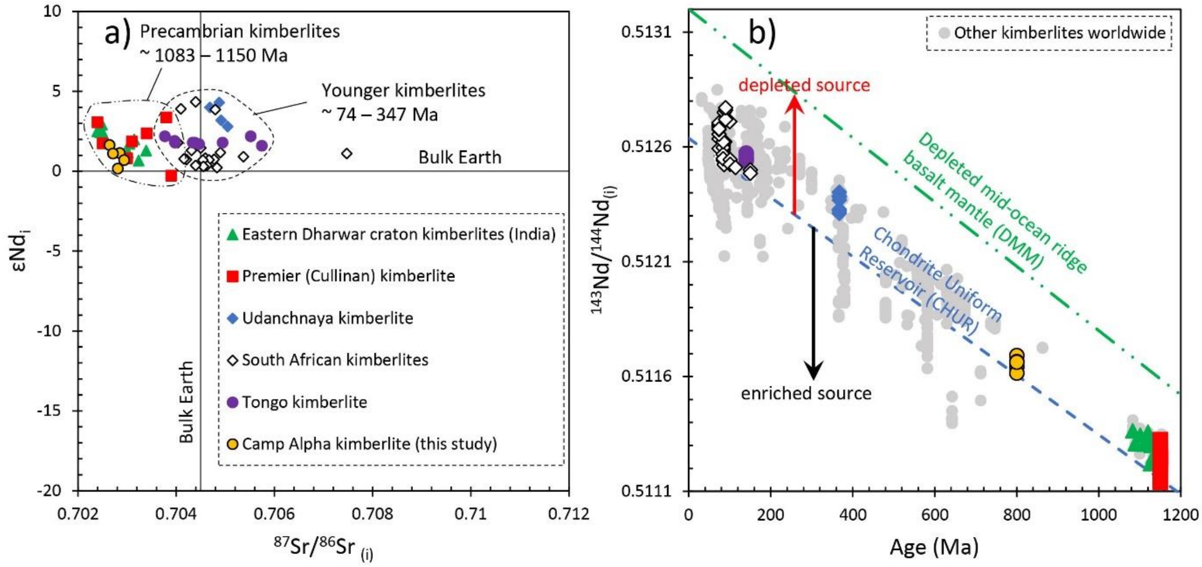

Fig. 24. The isotope composition of the Camp Alpha kimberlite at 800 Ma in comparison to other kimberlite regions. (a) εNd$_i$ vs initial ^{87}Sr/^{86}Sr ratio of the Camp Alpha rocks (at 800 Ma). The initial ^{87}Sr/^{86}Sr ratio is lower than Bulk Earth for older kimberlites but higher for younger kimberlites. (b) ^{143}Nd/^{144}Nd vs age. The Camp Alpha rocks originated from a depleted source. The Eastern Dharwar Craton (Chalapathi-Rao *et al.*, 2013), Premier Cullinan (Wu *et al.*, 2013), Udachnaya (Maas *et al.*, 2005), Tongo (Mathafeng, 2021), South African (Becker and le Roex, 2006; Smith, 1983) and other kimberlites worldwide (from Giuliani et al., 2021) are shown for comparison.

5.3 Constraining the parent melt composition of the Camp Alpha kimberlite

The close-to-parent melt composition for the Camp Alpha kimberlite will be calculated using bulk-rock geochemistry, with interest in comparing it (in section 5.3.3) with the parent melts of other West African rocks and kimberlites worldwide.

5.3.1 Evaluation of sample contamination

The hybrid nature of kimberlites, orangeites and lamproites means that the composition of the emplaced rock can be different from its parent melt composition due to contamination during sample preparation. Therefore, prior to estimating the close-to-parent melt composition, the effect of crustal xenolith and ilmenite macrocryst contamination and olivine macrocryst entrainment will be assessed in the following sections, following the approach of Clement (1982), Taylor *et al.* (1994) and Coe *et al.* (2008). The contaminated samples will then be excluded in the parent melt composition estimation.

5.3.1.1 Crustal xenolith and ilmenite contamination assessment

Kimberlites, lamproites and orangeites are hybrid in nature and comprise crustal and mantle xenoliths (Berg and Allsopp, 1972; Becker and le Roex, 2006; Giuliani and Pearson, 2019; Mitchell, 1986, 1995). The crustal and mantle xenoliths are undesirable during sample analysis and need to be carefully eliminated during sample preparation.

The West African rocks are known to contain considerable amounts of ilmenite xenocrysts (e.g., Haggerty, 2017; Skinner *et al.*, 2004; Taylor *et al.*, 1994). The Camp Alpha rocks in this study are no different and they contain ~ 2 to 18% ilmenite xenocrysts. To eliminate the influence of crustal xenoliths and ilmenite xenocrysts, the degree of contamination needs to be evaluated following the approaches outlined by Clement (1982) and Taylor *et al.* (1994).

The degree of crustal xenolith contamination in Camp Alpha rocks was assessed using a Contamination Index (C.I.; equation 8) developed by Clement (1982). The values lower than 1.5 are interpreted to be uncontaminated whereas those above are contaminated by crustal xenolith material (e.g., Clement, 1982; Taylor et al., 1994). Because West African kimberlites and lamproites contain ilmenite xenocrysts, the Ilmenite Index (Ilm.I.; equation 9) was used as outlined by Taylor *et al.* (1994). The rocks with Ilm.I. > 0.8 were considered highly contaminated (e.g., Taylor *et al*, 1994).

$$\mathrm{C.I.} = \frac{\mathrm{SiO_2+Al_2O_3+Na_2O}}{\mathrm{MgO+2K_2O}} \tag{8}$$

$$\mathrm{Ilm.I.} = \frac{\mathrm{FeO_T+TiO_2}}{\mathrm{MgO+2K_2O}} \tag{9}$$

Where:

- C.I. = Contamination Index
- Ilm.I. = Ilmenite Index

The major elements for dike samples were taken from Haggerty (2017), which are the same samples analysed in this study. The Camp Alpha samples contain low C.I. with a narrow range from 0.99 to 1.14 and plot within the kimberlite field. All samples contain C.I. < 1.5, indicating little to no effect from crustal contamination (Fig. 25a). The low C.I. values are consistent with the very low amount of crustal xenoliths observed in the petrography (<< 1%). In comparison, the Tongo (Mathafeng, 2021), Koidu (Taylor *et al.*, 1994) and Weasua (Skinner *et al.*, 2004) rocks show a wide range in C.I. (Tongo; C.I. ~ 0.82 – 1.54; Koidu; C.I. ~ 0.93 – 3.76), indicating a strong influence of crustal xenolith material on the rocks in some cases.

The majority of Camp Alpha samples (i.e., SC11 A1, SC11 A2, SC11 A3, SC11 A6, SC11 B2, SC11 B3, SC11 B4, SC11 B5 and SC11 B6) contain Ilm.I. that ranges from 0.37 to 0.71 (Fig. 25). One sample (i.e., SC11 A4) contains Ilm.I. > 0.8, indicating a significant ilmenite contamination effect (consistent with the high ilmenite abundance of 11 vol.% for this sample). The effect of ilmenite in sample SC11 A4 is reflected by very high TiO_2 content (6.36 wt.%) relative to estimated kimberlite melts (e.g., SA kimberlites with TiO_2 content of 2.58 ± 0.7 wt.%; Becker and le Roex, 2006). Thus, the sample SC11 A4 does not represent the parent magma composition.

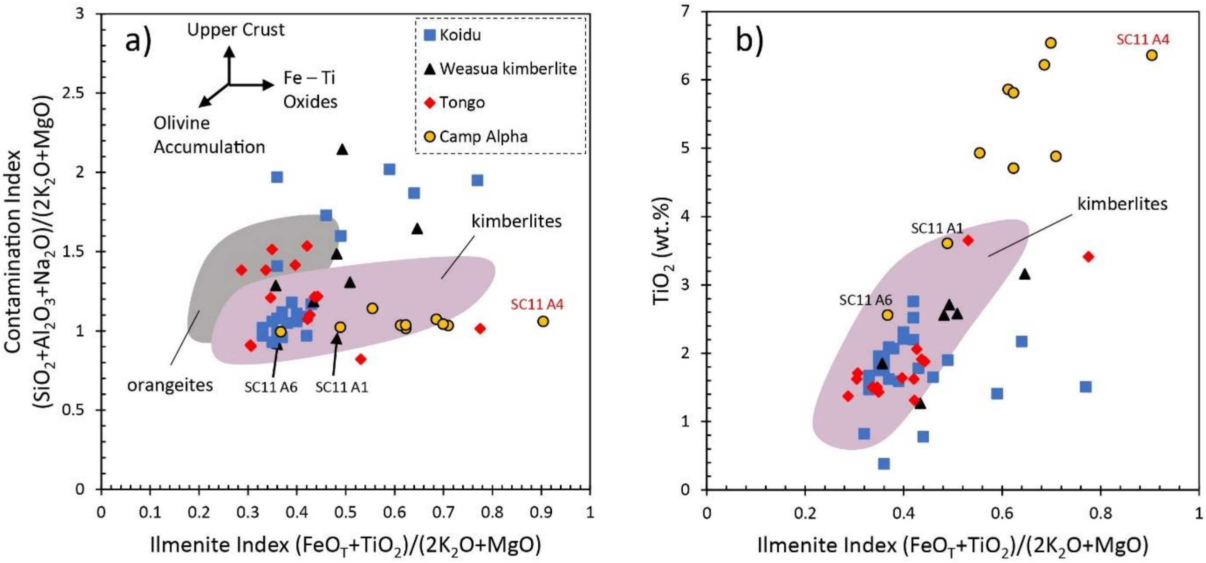

Fig. 25. Assessment of contamination in Camp Alpha samples (this study), Tongo (Mathafeng, 2021), Koidu (Taylor *et al.*, 1994) and Weasua (Skinner *et al.*, 2004) clusters, by using the Contamination Index (Clement, 1982) and Ilmenite Index (Taylor *et al.*, 1994). The bulk-rock literature data used to construct the fields are from: kimberlite (Becker and le Roex, 2006; Harris *et al.*, 2004; le Roex *et al.*, 2003); orangeites (Becker and le Roex, 2006; Coe *et al.*, 2008; Howarth *et al.*, 2011).

The effect of ilmenite contamination on Camp Alpha kimberlite samples was evaluated following the approach of Taylor *et al.* (1994) (which resulted in the elimination of sample SC11 A4; Ilm.I. > 0.8). However, the TiO_2 vs Ilm.I. variation (Fig. 25b) demonstrates that the TiO_2 content is heavily controlled by ilmenite (i.e., TiO_2 increases significantly with elevated Ilm.I.). As a result, only two samples (i.e., SC11 A6; TiO_2 ~ 2.56 wt.%, Ilm.I. ~ 0.37 and SC11 A1; TiO_2 ~ 3.61 wt.%, Ilm.I. ~ 0.49) contain low TiO_2 content (similar to 2.58 ± 0.7 wt.% TiO_2 of SA kimberlites; Becker and le Roex, 2006). This low TiO_2 and Ilm.I. indicates low influence by ilmenite contamination and consistent with low ilmenite abundances (2 vol.% for SC11 A1 and 8 vol.% for SC11 A6). The rest of the samples (i.e., SC11 A2, SC11

A3, SC11 A4, SC11 B2, SC11 B3, SC11 B4, SC11 B5 and SC11 B6) contain high TiO_2 content (4.71 – 6.54 wt.%; Ilm.I. ~ 0.55 – 0.99; also plotting outside the kimberlite filed), indicating a significant influence of ilmenite xenocrysts.

5.3.1.2 Olivine macrocrysts entrainment

Kimberlites and lamproites are characterised by an inequigranular texture where macrocrysts usually dominate the rock. However, aphanitic (absence of macrocrysts) kimberlite varieties are also common (e.g., le Roex *et al.*, 2003). Macrocrystic and aphanitic rocks experience different processes prior to their emplacement (e.g., Harris *et al.*, 2004; le Roex *et al.*, 2003). Aphanitic varieties lose macrocrysts through fractional crystallisation, a process that can also result in the loss of other crystals such as phlogopite and diamonds. Macrocrysts, such as olivine, are believed to represent mantle peridotite material that is entrained by the kimberlite melt (e.g., Becker and le Roex., 2006; Clement, 1982; Harris *et al.*, 2004; le Roex *et al.*, 2003). As a result, macrocrystic varieties do not represent liquid compositions, whereas aphanitic samples may more closely resemble the parent magma composition (e.g., le Roex *et al.*, 2003). However, this idea is now well known to be incorrect because olivine cores are xenocrystic and due to ubiquitous serpentinization (e.g., Giuliani, 2018).

The Camp Alpha samples are all macrocrystic and contain abundant olivine (27 to 63 vol.%). In order to estimate the composition of the kimberlite melt, the effect of olivine macrocryst incorporation needs to be assessed. The entrainment of peridotite material will result in an increase in SiO_2 content, compatible trace elements in olivine (e.g., Cr, Ni and Co) concentrations, and Mg# (e.g., Becker and le Roex., 2006; Coe *et al.*, 2008; Harris *et al.*, 2004; le Roex *et al.*, 2003). The effect of olivine macrocryst entrainment in the Camp Alpha rocks is assessed using the approach of Coe *et al.* (2008) (i.e., K_2O vs Ni and Ni vs MgO variations). The Camp Alpha olivine is completely serpentinised and using Ni for samples where olivine is completely serpentinised is not the best approach because serpentine contains very little Ni and bulk majors may be affected. However, this approach is the best possible for these highly altered Camp Alpha samples.

The composition of samples affected by olivine macrocryst entrainment will have increased Ni and MgO contents and will trend towards mantle lherzolite compositions (Coe *et al.*, 2008). The Camp Alpha samples trend towards the garnet lherzolite composition, and the Ni and MgO contents increase significantly indicating an effect of olivine entrainment on analysed samples (Fig. 26). All samples contain very high MgO content > 30 wt.% (32.1 – 40.3 wt.%) (Fig. 26b), however, there is a large range in Ni concentration (i.e., samples range from relatively low Ni to very high Ni content). As a result, the influence of olivine macrocrysts entrainment will be assessed by using Ni content (since there is a large variation). Samples that contain Ni content > 1000 ppm are considered highly contaminated. The majority of the samples (i.e., SC11 A1, SC11 B2, SC11 B3, SC11 B4, SC11 B5 and SC11 B6) have Ni content that ranges from 496 to 1096 ppm. These samples indicate a relatively low influence of olivine entrainment. The rest of the samples (i.e., SC11 A2, SC11 A3, SC11 A4 and SC11 A6) plot higher in the field towards the garnet lherzolite composition (Fig. 26a) and contain Ni content > 1000 ppm, indicating significant olivine entrainment.

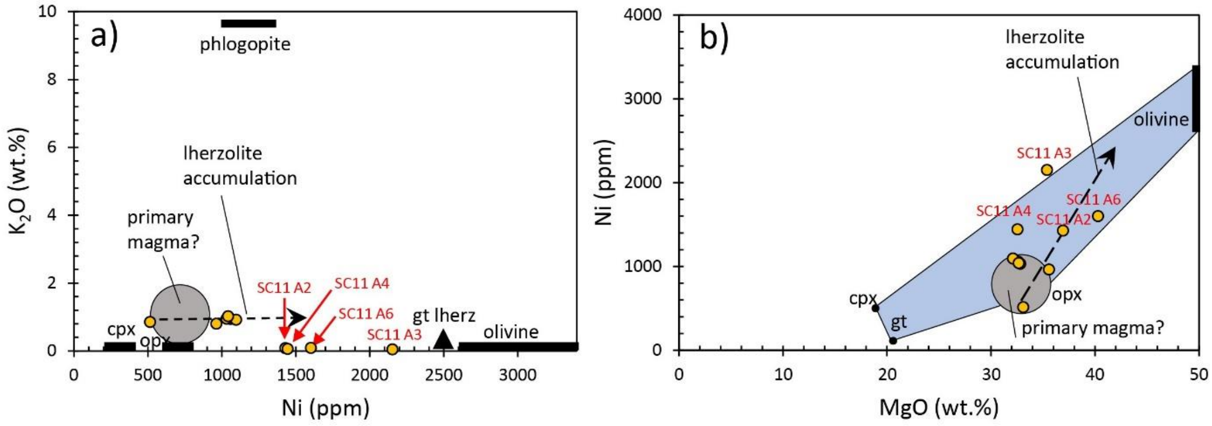

Fig. 26. Plots showing the effect of olivine macrocryst entrainment in the Camp Alpha samples. (a) K_2O vs Ni and (b) MgO vs Ni (adopted from Coe *et al.* (2008)).

5.3.2 Close-to-parent magma composition

To estimate the close-to-parent melt composition of the Camp Alpha kimberlite is not straightforward due to contamination by ilmenite and olivine macrocrysts. In summary

(Table 5), only sample SC11 A1 best represents the composition of Camp Alpha kimberlite parent melt (i.e., low crustal, ilmenite contamination and olivine entrainment effect). The Camp Alpha samples contain abundant ilmenite (up to 17 vol.%). Some ilmenite contamination may have occurred and the TiO_2 content may be a little high.

Table 5. Summary of excluded samples from the estimation of Camp Alpha kimberlite close-to-parent melt

Sample	Reason for exclusion
SC11 A2	ilmenite contamination and olivine entrainment
SC11 A3	ilmenite contamination and olivine entrainment
SC11 A4	ilmenite contamination and olivine entrainment
SC11 A6	Olivine entrainment
SC11 B2	ilmenite contamination
SC11 B3	ilmenite contamination
SC11 B4	ilmenite contamination
SC11 B5	ilmenite contamination
SC11 B6	ilmenite contamination

Table 6. Average major element composition of the close-to-parent magma for the Camp Alpha kimberlite (this study) in comparison to South African kimberlites and orangeites (Becker and le Roex, 2006), Tongo dike (Mathafeng, 2021), Koidu (Taylor *et al.*, 1994) and Weasua kimberlite (Skinner *et al.*, 2004).

	Camp Alpha kimberlite	South African kimberlite		South African orangeite		Micaceous Tongo kimberlite		Micaceous Koidu kimberlite		Weasua kimberlite	
	comp.	Av. comp.	SD	Av. comp.	SD	Av. Comp.	SD	Av. Comp.	SD	Av. Comp.	SD
wt.%											
SiO_2	34.2	26.1	2.70	33.9	4.80	28.2	3.90	31.9	2.30	33.5	1.30
TiO_2	3.61	2.58	0.70	1.77	1.50	1.71	0.30	2	0.35	2.33	0.42
Al_2O_3	3.77	2.76	0.45	3.76	2	4.08	1	2.28	0.55	3.32	0.81
Fe_2O_{3T}	14.6	10.7	1.20	8.76	0.60	10.2	1.70	3.71	0.83	9.80	1.51
MnO	0.23	0.19	0.03	0.18	0.05	0.19	0.01	0.18	0.03	0.27	0.09
MgO	35.6	25.2	2.10	23.2	4.20	21	1	27.3	2.43	24.17	1.35
CaO	5.64	13.3	2.20	9.96	2	12.5	1.80	8.31	1.87	8.44	1.56
Na_2O	0.06	0.16	0.14	0.25	0.24	0.18	0.02	0.07	0.03	0.01	-
K_2O	0.80	0.83	0.46	3.63	1.40	3.03	0.50	1.43	0.72	0.91	0.48
P_2O_5	0.23	2.04	1.20	1.85	0.80	1.65	0.60	0.60	0.41	0.45	0.13

5.3.3 Major element composition of the Camp Alpha parent melt in comparison with other West African diamondiferous rocks

The West African diamondiferous rocks exhibit significant variations in terms of their mineralogy and petrography (see section 2.3.2), indicating a difference in the major element composition of the melts from which these rocks crystallized. The calculated close-to-parent melt composition for the Camp Alpha kimberlite is compared with the parent melts of other West African rocks and kimberlites worldwide.

The estimated composition of the Camp Alpha kimberlite parent melt (best represented only by sample SC11 A1) is presented in Table 6. It is acknowledged that the Camp Alpha samples are highly altered and that they may not represent the parent melt composition. Thus, the calculation of the parent melt for these highly altered Camp Alpha samples may not be the best approach, but the best possible approach for these samples. This parent melt contains 34.3 wt.% SiO_2, TiO_2 (3.61 wt.%), Al_2O_3 (3.77 wt.%), Fe_2O_3 (14.58 wt.%), MgO (35.6 wt.%), CaO (5.64 wt.%) and K_2O (0.80 wt.%). The composition of the Camp Alpha kimberlite parent melt is, overall, similar to the magma composition of kimberlites (e.g., lower K_2O reflecting mica-poor nature and higher TiO_2 reflecting a high abundance of Ti-rich spinel, perovskite and ilmenite, in comparison to orangeites for example). Noticeably, the MgO content is significantly higher than both kimberlites and orangeites of the Kaapvaal Craton (possibly still indicating contamination by olivine xenocrysts).

The Camp Alpha, Koidu (Taylor *et al.*, 1994) and Weasua (Skinner *et al.*, 2004) kimberlites contain high SiO_2 content (i.e., 34.3, 31.9 ± 2.30 and 33.5 ± 1.30 wt.%, respectively, similar to 33.9 ± 4.80 wt.% of orangeites) relative to Tongo kimberlite (Mathafeng, 2021) and South African kimberlites. Most importantly, the Camp Alpha and Weasua kimberlites are mica-poor and contain low K_2O contents (i.e., 0.80 wt.% and 0.91 ± 0.13 wt.%, respectively; similar to 0.83 ± 0.46 wt.% of South African kimberlites) in comparison to the highly micaceous Tongo and Koidu kimberlites. The Tongo and Koidu kimberlites are mica-rich like orangeites, and this is reflected in their high K_2O contents (K_2O: Tongo ~ 3.03 ± 0.50 wt.%; Koidu ~ 1.43 ± 0.72 wt.%; orangeites ~ 3.63 ± 1.40 wt.%) (Table 6). The Tongo and Koidu kimberlites represent a rare micaceous kimberlite magmatism that is also observed in the Kaapvaal Craton (e.g., mica-rich Jagersfontein kimberlite; Taylor, 1998).

5.4 Melt composition of the Weasua lamproite at the time of perovskite crystallization

The formation of perovskite will be constrained with interest in using its trace element concentrations as a proxy for the parent melt composition of the Weasua lamproite. The aim is to compare (in section 5.4.3) the Weasua lamproite parent melt trace element composition with the parent melts of other West African rocks and kimberlites worldwide.

5.4.1 Formation of perovskite

The Weasua perovskites show a significant range in major elements. The binary diagrams and major element profiles show that for each perovskite grain, there are major element variations from the core to the rim. For example, in sample Y5759 the cores are slightly enriched in $(LREE)_2O_3$ compared to the rims. The LREE are strongly compatible ($D_X > 5.0$; e.g., Chakhmouradian *et al.*, 2013), thus, the core-ward increase in $(LREE)_2O_3$reflects incompatibility in the kimberlite melt during igneous differentiation.

Chakhmouradian and Mitchell (2000) noted that kimberlitic perovskite rarely shows oscillatory zoning and that if present, it is usually defined by variations in Ti, Ca, Nb and LREE. However, oscillatory zoning has been reported in some kimberlites and lamproites worldwide (e.g., kimberlites in Lunda Norte province, NE Angola, described Castillo-Oliver *et al.* (2016) and the West Kimberly lamproites, Western Australia, described by Jaques (2016)). Castillo-Oliver et al. (2016) and Jaques (2016) observed oscillatory zoning with sharp euhedral boundaries, indicating that the perovskite grains were involved in multi-stage processes during crystallisation. Castillo-Oliver *et al.* (2016) proposed that oscillatory zoning reflects magma mixing and crystallization in different conditions. Oscillatory zoning to this scale may also be a crystal-chemical process that has little petrogenetic meaning (e.g., Shore and Fowler, 1996).

The perovskites analysed in this study (e.g., Fig. 27b) show a different style of oscillatory zoning compared to those reported by Castillo-Oliver *et al.* (2016) (e.g., Fig. 27a). The perovskites in this study typically have rounded concentric zones with no sharp edges, i.e., anhedral grain boundaries. This also indicates multi-stage processes during crystallisation where each zone represents a different stage of evolution or growth. However, between each new stage of growth, the grains were resorbed, which resulted in rounded concentric zones.

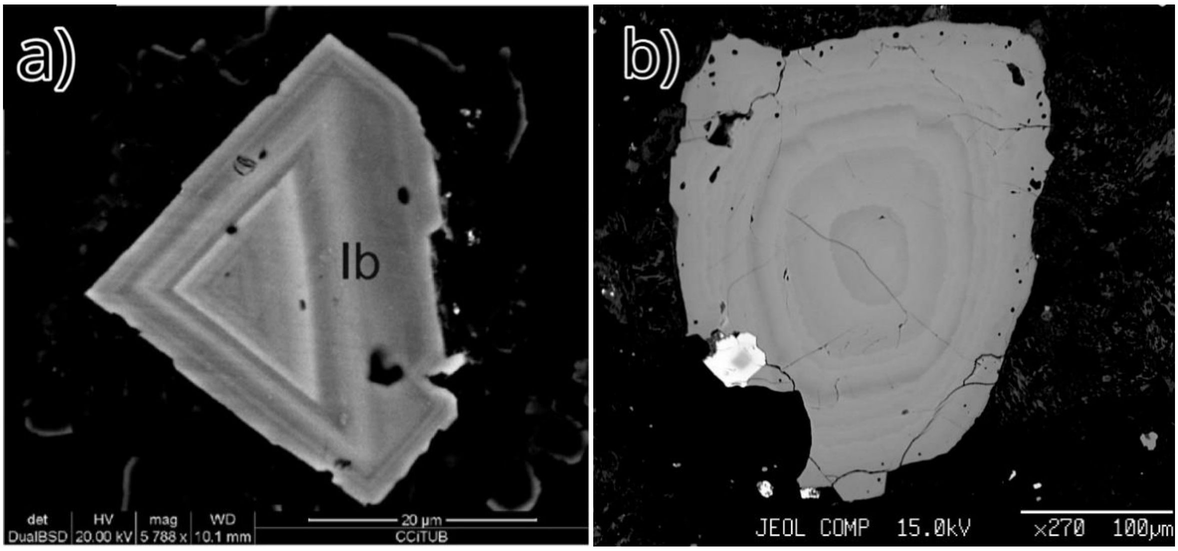

Fig. 27. Comparison of the style of oscillatory zoning for perovskites reported by Castillo *et al.* (2016) (a) and perovskites reported in this project (b). The perovskites described in this study show rounded zones, whereas the grains described by Castillo *et al.* (2016) have sharp euhedral zones.

5.4.2 Melt composition at the time of perovskite crystallisation

The trace element data produced by LA-ICP-MS shows no significant variations between the samples Y5747 and Y5759. Additionally, there is no significant difference in trace element composition observed between the cores and the rims (e.g., Fig. 23 & 28). Therefore, in the discussion below the cores and rims, and both samples will be discussed together rather than separately.

Since the trace element concentrations for cores and rims are similar, the perovskite data can be used to calculate the parent magma composition from which the perovskite crystallised. During the evolution of different carbonate and silicate melts, trace elements are fractionated between minerals and the melt. The crystallisation of perovskite plays an important role by incorporating trace elements that contain information about the nature of the primary magma (e.g., Beyer et al., 2013; Chakhmouradian et al., 2013). One of the objectives of this study is to determine the original composition of the Weasua melt. This can be done by using known kimberlite-perovskite partition coefficients described in the literature. The Weasua rocks are lamproites, however, no element partition coefficients between perovskite and lamproite melt have been reported. Therefore, kimberlite – perovskite partition coefficients were used, as the next best approach. An inversion of trace element data for the perovskites was performed using the partition coefficients published by Chakhmouradian *et al.* (2013), to determine the composition of the melt in equilibrium with perovskite at the time of crystallisation. Equation (10) was used to calculate this equilibrium melt composition.

$$D_i = \frac{c_{i,\ crystal}}{c_{i,\ melt}} \tag{10}$$

Where:

- i = trace element of interest
- D_i = partition coefficient for the trace element (i),
- $c_{i,\ crystal}$ = concentration of trace element (i) measured in the mineral,
- $c_{i,\ melt}$ = concentration of trace element (i) in the melt.

The calculated trace element data for the melt are presented in Table 7. The calculated melt shows smooth sub-parallel chondrite normalised REE patterns (normalised to the values of Sun and McDonough (1989); Fig. 28a) and enrichment in light REE relative to heavy REE (e.g., LREE; La ~ 700 – 1100 × chondrite, HREE; Lu ~ 6 – 12 × chondrite. La/Yb_N ~ 50 – 140). The primitive mantle normalised trace element patterns (Fig. 28b) are smooth and sub-parallel and show strong enrichment in highly incompatible elements (e.g., ~ 26 – 400 × primitive mantle) relative to HREE (e.g., Er to Lu; ~ 1 – 2 × primitive mantle). The REE and trace element patterns of the calculated melt are consistent with the calculated melts of kimberlites worldwide based on both perovskite and whole rock data (e.g., based on perovskite: Lunda Norte province kimberlites, NE Angola; Castillo-Oliver *et al.*, 2016; Chicken Park, Iron Mountain, Udachnaya and Grizzly kimberlites; Chakhmouradian *et al.*, 2013; based on whole rock: South African kimberlites; Becker and le Roex, 2006) (Fig. 28).

The calculated Weasua melt contains Ba/Nb ratios that range from 8.67 to 27.9 La/Nb (0.47 – 0.92) and Ce/Pb (18.2 – 66.8). These ratios are similar to those of kimberlites (e.g., Fig. 30) and in contrast with the petrography and mineral chemistry (which look similar to lamproites). Thus, based on the mineralogy and phlogopite composition the Weasua rocks are clearly lamproites, however, geochemically the parent melt has similar trace element ratios to kimberlite worldwide.

Table 7. Average trace element composition of the calculated equilibrium melt for Weasua rocks.

Weasua lamproite melt (calculated from perovskite)								
	Av. comp.	SD		Av. comp.	SD		Av. comp.	SD
ppm			ppm			ppm		
Sc	35.51	12.81	Pr	35.10	7.43	Tm	0.27	0.06
Rb	12184	7609	Nd	126.94	27.62	Yb	1.84	0.40
Sr	2656	647.31	Sm	17.12	3.11	Lu	0.25	0.06
Y	26	3.04	Eu	4.95	0.65	Hf	8	1.97
Zr	357.96	102.97	Tb	1.47	0.13	Ta	7.01	1.49
Nb	314.89	40.63	Gd	10.88	1.18	Pb	11.93	5.49
Ba	31013	76088	Dy	5.70	0.42	Th	8.03	3.76
La	226.32	25.44	Ho	0.86	0.09	U	3.83	0.83
Ce	385.37	62.26	Er	2.13	0.31			

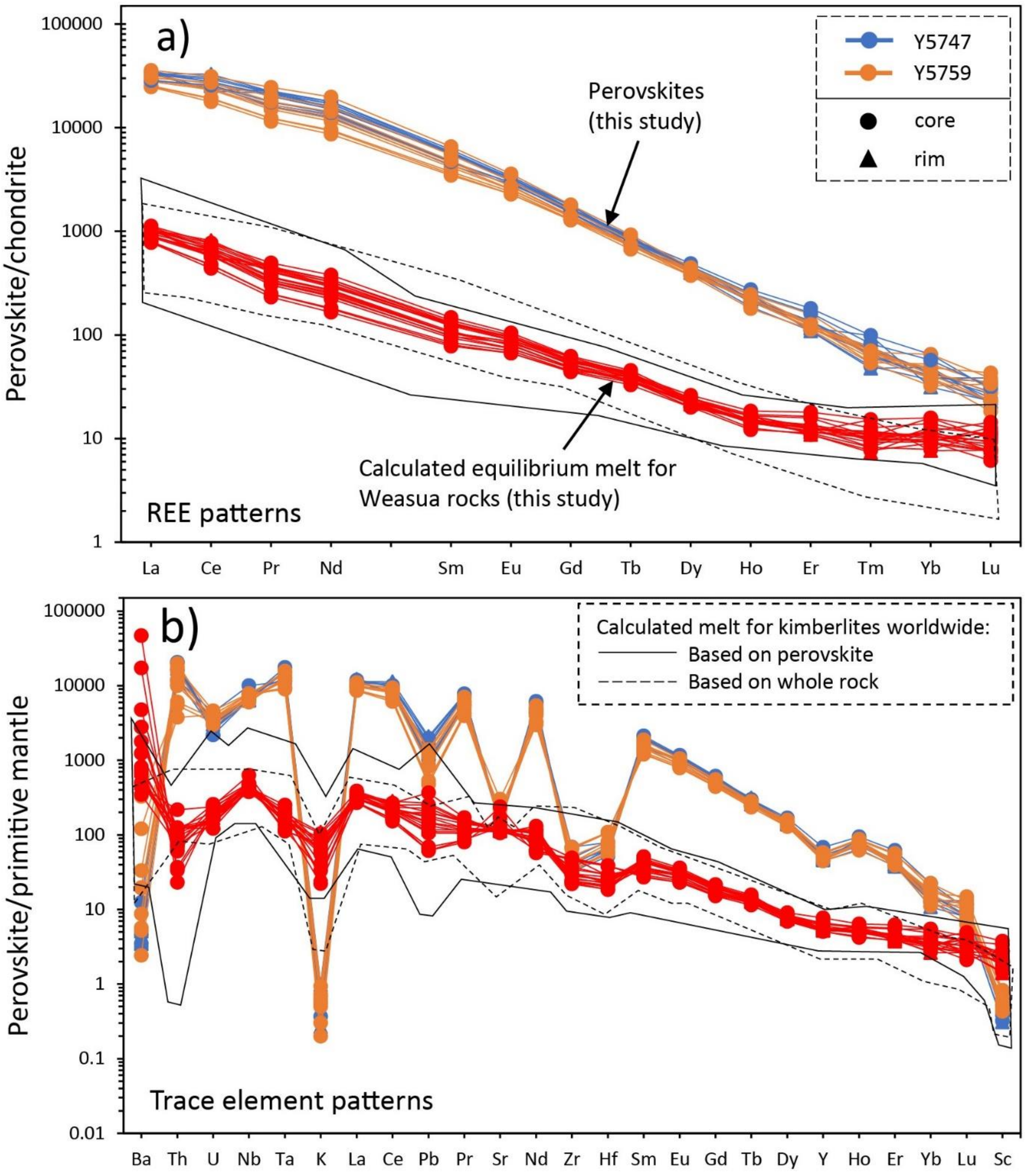

Fig. 28. Trace element composition of perovskite and the calculated equilibrium melt. (a) REE distribution patterns normalised to the chondrite values of Sun and McDonough (1989). The equilibrium melt is depleted in REEs relative to the perovskite. (b) Trace element patterns normalised to the primitive mantle of Sun and McDonough (1989). The equilibrium melt is depleted in trace elements but enriched in Ba and K, relative to the perovskite. The calculated melt for kimberlites worldwide based on perovskite (solid line; Castillo-Oliver *et al.*, 2016; Chakhmouradian *et al.*, 2013) and whole rock (dotted line; Becker and le Roex, 2006) are plotted for comparison.

5.4.3 Comparison of the trace element composition for West African diamondiferous rocks

The West African diamondiferous rocks exhibit significant variations in terms of their mineralogy, petrography and major element composition. However, the melts of the Camp Alpha kimberlite, micaceous Tongo and Koidu kimberlites, and Weasua lamproite, contain similar trace element compositions. All the above-mentioned clusters show smooth sub-parallel chondrite normalised REE patterns and enrichment in light REE relative to heavy REE (Fig. 29a, b, c & d). The chondrite normalised REE patterns of the West African rocks are similar to each other and those of South African and Wajrakarur (India) kimberlite magmas.

All West African clusters show smooth sub-parallel primitive mantle normalised trace element patterns (Fig. 29e, f, g & h) and strong enrichment in highly incompatible elements, with HREE showing least enrichment. Similarly to South African and Wajrakarur (India) kimberlite magmas, the Camp Alpha kimberlite, micaceous Tongo and Koidu kimberlites, Weasua kimberlite and lamproite, are characterised by depletion (negative anomaly) in Rb, K, Sr, Hf-Zr and Ti elements (however, the negative Sr anomaly is not observed in the Weasua lamproite; Fig. 29f). The primitive mantle normalised trace element patterns of the West African rocks are similar to each other and those of South African and Wajrakarur (India) kimberlite magmas.

One of the ways to discriminate kimberlites from orangeites/lamproites is by using trace element ratios (e.g., Becker and le Roex, 2006). Becker and le Roex (2006) showed that kimberlites are typically characterised by Ce/Pb > 22 and La/Nb < 1.10. Conversely, orangeites are typically characterised by Ce/Pb < 22 and La/Nb > 1.10. Lamproites exhibit a very wide range in composition. However, they show close geochemical similarities to orangeites, rather than to kimberlites. In addition to the chondrite and primitive mantle normalised patterns, the trace element ratios (Ba/Nb, La/Nb and Ce/Pb) of Camp Alpha, Weasua, Tongo, Koidu kimberlites and Weasua lamproite are similar to each other and those of kimberlite magmas worldwide (Fig. 30).

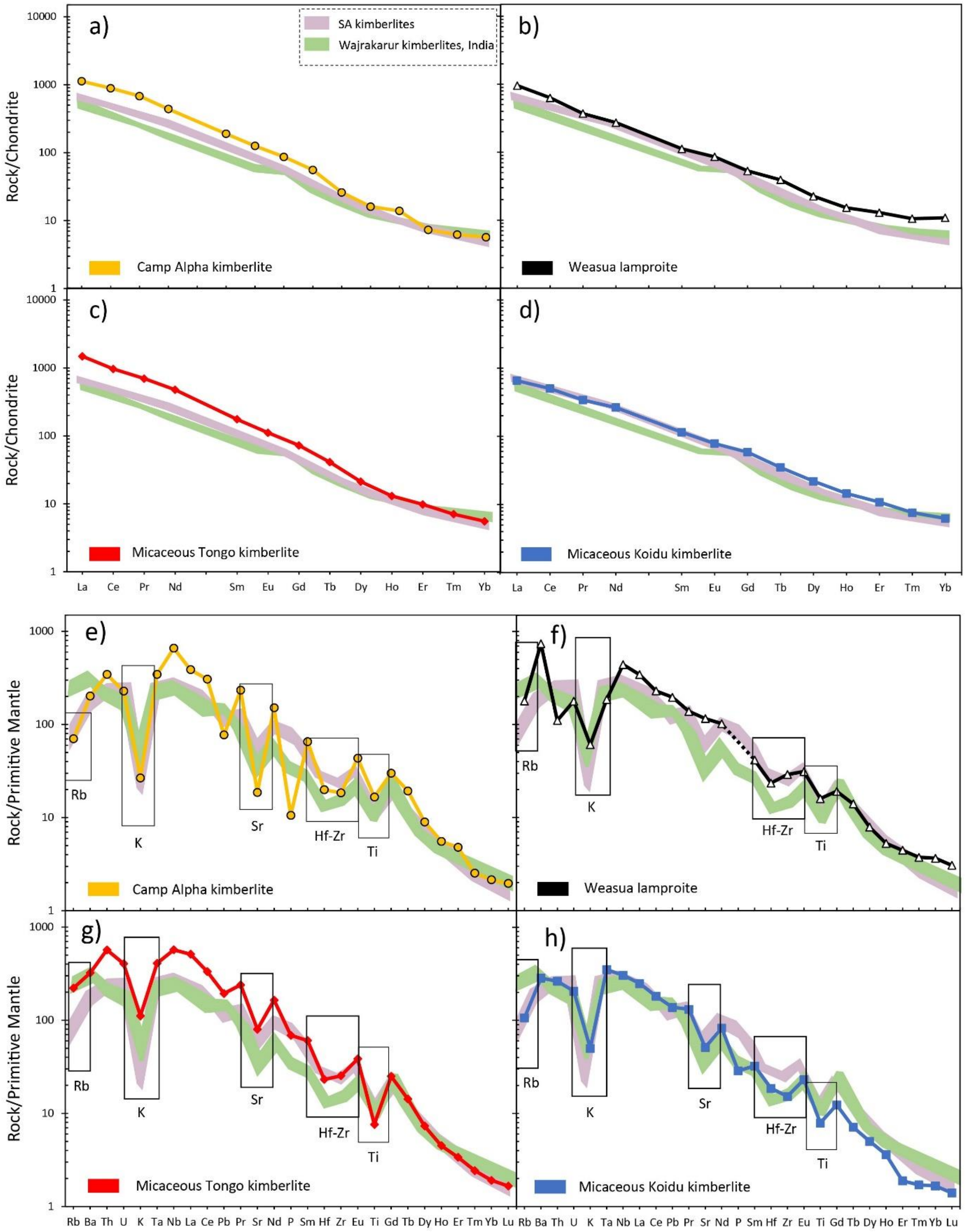

Fig. 29. Averaged Chondrite-normalised REE (plot a, b, c & d) and Primitive mantle-normalised trace element (plot e, f, g & h) patterns of West African diamondiferous rocks (data from: Camp Alpha and Weasua lamproite; this study; Tongo Mathafeng, 2021; Koidu; Taylor *et al.*, 1994; Weasua kimberlite; there was not enough trace element data to make comparison) normalised to the

values of Sun and McDonough (1989). The average South African kimberlites (bulk-rock data are from: le Roex *et al.*, 2003; Harris *et al.*, 2004; Becker and le Roex, 2006) and Wajrakarur kimberlites, India (bulk-rock data are from: Chalapathi-Rao *et al.*, 2004) are plotted for comparison. The patterns are similar for the West African rocks, South African and Wajrakarur kimberlites.

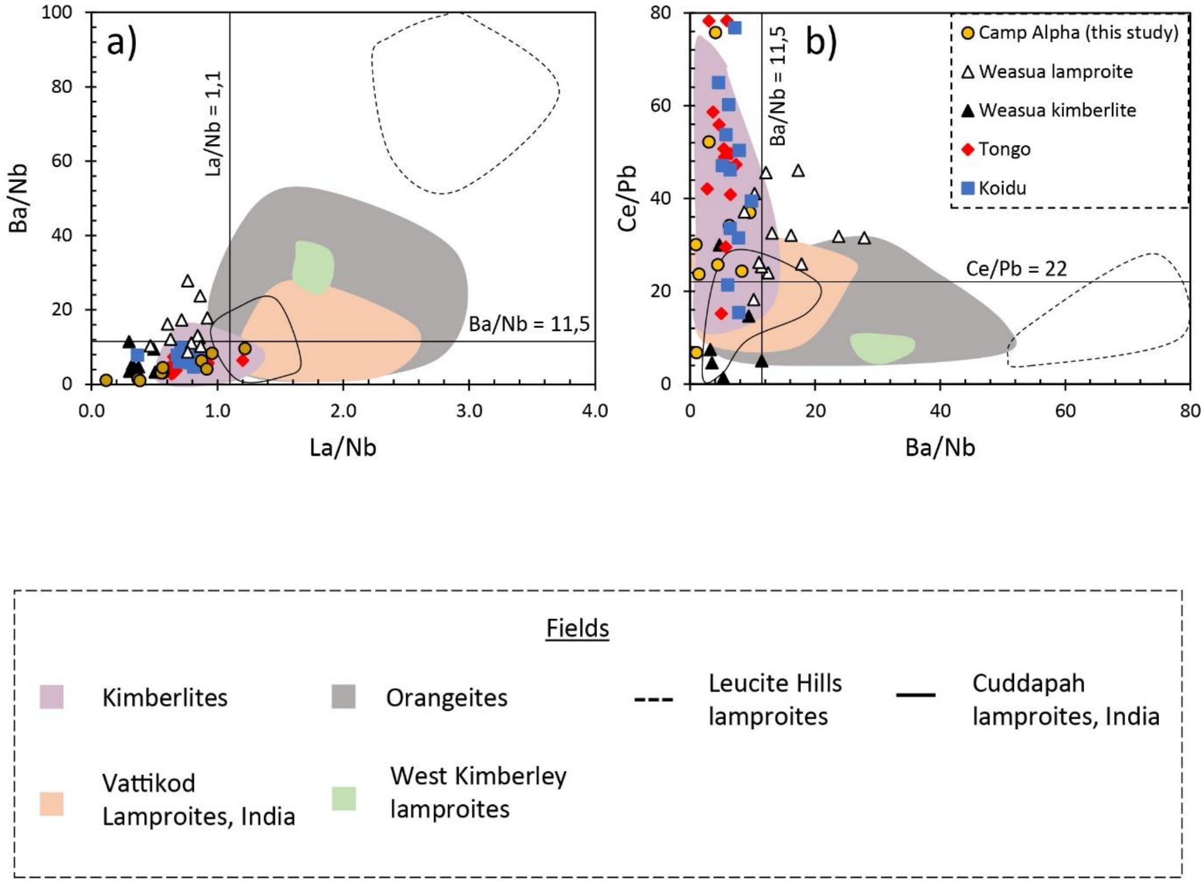

Fig. 30. (a) Ba/Nb vs La/Nb and (b) Ce/Pb vs Ba/Nb for the West African diamondiferous rocks (Camp Alpha and Weasua lamproite; this study; Weasua kimberlite; Skinner *et al.*, 2004; Tongo; Mathafeng, 2021; Koidu; Taylor *et al.*, 1994). The ratios are similar for the West African rocks and kimberlites worldwide. The bulk-rock literature data used to construct the fields are the same as in **Fig. 6**.

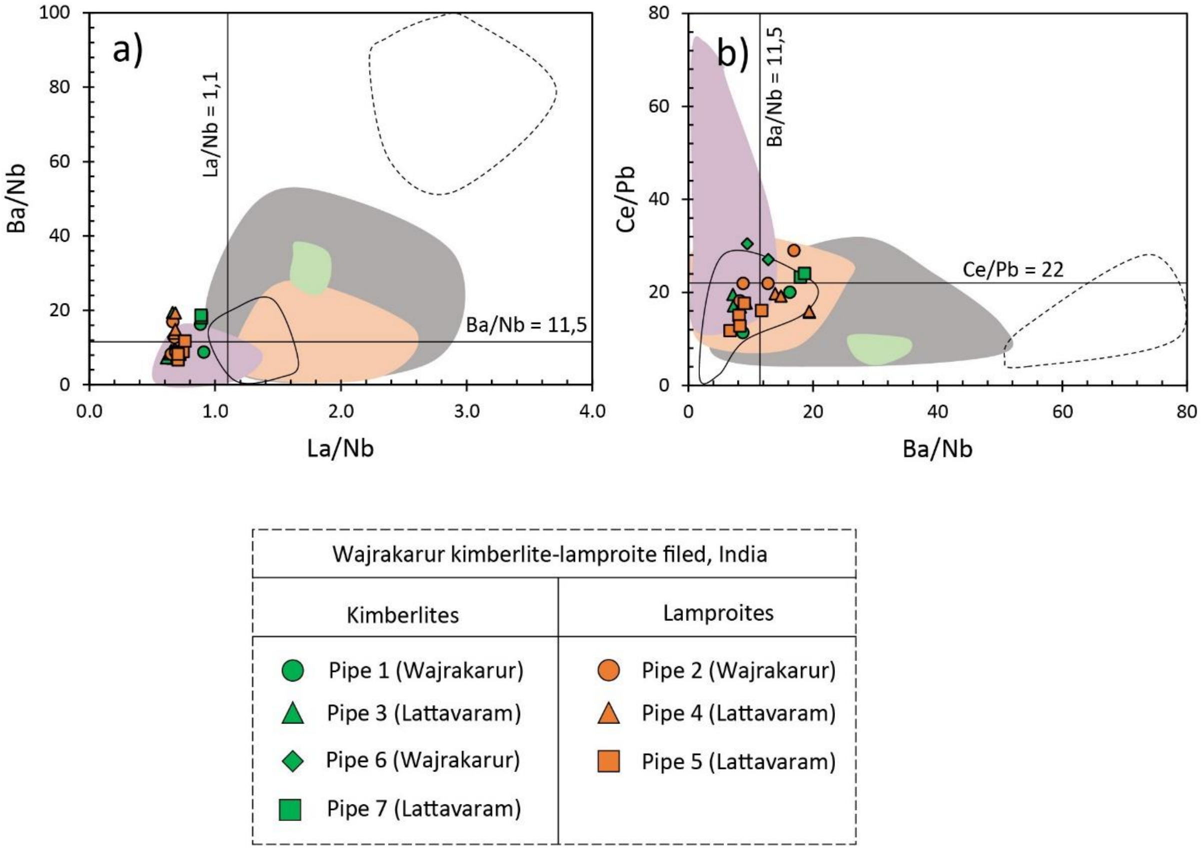

Fig. 31. (a) Ba/Nb vs La/Nb and (b) Ce/Pb vs Ba/Nb for the Wajrakarur kimberlites and lamproites. They show similar ratios with each other and with kimberlites worldwide. The bulk-rock data are from Chalapathi-Rao *et al.* (2004) and the fields are the same as in **Fig. 30**.

5.5 Evaluation of the genetic link between kimberlites and lamproites in the Man Craton

The West African kimberlite/lamproite clusters exhibit variable major element and petrographic features (e.g., the Camp Alpha and Weasua kimberlites are mica-poor and contain low K_2O content, whereas the Weasua lamproite, Tongo and Koidu kimberlites are mica-rich and contain high K_2O). However, the trace element composition of these West African diamondiferous rocks is similar to each other and to that of kimberlite magmas (e.g., similar Ba/Nb, La/Nb and Ce/Pb ratios; Fig. 30; and similar chondrite and primitive mantle normalised patterns; Fig. 29). The processes that can explain the difference in major element and petrographic features but similar trace element patterns for kimberlites and lamproites of the Man Craton are evaluated in this section.

All kimberlites worldwide are believed to originate from a common convective mantle source (e.g., Woodhead *et al.*, 2019; Giuliani *et al.*, 2021). *En route* to the surface, the kimberlite melt assimilates metasomatized SCLM which drastically changes the composition of major elements of the kimberlite rock emplaced on the surface (e.g., Giuliani *et al.*, 2020). Kimberlite melts result from very low degrees of partial melting, thus, these melts are very enriched in incompatible trace elements (e.g., Pearson et al., 2019; Woodhead et al., 2019; Giuliani et al., 2020). Therefore, it is difficult for assimilation to change the composition of trace elements (and their ratios), due to their very high enrichment in the kimberlite melt. Since trace elements are less sensitive to assimilation, they represent the nature of the primary magma source and have been shown to be similar for kimberlites worldwide (e.g., Giuliani *et al.*, 2020; Pearson *et al.*, 2019; Woodhead *et al.*, 2019).

Therefore, the similarity observed in trace element patterns for Camp Alpha, Weasua, Tongo, Koidu kimberlites and Weasua lamproite, suggests that these rocks were derived from a common asthenospheric kimberlitic source. In the absence of melt-SCLM interactions, the West African kimberlites and lamproites would exhibit similar parent melt characteristics (i.e., low mica abundance and K_2O content). However, the major element compositions of these West African rocks were largely controlled by the interaction of their parent magmas with the SCLM during their ascent to the surface (Fig. 32). The Camp Alpha and Weasua kimberlites exhibit close mineralogical and major element similarity to kimberlite magmas, thus, they must have assimilated a less metasomatized SCLM material such as South African kimberlites (e.g., Becker and le Roex, 2006). The Tongo and Koidu kimberlites are mica-rich and contain relatively high K_2O content, thus, they must have assimilated phlogopite-rich SCLM material (maybe an SCLM material similar to the one assimilated by orangeites but with no clinopyroxene component). The Weasua lamproite is mica-rich and contains primary groundmass diopside and calcite. Thus, the Weasua lamproite must have assimilated intensely metasomatized clinopyroxene-mica-rich SCLM material.

The hypothesis that kimberlites and lamproites share a common convective asthenospheric magma source but assimilate differently metasomatized SCLM material *en route* to the surface, is confirmed in the Man Craton, West Africa. Similarly to the Man Craton, the Wajrakarur kimberlites and lamproites (in the Dharwar Craton, southern India) are believed to have originated from a common asthenospheric mantle source (e.g., Shaikh *et al*., 2018; Sarkar *et al*., 2021). The Wajrakarur kimberlites and lamproites are petrographically and mineralogically different (i.e., the groundmass of kimberlites is dominated by phlogopite and monticellite, in comparison to an Al-poor diopside and phlogopite dominated groundmass in lamproites; Sarkar *et al*., 2021; Shaikh *et al*., 2018). However, the Ba/Nb, La/Nb and Ce/Pb trace element ratios of the Wajrakarur kimberlites and lamproites are similar to each other and to those of kimberlites worldwide, as illustrated in Fig. 31. Sarkar *et al*. (2021) suggested a common asthenospheric source for the Wajrakarur lamproites and kimberlites, where the lamproites must have sampled intensely metasomatized SCLM.

However, it is not clear if the above-discussed model applies to all cratonic regions. For example, in the Kaapvaal Craton, the mineralogy and major element chemistry, as well as trace element and Sr-Nd-Hf isotope composition of orangeites are clearly different from those of kimberlites, implying different source regions (e.g., Becker and le Roex, 2006). Therefore, the hypothesis that kimberlites and lamproites share a common convective asthenospheric magma source hypothesis should be evaluated in other cratonic regions worldwide.

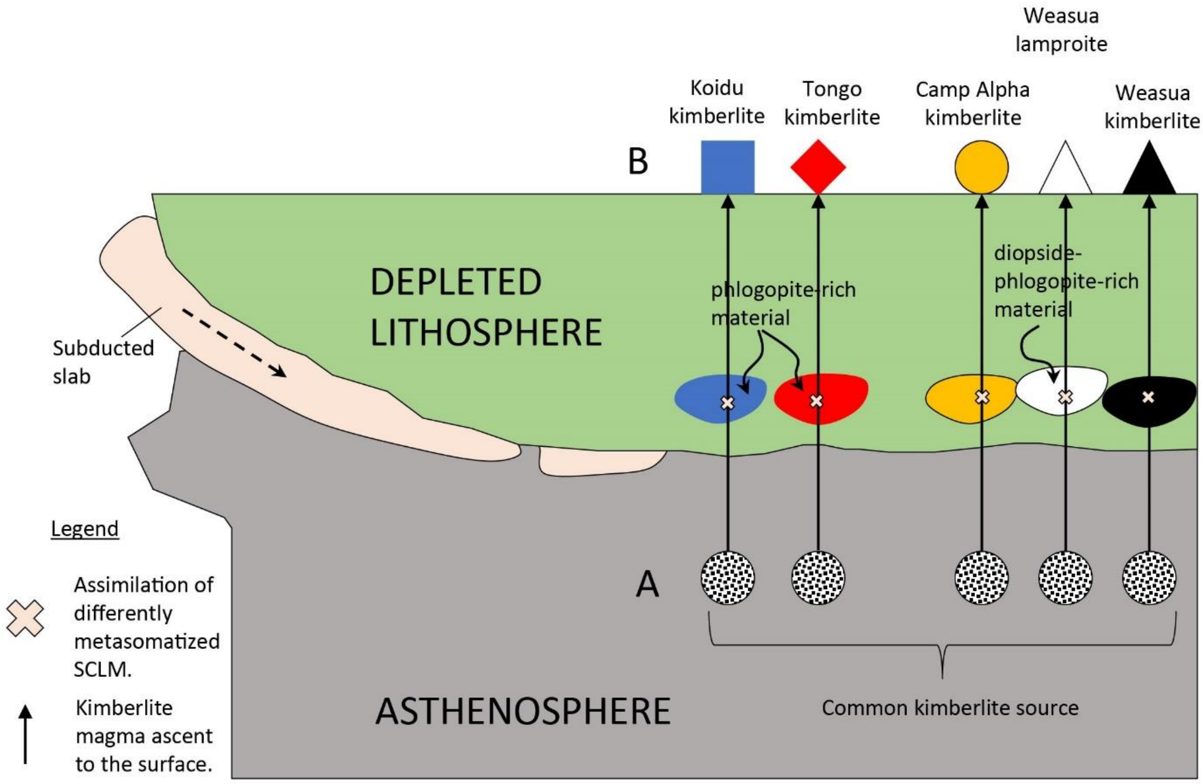

Fig. 32. A model showing the derivation of kimberlites and lamproites in West Africa. The kimberlites and lamproites of the Man Craton share a common asthenospheric kimberlitic source (i.e., A) but assimilated differently metasomatized SCLM material, resulting in mineralogical and petrographic differences (i.e., B).

CHAPTER 6: Conclusions

This study has provided petrography, mineral chemistry (groundmass phlogopite and spinel), bulk-rock geochemistry and classification for the Camp Alpha rocks. In addition to the petrography, the chemistry of perovskite was provided for the Weasua rocks.

The Camp Alpha rocks in this study are mica-poor and contain abundant olivine and ilmenite macrocrysts occurring in a groundmass of phlogopite, spinel, perovskite, serpentine, rare apatite and a base of calcite. Most importantly, there is no evidence of diopside (primary or secondary) in any of the Camp Alpha samples. The Camp Alpha phlogopite is enriched in Al_2O_3 but slightly depleted in FeO and TiO_2 and the spinel exhibits a trend 1 compositional evolution. The trace element ratios Ba/Nb, Ce/Pb and La/Nb fall within the ranges that define kimberlites. Additionally, the chondrite and primitive mantle normalised trace element patterns are similar to kimberlite patterns (e.g., Rb, K, Sr and P show negative anomalies). As a result of these characteristics, the studied Camp Alpha rocks are classified as kimberlites. A close to parent melt composition of the Camp Alpha kimberlite was provided in this study (using bulk-rock geochemistry). The composition of the estimated melt is similar to that of kimberlite magmas and characterised by low K_2O (reflective of mica-poor nature).

The Weasua rocks in this study are phlogopite-rich and contain olivine macrocrysts occurring in a groundmass of phlogopite, spinel, perovskite, primary groundmass diopside, serpentine and calcite. The phlogopite shows enrichment in FeO and depletion in Al_2O_3 and TiO_2. The spinel exhibits a trend 2 compositional evolution. Strongly supported by the presence of primary groundmass diopside and calcite, the studied Weasua rocks are classified as carbonate-rich olivine lamproites. The Weasua rocks described by Skinner *et al.* (2004) are petrographically and geochemically similar to kimberlites. This means that the Weasua region comprises both kimberlites (Skinner *et al*, 2004) and lamproites (Howarth and Giuliani, 2020; this study). An inversion of trace element data for the perovskites was performed using known partition coefficients, to determine the composition of the melt in equilibrium with perovskite at the time of crystallisation. The composition of this Weasua parent melt is similar to that of kimberlite magmas (i.e., similar chondrite/primitive mantle-normalised trace element patterns, Ba/Nb, Ce/Pb and La/Nb ratios).

Whereas the Camp Alpha and Weasua rocks are classified as kimberlite and lamproite, respectively, the trace element composition of the parent melt is similar to that of kimberlite magmas for both cases. This suggests a common asthenospheric magma source for the Camp Alpha kimberlite and Weasua lamproite. *En route* to the surface, these rock types assimilated differently metasomatized SCLM material (i.e., the Weasua lamproite magma assimilated mica-diopside-rich wall rock). The Camp Alpha kimberlite was shown to be approximately 800 Ma old, similar to the Weasua lamproite. Therefore, the Camp Alpha and Weasua magmas were interpreted to be broadly coeval based on the similarity in age and location. In addition to the Indian Dharwar Craton (Sarkar *et al.*, 2021; Shaikh *et al.*, 2018), the hypothesis that kimberlites and lamproites share a common convective asthenospheric magma source but assimilate differently metasomatized SCLM material *en route* to the surface, is confirmed in the Man Craton, West Africa.

References

Armstrong, J.P., Wilson, M., Barnett, R.L., Nowicki, T. and Kjarsgaard, B.A. 2004. Mineralogy of primary carbonate-bearing hypabyssal kimberlite, Lac de Gras, Slave Province, Northwest Territories, Canada. Lithos, 76, 415–433.

Batumike, J.M., Belousova, E., Griffin, W.L., Lubala, T.R.F., Chabu, M., Kaseti, P.K., Djuma, B.A. and Ferrière, L. 2019. Petrography and perovskite U-Pb age of the Katuba kimberlite, Kundelungu Plateau (DR Congo): Implications for regional tectonism and mineralisation. Journal of African Earth Sciences, 156, 35–43.

Beard, A.D., Downes, H., Hegner, E. and Sablukov, S.M. 2000. Geochemistry and mineralogy of kimberlites from the Arkhangelsk Region, NW Russia: evidence for transitional kimberlite magma types. Lithos, 51, 47–73.

Becker, M. and le Roex, A.P. 2006. Geochemistry of South African On- and Off-craton, Group I and Group II Kimberlites: Petrogenesis and Source Region Evolution. Journal of Petrology, 47, 673–703.

Berg, G.W. and Allsopp, H.L. 1972. Low87/Sr86Sr ratios in fresh South African kimberlites. Earth and Planetary Science Letters, 16, 27–30.

Bergman, S.C. 1987. Lamproites and other potassium-rich igneous rocks: a review of their occurrence, mineralogy and geochemistry. Geological Society, London, Special Publications, 30, 103–190.

Beyer, C., Berndt, J., Tappe, S. and Klemme, S. 2013. Trace element partitioning between perovskite and kimberlite to carbonatite melt: New experimental constraints. Chemical Geology, 353, 132–139.

Castillo-Oliver, M., Galí, S., Melgarejo, J.C., Griffin, W.L., Belousova, E., Pearson, N.J., Watangua, M. and O'Reilly, S.Y. 2016. Trace-element geochemistry and U–Pb dating of perovskite in kimberlites of the Lunda Norte province (NE Angola): Petrogenetic and tectonic implications. Chemical Geology, 426, 118–134.

Chakhmouradian, A.R. and Mitchell, R.H. 2000. Occurrence, alteration patterns and compositional variation of perovskite in kimberlites. The Canadian Mineralogist, 38, 975–994.

Chakhmouradian, A.R., Reguir, E.P., Kamenetsky, V.S., Sharygin, V. v and Golovin, A. v 2013. Trace-element partitioning in perovskite: implications for the geochemistry of kimberlites and other mantle-derived undersaturated rocks. Chemical Geology, 353, 112–131.

Chalapathi Rao, N. v, Gibson, S.A., Pyle, D.M. and Dickin, A.P. 2004. Petrogenesis of Proterozoic lamproites and kimberlites from the Cuddapah Basin and Dharwar craton, southern India. Journal of Petrology, 45, 907–948.

Chalapathi-Rao, N. v, Wu, F.Y., Mitchell, R.H., Li, Q.L. and Lehmann, B. 2013. Mesoproterozoic U–Pb ages, trace element and Sr–Nd isotopic composition of perovskite from kimberlites of the Eastern Dharwar craton, southern India: distinct mantle sources and a widespread 1.1 Ga tectonomagmatic event. Chemical Geology, 353, 48–64.

Clement, C.R. 1982. A comparative geological study of some major kimberlite pipes in the Northern Cape and Orange Free State.

Clement, C.R., Skinner, E.M.W. and Scott-Smith, B.H. 1984. Kimberlite Redefined. The Journal of Geology, 92, 223–228.

Coe, N., le Roex, A., Gurney, J., Pearson, D.G. and Nowell, G. 2008. Petrogenesis of the Swartruggens and Star Group II kimberlite dyke swarms, South Africa: constraints from whole rock geochemistry. Contributions to Mineralogy and Petrology, 156, 627–652.

Dawson, J.B. 1987. The kimberlite clan: relationship with olivine and leucite lamproites, and inferences for upper-mantle metasomatism. Geological Society, London, Special Publications, 30, 95–101.

Donnelly, C.L., Griffin, W.L., O'Reilly, S.Y., Pearson, N.J. and Shee, S.R. 2011. The kimberlites and related rocks of the Kuruman kimberlite province, Kaapvaal craton, South Africa. Contributions to Mineralogy and Petrology, 161, 351–371.

Downes, P.J., Wartho, J.-A. and Griffin, B.J. 2006. Magmatic Evolution and Ascent History of the Aries Micaceous Kimberlite, Central Kimberley Basin, Western Australia: Evidence from Zoned Phlogopite Phenocrysts, and UV Laser 40Ar/39Ar Analysis of Phlogopite–Biotite. Journal of Petrology, 47, 1751–1783.

Edwards, D., Rock, N.M.S., Taylor, W.R., Griffin, B.J. and Ramsay, R.R. 1992. Mineralogy and Petrology of the Aries Diamondiferous Kimberlite Pipe, Central Kimberley Block, Western Australia. Journal of Petrology, 33, 1157–1191.

Emmons, S.F. 1877. Descriptive Geology. In King, C. (ed.). Report of the Geological Exploration of the 40th Parallel. U.S. Army Engineer Dept. Prof. Papers 2, 236–238.

Evans, N.J., McInnes, B.I.A., McDonald, B., Danišík, M., Jourdan, F., Mayers, C., Thern, E. and Corbett, D. 2013. Emplacement age and thermal footprint of the diamondiferous Ellendale E9 lamproite pipe, Western Australia. Mineralium Deposita, 48, 413–421.

Fitzgerald, W. 1907. V., 1907: Reports on Portions of the Kimberleys, 1905-6. West. Aust. Govt. Printer.

Fraser, K.J. 1988. Petrogenesis of kimberlites from South Africa and lamproites from Western Australia and North America. Open University (United Kingdom)

Fraser, K.J. and Hawkesworth, C.J. 1992. The petrogenesis of group 2 ultrapotassic kimberlites from Finsch Mine, South Africa. Lithos, 28, 327–345.

Fraser, K.J., Hawkesworth, C.J., Erlank, A.J., Mitchell, R.H. and Scott-Smith, B.H. 1985. Sr, Nd and Pb isotope and minor element geochemistry of lamproites and kimberlites. Earth and Planetary Science Letters, 76, 57–70.

Giuliani, A., Jackson, M.G., Fitzpayne, A. and Dalton, H. 2021. Remnants of early Earth differentiation in the deepest mantle-derived lavas. PNAS, 118.

Giuliani, A., Pearson, D.G., Soltys, A., Dalton, H., Phillips, D., Foley, S.F., Lim, E., Goemann, K., Griffin, W.L. and Mitchell, R.H. 2020. Kimberlite genesis from a common carbonate-rich primary melt modified by lithospheric mantle assimilation. Science Advances, 6, eaaz0424.

Giulinani, A. 2018. Insights into kimberlite petrogenesis and mantle metasomatism from a review of the compositional zoning of olivine in kimberlites worldwide. Lithos, 312, 322 – 342.

Giuliani, A., Soltys, A., Phillips, D., Kamenetsky, V.S., Maas, R. and Goemann, K. 2017. The final stages of kimberlite petrogenesis: petrography, mineral chemistry, melt inclusions and Sr-CO isotope geochemistry of the Bultfontein kimberlite (Kimberley, South Africa). Chemical Geology, 455, 342-356.

Giuliani, A., Phillips, D., Kamenetsky, V.S., Goemann, K. 2016. Constraints on kimberlite ascent mechanisms revealed by phlogopite compositions in kimberlites and mantle xenoliths. Lithos, 240 – 243, 189-201.

Giuliani, A., Phillips, D., Woodhead, J.D., Kamenetsky, V.S., Fiorentini, M.L., Maas, R., Soltys, A. and Armstrong, R.A. 2015. Did diamond-bearing orangeites originate from MARID-veined peridotites in the lithospheric mantle? Nature communications, 6, 1–10.

Griffin, W., Batumike, J., Greau, Y., Pearson, N., Shee, S. and O'Reilly, S.Y. 2014. Emplacement ages and sources of kimberlites and related rocks in southern Africa: U–Pb ages and Sr–Nd isotopes of groundmass perovskite. Contributions to Mineralogy and Petrology, 168, 1-13.

Haggerty, S.E. 2017. Kimberlite discoveries in NW Liberia: Tropical exploration & preliminary results. Journal of Geochemical Exploration, 173, 99–109.

Harris, M., le Roex, A. and Class, C. 2004. Geochemistry of the Uintjiesberg kimberlite, South Africa: petrogenesis of an off-craton, group I, kimberlite. Lithos, 74, 149–165.

Howarth, G.H. and Giuliani, A. 2020. Contrasting types of micaceous kimberlite-lamproite magmatism from the Man Craton (West Africa): New insights from petrography and mineral chemistry. Lithos, 362–363.

Howarth, G.H., Michael, E., Skinner, W. and Prevec, S.A. 2011. Petrology of the hypabyssal kimberlite of the Kroonstad group II kimberlite (orangeite) cluster, South Africa: Evolution of the magma within the cluster. Lithos, 125, 795–808.

Howarth, G.H., Moore, A.E., Harris, C., van der Meer, Q.H.A. and le Roux, P. 2019. Crustal versus mantle origin of carbonate xenoliths from Kimberley region kimberlites using CO-Sr-Nd-Pb isotopes and trace element abundances. Geochimica et Cosmochimica Acta, 266, 258–273.

Hwang, P., Taylor, W.R., Rocky, N.M.S. and Ramsay, R.R. 1994. Mineralogy, geochemistry and petrogenesis of the Metters Bore No. 1 lamproite pipe, Calwynyardah Field, West Kimberley Province, Western Australia. Mineralogy and Petrology, 51, 195–226.

Jaques, A.L. 2016. Major and trace element variations in oxide and titanate minerals in the West Kimberley lamproites, Western Australia. Mineralogy and Petrology, 110, 159–197.

Maas, R., Kamenetsky, M.B., Sobolev, A. v, Kamenetsky, V.S. and Sobolev, N. v 2005. Sr, Nd, and Pb isotope evidence for a mantle origin of alkali chlorides and carbonates in the Udachnaya kimberlite, Siberia. Geology, 33, 549–552.

Mathafeng, K.P. 2021. Classification and petrogenesis of the Tongo dike-01 from the Tongo-Tongoma cluster, Sierra Leone: constraints from bulk-rock geochemistry. MSc thesis, University of Cape Town.

Mirnejad, H. and Bell, K. 2006. Origin and Source Evolution of the Leucite Hills Lamproites: Evidence from Sr-Nd-Pb-O Isotopic Compositions. Journal of Petrology, 47, 2463–2489.

Mitchell, R.H. 1970. Kimberlite and related rocks: a critical reappraisal. The Journal of Geology, 78, 686–704.

Mitchell, R.H. 1986. Kimberlites: mineralogy, geochemistry, and petrology. Springer Science & Business Media

Mitchell, R.H. 1995. Kimberlites and orangeites. In: Kimberlites, Orangeites, and Related Rocks. Springer, 1–90.

Mitchell, R.H. 2005. Potassic magmas derived from metasomatized lithospheric mantle: nomenclature and relevance to exploration for diamond-bearing rocks. Paper presented at the Group Discussion on Kimberlites and Related Rocks of India organised by the Geological Society of India in.

Mitchell, R.H. and Bergman, S.C. 1991. Petrology of lamproites. Springer Science & Business Media

Mitchell, R.H., Giuliani, A. and O'Brien, H. 2019. What is a kimberlite? Petrology and mineralogy of hypabyssal kimberlites. Elements: An International Magazine of Mineralogy, Geochemistry, and Petrology, 15, 381–386.

Mitchell, R.H. and Meyer, H.O.A. 1986. Mineralogy of micaceous kimberlites from the new Elands and Star mines, Orange Free State, South Africa. In: International Kimberlite Conference: Extended Abstracts. 75–77.

Pandey, A., and Chalapathi-Rao, N.C. 2020. Supercontinent transition as a trigger for~ 1.1 Gyr diamondiferous kimberlites and related magmatism in India. Lithos, 370, 105-620.

Pearson, D.G., Woodhead, J. and Janney, P.E. 2019. Kimberlites as Geochemical Probes of Earth's Mantle. Elements, 15, 387–392.

Roeder, P.L. and Schulze, D.J. 2008. Crystallization of Groundmass Spinel in Kimberlite. Journal of Petrology, 49, 1473–1495.

Russell, J.K., Porritt, L.A., Lavallée, Y., and Dingwell, D.B. 2012. Kimberlite ascent by assimilation-fuelled buoyancy. Nature, 481, 352-356.

le Roex, A.P., Bell, D.R. and Davis, P. 2003. Petrogenesis of Group I Kimberlites from Kimberley, South Africa: Evidence from Bulk-rock Geochemistry. Journal of Petrology, 44, 2261–2286.

Sarkar, S., Giuliani, A., Ghosh, S. and Phillips, D. 2021. Petrogenesis of coeval lamproites and kimberlites from the Wajrakarur field, Southern India: New insights from olivine compositions. Lithos, 106524.

Shaikh, A.M., Kumar, S.P., Patel, S.C., Thakur, S.S., Ravi, S. and Behera, D. 2018. The P3 kimberlite and P4 lamproite, Wajrakarur kimberlite field, India: mineralogy, and major and minor element compositions of olivines as records of their phenocrystic vs xenocrystic origin. Mineralogy and Petrology, 112, 609–624.

Skinner, E.M.W. 1989. Contrasting group I and II kimberlite petrology: Towards a genetic model for kimberlites. In Ross et al. (1989) q.v. 1, 528–544.

Skinner, E.M.W., Apter, D.B., Morelli, C. and Smithson, N.K. 2004. Kimberlites of the Man craton, West Africa. Lithos, 76, 233–259.

Skinner, E.M.W. and Clement, C.R. 1979. Mineralogical classification of southern African kimberlites. In Boyd and Meyer (1979) q.v. 1, 129–139.

Skinner, E.M.W., Viljoen, K.S., Clark, T.C. and Smith, C.B. 1994. The petrography, tectonic setting and emplacement ages ofkimberlites in the south western border region of the Kaapvaal craton, Prieska area. In Meyer and Leonardos (1994) q.v. 1, 80–97.

Smith, C., Allsop, H., Kramers, J., Hutchinson, G. and Roddick, J. 1985. Emplacement ages of Jurassic-Cretaceous South African kimberlites by the Rb-Sr method on phlogopite and whole-rock samples. Transactions of the Geological Society of South Africa, 88, 249-266.

Smith, C.B. 1983. Pb, Sr and Nd isotope evidence for sources of African cretaceous kimberlites. Nature, 304, 51–54.

Smith, C.B. and Skinner, E.M. 1984. Diamondiferous Lamproites. The Journal of Geology, 92, 433–438.

Stamm, N., Schmidt, M.W. 2017. Asthenospheric kimberlites: volatile contents and bulk compositions at 7 GPa. Earth and Planetary Science Letters, 474, 309-321.

Sun, S.-S. and McDonough, W.F. 1989. Chemical and isotopic systematics of oceanic basalts: implications for mantle composition and processes. Geological Society, London, Special Publications, 42, 313–345.

Tainton, K.M. and Browning, P. 1991. The Group-2-Kimberlite-Lamproite Connection: Some Constraints from the Barkly-West District, Northern Cape Province, South Africa. In: International Kimberlite Conference: Extended Abstracts. 405–407.

Tainton, K.M. and McKenzie, D.A.N. 1994. The generation of kimberlites, lamproites, and their source rocks. Journal of Petrology, 35, 787–817.

Talukdar, D., Pandey, A., Chalapathi Rao, N. v, Kumar, A., Pandit, D., Belyatsky, B. and Lehmann, B. 2018. Petrology and geochemistry of the Mesoproterozoic Vattikod lamproites, Eastern Dharwar Craton, southern India: evidence for multiple enrichment of sub-continental lithospheric mantle and links with amalgamation and break-up of the Columbia supercontinent. Contributions to Mineralogy and Petrology, 173.

Taylor, W.R. 1998. Mineralogy of the Jagersfontein kimberlite-an unusual group 1 micaceous kimberlite-and a comment on the robustness of the mineralogical definition of'orangeite'. In: International Kimberlite Conference: Extended Abstracts. 892–894.

Taylor, W.R., Tompkins, L.A. and Haggerty, S.E. 1994. Comparative geochemistry of West African kimberlites: Evidence for a micaceous kimberlite endmember of sublithospheric origin. Geochimica et Cosmochimica Acta, 58, 4017–4037.

Wade, A. and Prider, R.T. 1940. The leucite-bearing rocks of the West Kimberley area, Western Australia. Quarterly Journal of the Geological Society, 96, 39-NP.

Wagner, P.A. 1914. The diamond fields of southern Africa. Transvaal leader

Wagner, P.A. 1928. The Evidence of the Kimberlite Pipes on the Constitution of the Outer Part of the Earth. S. Af. Journ. Sci., 25, 127.

Woodhead, J., Hergt, J., Giuliani, A., Maas, R., Phillips, D., Pearson, D.G. and Nowell, G. 2019. Kimberlites reveal 2.5-billion-year evolution of a deep, isolated mantle reservoir. Nature, 573, 578–581.

Wu, F.-Y., Mitchell, R.H., Li, Q.-L., Sun, J., Liu, C.-Z. and Yang, Y.-H. 2013. In situ UPb age determination and SrNd isotopic analysis of perovskite from the Premier (Cullinan) kimberlite, South Africa. Chemical Geology, 353, 83–95.

Xiang, L., Zheng, J., Zhai, M. and Siebel, W. 2020. Geochemical and Sr–Nd–Pb isotopic constraints on the origin and petrogenesis of Paleozoic lamproites in the southern Yangtze Block, South China. Contributions to Mineralogy and Petrology, 175.

Appendices

Appendix 1A: Major element composition of phlogopites from Camp Alpha

Units are in wt.%		F	Na_2O	MgO	Al_2O_3	SiO_2	K_2O	FeO_T	MnO	TiO_2	BaO	Cl	CaO	Cr_2O_3	Total
Analysis	zone														
Sample SC11 A1															
1	zone 2	0.27	0.12	25.3	15.07	35.31	7.67	6.18	0.02	0.81	0.85	0.14	0.02	0.07	91.83
2	zone 2	0.29	0.13	25.78	15.25	35.21	7.1	5.55	0.08	0.58	1.21	0.11	0.02	0.02	91.34
3	zone 2	0.37	0.11	25.68	15.61	35.87	7.17	6.3	0.03	0.88	0.82	0.1	0.03	0.06	93.03
4	zone 2	0.31	0.12	24.44	16.68	36.69	8.16	6.09	0.07	0.84	0.86	0.04	0.01	0.08	94.38
5	zone 2	0.36	0.09	24.42	17.24	35.99	8.09	5.21	0.06	0.83	1.38	0.07	0.02	0.07	93.81
6	zone 1	0.27	0.15	25.32	15.52	35.64	7.43	5.14	0.03	0.8	0.84	0.11	0.02	0.02	91.29
7	zone 1	0.26	0.16	24.52	16.26	34.81	7.66	6.08	0.04	0.96	1.1	0.11	0.06	0.04	92.05
8	zone 1	0.22	0.16	25.81	15.54	34.55	6.78	6.74	0.05	0.77	0.64	0.13	b.d.	0.03	91.41
9	zone 1	0.15	0.23	26.04	16.7	36.37	8.24	3.46	0.05	0.11	0.08	0.09	0.05	0.05	91.62
10	zone 1	0.46	0.15	23.73	16.74	36.37	8.95	3.53	0.08	0.46	2.33	0.06	0.1	0.07	93.04
11	zone 1	0.17	0.21	27.35	15.28	35.52	6.89	4.67	0.03	0.06	0.03	0.1	0.08	0.01	90.38
12	zone 1	0.15	0.13	27.11	14.97	35.94	6.95	4.64	0.07	0.04	0.39	0.07	0.02	0.04	90.52
13	zone 1	0.37	0.13	23.46	16.88	37.51	9.86	4.52	0.12	0.79	0.78	0.06	0.04	0.05	94.56
14	zone 1	0.35	0.19	25.31	16.52	34.41	6.98	5.6	0.1	0.81	1.92	0.15	0.14	0.03	92.51
15	zone 1	0.14	0.16	27.45	15.35	34.79	5.57	4.85	0.11	0.09	0.13	0.11	0.1	0.04	88.89
16	zone 1	0.36	0.19	23.44	17.51	36.04	9.1	3.98	0.01	0.88	2.76	0.03	0.12	0.03	94.46
17	zone 1	0.28	0.19	25.13	15.2	36.22	7.74	5.67	0.11	0.79	0.76	0.09	0.01	0.03	92.21

Appendix 1A: *Continues*

Units are in wt.%		F	Na_2O	MgO	Al_2O_3	SiO_2	K_2O	FeO_T	MnO	TiO_2	BaO	Cl	CaO	Cr_2O_3	Total
Analysis	zone														
Sample SC11 B1															
18	zone 1	0.19	0.06	27.94	11.74	38.81	7.38	4.56	0.02	0.64	0.96	0.05	0.08	0.04	92.48
19	zone 1	0.32	0.07	26.01	15.07	38.67	9.35	2.9	0.05	0.34	2.45	0.05	0.07	0.05	95.4
20	zone 1	0.44	0.09	26.16	14.07	39.74	9.05	2.37	b.d.	0.25	1.4	0.01	0.16	0.03	93.76
21	zone 1	0.4	0.07	26.07	14.21	39.36	9.77	2.41	b.d.	0.2	0.04	0.04	0.09	0.04	92.7
22	zone 1	0.44	0.08	26.91	12.91	39.08	8.85	3.76	0.02	0.1	0.38	0.03	0.13	0.01	92.7
23	zone 1	0.34	0.06	27.37	12.77	39.07	7.83	4.33	0.04	0.22	0.29	0.07	0.06	0.01	92.45
24	zone 1	0.41	0.09	27.64	14.01	38.9	7.91	3.91	0.02	0.18	1.42	0.06	0.07	0.07	94.69
25	zone 1	0.37	0.09	25.34	15.09	37.22	9.14	3.01	0.01	0.21	3.17	0.05	0.06	0.07	93.83
26	zone 1	0.34	0.07	26.41	14.15	39.73	9.78	2.78	0.03	0.22	0.4	0.05	0.05	0.04	94.05
Sample SC11 B2															
27	zone 1	0.14	0.05	28.91	10.44	40.72	7.59	4.4	0.02	0.1	0.06	0.02	0.04	b.d.	92.5
28	zone 1	0.06	0.06	28.91	10.09	41.54	8.39	4.34	0.07	0.02	0.06	0.03	0.07	b.d.	93.64
29	zone 1	0.04	0.06	30.3	8.03	41.56	7	6	0.05	0.12	0.07	0.02	0.05	b.d.	93.31
30	zone 1	0.08	0.05	34.33	2.84	41.2	1.47	6.36	0.12	0.1	b.d.	0.05	0.07	0.01	86.69
31	zone 1	0.09	0.06	28.56	10.64	42.09	8.54	3.94	0.02	0.04	0.06	0.02	0.04	0.04	94.16
32	zone 1	0.2	0.11	29.24	13.89	32.58	2.94	7.21	0.09	0.24	1.8	0.1	0.12	b.d.	88.51
33	zone 1	0.1	0.04	28.94	5.26	36.65	2.65	3.83	0.07	0.12	0.09	0.04	6.4	b.d.	84.19
34	zone 1	0.23	0.09	33.99	6.54	40.35	2.06	5.92	0.13	0.18	0.35	0.05	0.25	b.d.	90.14
35	zone 1	0.14	0.04	31.41	8.95	35.74	2.5	9.26	0.03	0.05	0.05	0.03	0.06	0.04	88.31
36	zone 1	0.21	0.11	27.75	15.58	34.14	5.53	5.91	0.02	0.26	2.34	0.05	0.2	0.05	92.15

Appendix 1A: *Continues*

Units are in wt.%		F	Na_2O	MgO	Al_2O_3	SiO_2	K_2O	FeO_T	MnO	TiO_2	BaO	Cl	CaO	Cr_2O_3	Total
Analysis	zone														
						Sample SC11 B2									
37	zone 2	0.46	0.08	25.32	14.46	37.91	8.69	4.06	0.02	0.32	2.33	0.02	0.08	0.02	93.77
38	zone 2	0.07	0.01	30.91	1.06	33.27	1.13	18.65	0.36	0.08	b.d.	0.05	0.12	0.04	85.74
39	zone 2	0.45	0.04	27.18	13.65	38.4	7.73	4.33	0.04	0.19	1.82	0.05	0.02	0.06	93.96
40	zone 2	0.09	0.04	28.72	0.93	37.14	5.43	16.58	0.09	0.06	0.05	0.03	0.04	b.d.	89.19
41	zone 2	0.13	0.04	28.54	1.3	38.53	6.27	15.59	0.05	0.11	0.03	0.02	0.06	0.04	90.73
42	zone 2	0.43	0.08	24.01	18.9	33.32	7.12	2.91	b.d.	0.31	6.38	0.04	0.12	0.02	93.66
43	zone 2	0.4	0.08	27.1	10.97	38.33	7.02	6.48	0.06	0.18	0.84	0.04	0.16	0.01	91.67
44	zone 2	0.41	0.05	24.7	18.97	34.13	6.36	2.89	0.03	0.28	6.22	0.05	0.27	0.01	94.37
45	zone 2	0.55	0.05	25.94	14.44	39.18	9.1	2.5	0.04	0.34	4.25	0.01	0.13	0.05	96.57
						Sample SC11 B3b									
46	zone 1	0.56	0.08	27.49	13.19	40.34	8.91	2.82	0.01	0.1	1.85	0.02	0.04	0.03	95.44
47	zone 1	0.51	0.06	27.25	12.96	39.77	8.53	3.9	0.02	0.22	0.95	0.03	0.12	0.09	94.41
48	zone 1	0.47	0.05	26.14	15.57	39.85	9.77	2.41	b.d.	0.09	0.46	0.02	0.03	b.d.	94.87
49	zone 2	0.46	0.06	25.53	15.61	38.15	8.32	2.95	0.01	0.21	2.41	0.02	0.13	0.05	93.93
50	zone 1	0.68	0.07	26.11	14.82	38.01	8.45	3.38	0.12	0.14	2.61	0.02	0.05	0.02	94.47
51	zone 2	0.42	0.04	26.64	15.18	40.15	8.46	3.34	b.d.	0.46	3.09	0.02	0.01	0.11	97.93
52	zone 1	0.5	0.04	26.71	14.68	38.97	8.39	3.48	0.07	0.25	2.01	0.03	0.07	b.d.	95.19
53	zone 2	0.35	0.05	23.61	14.91	39.29	9.56	4.7	0.06	1.47	1.9	0.02	0.01	0.12	96.07
54	zone 1	0.63	0.06	26.2	13.7	39.37	9.54	3.27	0.05	0.29	1.59	0.01	0.04	0.02	94.78
55	zone 1	0.51	0.04	26.25	15.48	40.16	10.28	2.82	0.04	0.27	0.18	b.d.	0.05	b.d.	96.07

Appendix 1A: *Continues*

Units are in wt.%		F	Na_2O	MgO	Al_2O_3	SiO_2	K_2O	FeO_T	MnO	TiO_2	BaO	Cl	CaO	Cr_2O_3	Total
Analysis	zone														
							Sample SC11 B3b								
56	zone 2	0.47	0.05	23.67	19.43	33.76	7.22	2.24	b.d.	0.27	8.51	0.01	0.02	0.04	95.68
57	zone 1	0.42	0.03	24.85	13.25	39.11	8.58	3.34	0.01	0.18	1.05	0.02	0.11	b.d.	90.94
58	zone 2	0.58	0.06	25.73	14.44	38.21	7.78	3.99	0.04	0.18	2.89	0.02	0.11	0.04	94.07
59	zone 2	0.34	0.03	24.46	14.98	38.31	8.97	2.68	0.04	0.29	3.3	0.01	0.14	0.08	93.66

Appendix 1B: Major element composition of spinels from Camp Alpha

Units are in wt.%		Na_2O	MgO	K_2O	CaO	FeO_T	MnO	Cr_2O_3	TiO_2	SiO_2	Al_2O_3	NiO	Total
Analysis	zone												
						Sample SC11 A1							
1	zone 2	0.07	11.36	0.01	0.07	74.95	1.05	1.17	1.13	0.17	0.63	0.45	91.07
2	zone 2	0.05	12.63	0.02	0.17	73.34	1.04	0.73	2.37	0.04	1.37	0.4	92.16
3	zone 2	0.05	15.08	0.02	0.06	67.65	0.85	0.48	4.86	0.04	2.93	0.35	92.36
4	zone 2	0.11	8.64	0.04	0.01	79.45	1.08	0.87	0.3	0.06	0.09	0.51	91.15
5	zone 2	0.04	14.67	0.01	0.04	67.51	0.82	1.45	4.71	0.05	2.95	0.39	92.62
6	zone 2	0.05	10.28	0.02	0.15	76.57	1.31	1.15	1.08	0.05	0.4	0.51	91.58
7	zone 2	0.05	10.56	0.02	0.04	75.35	0.8	0.64	3.36	0.13	2.02	0.22	93.17

Appendix 1B: *Continues*

Units are in wt.%		Na_2O	MgO	K_2O	CaO	FeO_T	MnO	Cr_2O_3	TiO_2	SiO_2	Al_2O_3	NiO	Total
Analysis	zone												
Sample SC11 A1													
8	zone 2	0.04	2.53	0.02	0.03	83.89	0.15	0.22	0.43	0.52	0.96	0.08	88.87
9	zone 2	0.03	14.81	0.02	0.04	67.67	0.9	0.67	4.77	0.04	2.72	0.32	92
10	zone 2	0.06	9.26	0.02	0.04	79.27	1.19	0.95	0.4	0.05	0.11	0.53	91.88
Sample SC11 B1													
11	zone 2	0.04	11.46	0.02	0.07	74.69	0.95	1.07	2.19	0.08	1.27	0.25	92.08
12	zone 2	0.06	12.56	0.05	0.09	72.21	0.9	1.2	2.82	0.22	0.63	0.49	91.21
13	zone 2	0.07	13.04	0.01	0.3	69.22	0.79	0.28	5.08	0.06	3.45	0.39	92.7
14	zone 2	0.05	11.04	0.04	0.19	75.66	0.65	0.88	2.22	0.05	0.64	0.55	91.97
15	zone 2	0.06	10.88	0.04	0.14	75.98	0.97	0.98	1.9	0.08	0.7	0.28	92.02
16	zone 2	0.05	13.64	0.03	0.06	65.55	1.02	1.4	6.1	0.06	3.3	0.3	91.53
17	zone 2	0.05	11.24	0.02	0.13	76.83	0.69	0.78	1.21	0.04	0.41	0.48	91.9
18	zone 2	0.03	13.55	0.05	0.16	69.55	0.88	0.94	4.57	0.05	1.9	0.5	92.18
19	zone 2	0.04	8.14	0.03	2.59	71.32	0.69	0.47	3.54	1.69	0.15	0.18	88.83
20	zone 2	0.03	11.69	0.03	0.12	72.99	1.04	1.54	3.26	0.05	1.15	0.28	92.19
Sample SC11 B2													
21	zone 1	0.03	19.65	0.02	0.06	39.56	1.2	12.06	12.08	0.12	10.4	0.28	95.47
22	zone 2	0.02	11.56	0.01	0.03	73.99	1.11	2.04	2.35	0.09	0.41	0.43	92.05
23	zone 2	0.04	10.81	0.03	0.07	78.22	0.86	0.83	0.97	0.06	0.28	0.52	92.66
24	zone 2	0.01	10.94	0.02	0.06	76.12	0.88	0.73	1.85	0.07	0.59	0.49	91.77

Appendix 1B: *Continues*

Units are in wt.%		Na_2O	MgO	K_2O	CaO	FeO_T	MnO	Cr_2O_3	TiO_2	SiO_2	Al_2O_3	NiO	Total
Analysis	zone												
Sample SC11 B2													
25	zone 2	0.09	8.45	0.04	0.06	79.76	0.9	1.16	0.63	0.08	0.36	0.56	92.1
26	zone 2	0.02	10.29	0.03	0.4	77.6	0.89	1.05	1.24	0.09	0.15	0.47	92.22
27	zone 2	0.02	10.43	0.03	0.16	77.08	0.88	0.92	1.28	0.08	0.41	0.52	91.81
28	zone 2	0.03	9.34	0.01	4.08	72.46	0.91	0.96	4.51	0.08	0.14	0.5	93
29	zone 2	0.03	10.42	0.02	0.2	77.17	0.89	1.48	1.09	0.06	0.41	0.49	92.26
30	zone 2	0.02	8.22	0.02	0.06	80.09	0.87	0.9	0.46	0.25	0.09	0.5	91.5
31	zone 2	0.05	12.28	0.05	0.08	73.71	1.06	1.47	2.39	0.11	0.59	0.43	92.22
32	zone 1	0.02	16.2	0.04	0.14	45.27	0.84	11.51	5.91	0.25	13.63	0.33	94.15
33	zone 1	0.03	13.29	0.02	0.14	71.26	0.78	0.83	4	0.09	1.59	0.45	92.49
Sample C11 B3b													
34	zone 2	0.05	8.57	0.01	0.03	77.9	0.45	0.22	2.85	0.1	2.14	0.5	92.83
35	zone 2	0.31	5.8	0.04	15.61	42.95	0.54	0.61	23.3	0.21	0.3	0.19	89.86
36	zone 2	0.05	8.58	0.06	0.13	76.24	0.77	0.8	2.42	0.51	1.27	0.42	91.27
37	zone 2	0.04	12.32	0.02	0.25	64.12	0.95	2.66	7.7	0.16	5.82	0.38	94.42
38	zone 2	0.03	10.79	0.01	0.13	74.54	0.98	0.9	2.98	0.06	1.54	0.34	92.3
39	zone 2	0.03	10.25	0.01	0.09	79.05	0.77	0.56	1.01	0.04	0.21	0.42	92.43
40	zone 2	0.02	9.61	0.01	0.02	75.83	0.78	0.29	2.77	0.08	2.7	0.4	92.5
41	zone 2	0.03	10.38	0.02	0.04	72.5	0.83	0.16	4.06	0.08	3.26	0.41	91.77
42	zone 1	0.05	8.81	0.03	1.4	74.36	0.73	1.1	3.27	0.13	1.51	0.42	91.79
43	zone 2	0.04	10.83	0.02	0.07	72.37	0.76	1.02	4.68	0.03	2.89	0.4	93.1

Appendix 1B: *Continues*

Units are in wt.%		Na_2O	MgO	K_2O	CaO	FeO_T	MnO	Cr_2O_3	TiO_2	SiO_2	Al_2O_3	NiO	Total
Analysis	zone												
						Sample C11 B3b							
44	zone 1	0.02	16.31	0.05	0.15	44.87	0.78	11.8	6.03	0.17	13.94	0.31	94.43
45	zone 1	0.02	11.85	0.01	0.05	70.05	0.95	0.59	5.43	0.07	3.49	0.42	92.95

Appendix 2A: Major element composition of perovskites from Weasua

Units are in wt.%		SiO_2	Ce_2O_3	TiO_2	La_2O_3	CaO	Al_2O_3	K_2O	MgO	NiO	Na_2O	FeO	MnO	Cr_2O_3	SrO	Total
Analysis	core /rim															
								Sample Y5747								
prv1	core	b.d.	0.45	55.01	0.55	39.10	0.44	0.01	0.08	b.d.	0.31	1.44	b.d.	b.d.	0.18	97.56
prv1	core	b.d.	0.75	55.15	0.65	38.64	0.37	0.01	0.06	b.d.	0.32	1.35	0.04	0.02	0.27	97.62
prv1	core	b.d.	0.50	55.55	0.76	38.72	0.39	0.01	0.07	b.d.	0.36	1.64	0.05	b.d.	0.20	98.25
prv1	rim	b.d.	0.77	55.78	0.77	38.62	0.35	0.01	0.07	0.08	0.39	1.42	0.02	b.d.	0.20	98.47
prv1	rim	b.d.	0.52	55.99	0.70	39.04	0.37	0.01	0.03	b.d.	0.34	1.48	b.d.	b.d.	0.29	98.77
prv1	rim	b.d.	0.72	56.32	0.38	38.81	0.39	0.01	0.03	0.03	0.38	1.46	b.d.	b.d.	0.23	98.74
prv1	rim	b.d.	0.41	56.21	0.50	38.76	0.36	0.03	0.07	b.d.	0.30	1.46	b.d.	0.01	0.26	98.35

Appendix 2A: *Continues*

Units are in wt.%		SiO_2	Ce_2O_3	TiO_2	La_2O_3	CaO	Al_2O_3	K_2O	MgO	NiO	Na_2O	FeO	MnO	Cr_2O_3	SrO	Total
Analysis	core/rim															
Sample Y5747																
prv1	rim	b.d.	b.d.	56.59	0.34	39.55	0.13	0.02	0.03	b.d.	0.44	1.28	0.04	b.d.	0.27	98.68
prv1	rim	b.d.	0.63	55.92	0.69	36.86	0.01	0.05	b.d.	0.07	1.05	0.91	b.d.	b.d.	0.57	96.75
prv2	core	b.d.	0.59	54.80	0.70	38.29	0.32	0.02	0.03	0.05	0.34	1.53	0.02	0.03	0.17	96.89
prv2	core	b.d.	0.59	55.63	0.32	38.84	0.35	0.01	0.01	0.03	0.29	1.51	0.04	b.d.	0.14	97.77
prv2	core	b.d.	0.57	56.24	0.40	38.61	0.40	0.03	0.04	b.d.	0.37	1.50	b.d.	b.d.	0.19	98.35
prv2	rim	b.d.	0.38	56.21	0.31	39.07	0.38	0.02	0.03	b.d.	0.33	1.68	b.d.	b.d.	0.24	98.63
prv2	rim	b.d.	0.43	55.70	0.61	38.15	0.10	0.03	0.02	0.03	0.54	1.05	b.d.	0.30	0.29	97.24
prv2	rim	b.d.	b.d.	56.11	0.27	39.62	0.16	0.02	0.06	b.d.	0.40	1.29	0.05	b.d.	0.26	98.23
prv2	rim	b.d.	0.46	56.03	0.61	37.98	0.03	0.02	b.d.	b.d.	0.89	0.85	0.04	b.d.	0.32	97.23
prv2	rim	b.d.	0.50	56.18	0.71	37.51	0.03	0.02	b.d.	0.01	0.99	0.78	0.01	b.d.	0.38	97.10
prv4	core	b.d.	0.42	56.01	0.54	38.46	0.36	0.03	0.04	b.d.	0.30	1.72	b.d.	b.d.	0.23	98.12
prv4	core	b.d.	0.56	56.02	0.40	38.51	0.35	0.01	0.03	0.01	0.40	1.48	b.d.	b.d.	0.23	97.99
prv4	rim	b.d.	0.45	56.16	0.42	38.73	0.40	0.02	0.05	0.02	0.26	1.58	0.01	b.d.	0.23	98.33
prv7	core	b.d.	0.77	55.43	0.57	38.90	0.38	0.01	0.06	0.01	0.31	1.64	b.d.	b.d.	0.14	98.20
prv7	core	b.d.	0.36	55.89	0.41	38.74	0.37	0.01	0.04	b.d.	0.35	1.52	b.d.	0.01	0.19	97.89
prv7	rim	b.d.	0.39	55.70	0.36	38.88	0.40	0.01	0.03	b.d.	0.36	1.51	0.04	b.d.	0.22	97.92
prv7	rim	b.d.	0.43	56.07	0.38	38.76	0.36	0.01	0.04	b.d.	0.39	1.48	0.05	b.d.	0.21	98.20

Appendix 2A: *Continues*

Units are in wt.%		SiO_2	Ce_2O_3	TiO_2	La_2O_3	CaO	Al_2O_3	K_2O	MgO	NiO	Na_2O	FeO	MnO	Cr_2O_3	SrO	Total
Analysis	core /rim															
								Sample Y5747								
prv8	core	b.d.	0.49	55.93	0.49	39.27	0.41	0.01	0.01	0.05	0.28	1.38	b.d.	b.d.	0.22	98.54
prv8	rim	b.d.	0.72	56.19	0.52	38.67	0.35	0.02	0.05	0.03	0.40	1.40	0.03	b.d.	0.19	98.55
prv9	core	b.d.	0.53	55.84	0.57	38.73	0.35	0.03	0.04	0.05	0.34	1.54	0.02	b.d.	0.20	98.25
prv9	rim	b.d.	0.31	56.32	0.49	38.83	0.38	0.01	0.05	0.01	0.37	1.56	b.d.	b.d.	0.20	98.53
prv12	core	b.d.	0.17	56.73	0.40	39.42	0.13	b.d.	0.03	b.d.	0.34	1.16	0.04	b.d.	0.18	98.61
prv12	core	b.d.	0.52	55.07	0.53	38.45	0.36	0.03	0.04	0.04	0.25	1.40	b.d.	0.01	0.20	96.91
prv12	core	b.d.	0.58	55.05	0.55	38.55	0.36	0.02	0.04	b.d.	0.35	1.50	b.d.	0.02	0.18	97.19
prv12	rim	b.d.	0.60	54.84	0.49	38.57	0.38	b.d.	0.06	0.01	0.31	1.40	b.d.	b.d.	0.20	96.85
prv13	core	b.d.	0.28	55.91	0.42	38.59	0.32	0.02	0.02	0.04	0.35	1.40	0.03	b.d.	0.27	97.63
prv13	rim	b.d.	0.11	55.85	0.55	39.26	0.40	0.03	0.05	b.d.	0.28	1.70	0.06	b.d.	0.25	98.54
prv13	core	b.d.	0.47	55.94	0.57	38.91	0.42	0.01	0.05	b.d.	0.31	1.71	0.02	b.d.	0.28	98.68
prv13	core	b.d.	0.61	55.02	0.58	38.90	0.39	0.01	0.04	b.d.	0.25	1.64	b.d.	b.d.	0.26	97.70
prv13	rim	b.d.	0.04	55.39	0.34	39.26	0.35	0.04	0.04	b.d.	0.18	1.76	b.d.	b.d.	0.21	97.62
prv14	core	b.d.	0.54	55.02	0.56	38.80	0.37	0.01	0.05	b.d.	0.29	1.54	b.d.	b.d.	0.18	97.37
prv14	rim	b.d.	0.41	54.58	0.73	38.79	0.39	0.02	0.03	b.d.	0.34	1.66	b.d.	b.d.	0.22	97.16

Appendix 2A: *Continues*

Units are in wt.%		SiO_2	Ce_2O_3	TiO_2	La_2O_3	CaO	Al_2O_3	K_2O	MgO	NiO	Na_2O	FeO	MnO	Cr_2O_3	SrO	Total
Analysis	core/rim															
Sample Y5747																
prv14	core	b.d.	0.64	55.15	0.62	38.82	0.34	0.02	0.02	b.d.	0.37	1.44	b.d.	0.01	0.22	97.66
prv14	rim	b.d.	0.31	55.51	0.64	38.99	0.36	0.01	0.06	b.d.	0.30	1.55	b.d.	0.04	0.23	97.99
prv15	core	b.d.	0.64	56.02	0.46	38.54	0.36	0.02	0.07	0.02	0.36	1.55	0.02	b.d.	0.19	98.26
prv15	rim	b.d.	0.70	55.62	0.47	38.73	0.38	0.02	0.09	b.d.	0.42	1.55	0.01	b.d.	0.12	98.12
Sample Y5759																
prv1	core	b.d.	0.57	55.90	0.58	38.63	0.24	0.03	0.06	b.d.	0.33	1.21	0.04	0.07	0.18	97.83
prv1	rim	b.d.	0.75	56.09	0.50	38.84	0.29	0.02	0.03	0.02	0.31	1.29	0.03	0.05	0.17	98.38
prv1	rim	b.d.	0.43	56.04	0.36	38.95	0.36	0.03	0.05	0.02	0.40	1.35	b.d.	0.02	0.22	98.21
prv1	rim	b.d.	b.d.	56.09	0.42	39.64	0.16	0.07	0.01	0.02	0.33	1.49	0.02	b.d.	0.46	98.73
prv1	core	b.d.	0.42	56.07	0.54	38.63	0.27	0.02	0.04	b.d.	0.38	1.27	0.01	0.01	0.21	97.87
prv1	core	b.d.	0.56	56.24	0.30	39.15	0.25	0.01	0.04	b.d.	0.27	1.25	b.d.	0.04	0.19	98.30
prv1	rim	b.d.	0.50	56.13	0.40	39.17	0.35	0.03	0.06	0.01	0.34	1.31	b.d.	0.03	0.21	98.52
prv1	rim	b.d.	0.22	55.91	0.54	39.68	0.35	0.05	0.04	b.d.	0.19	1.60	0.03	b.d.	0.23	98.83
prv3	core	0.01	0.28	56.02	0.47	39.24	0.31	0.02	0.03	b.d.	0.29	1.25	b.d.	0.08	0.21	98.21
prv3	rim	b.d.	b.d.	56.42	0.32	39.67	0.15	0.05	b.d.	0.04	0.25	1.33	0.01	b.d.	0.33	98.56
prv3	rim	b.d.	b.d.	56.12	0.16	39.40	0.15	0.06	0.04	b.d.	0.42	1.50	0.02	b.d.	0.22	98.08

Appendix 2A: *Continues*

Units are in wt.%		SiO_2	Ce_2O_3	TiO_2	La_2O_3	CaO	Al_2O_3	K_2O	MgO	NiO	Na_2O	FeO	MnO	Cr_2O_3	SrO	Total
Analysis	core/rim															
							Sample Y5759									
prv8	core	b.d.	0.50	55.70	0.49	39.04	0.37	0.02	0.05	0.02	0.30	1.43	0.08	0.03	0.17	98.18
prv8	rim	b.d.	b.d.	56.31	0.21	39.32	0.11	0.02	0.02	0.06	0.42	1.34	0.01	b.d.	0.30	98.10
prv9	core	b.d.	0.63	55.57	0.39	38.52	0.34	0.01	0.06	0.06	0.34	1.24	b.d.	0.06	0.19	97.41
prv9	rim	0.03	b.d.	56.13	0.16	39.19	0.14	0.03	0.03	b.d.	0.41	1.29	0.05	b.d.	0.23	97.68
prv9	rim	0.02	b.d.	56.17	0.38	39.31	0.13	0.04	0.01	0.03	0.35	1.36	0.05	b.d.	0.22	98.07
prv9	core	b.d.	0.30	55.61	0.46	39.01	0.37	0.01	0.03	0.05	0.34	1.29	0.02	b.d.	0.20	97.67
prv10	core	b.d.	0.72	55.58	0.60	38.20	0.29	0.02	0.05	b.d.	0.47	1.17	b.d.	b.d.	0.16	97.27
prv10	core	b.d.	0.67	55.49	0.61	38.09	0.31	0.02	0.07	b.d.	0.35	1.24	b.d.	b.d.	0.13	96.96
prv10	rim	b.d.	0.39	55.88	0.62	38.69	0.26	0.01	0.03	b.d.	0.39	1.18	0.04	0.04	0.19	97.71
prv10	rim	b.d.	0.36	54.70	0.51	38.61	0.23	0.02	0.04	b.d.	0.31	1.32	b.d.	0.02	0.22	96.36
prv10	rim	b.d.	0.61	56.13	0.44	38.66	0.36	0.02	0.05	0.01	0.29	1.17	0.07	0.02	0.19	98.01
prv10	rim	b.d.	0.29	55.80	0.47	38.69	0.29	0.01	0.07	b.d.	0.30	1.23	b.d.	0.01	0.26	97.40
prv10	rim	b.d.	0.40	55.86	0.46	38.67	0.36	0.02	0.04	b.d.	0.34	1.20	0.03	b.d.	0.22	97.58
prv10	rim	b.d.	0.21	55.55	0.50	38.61	0.34	0.02	0.06	0.02	0.28	1.17	0.02	b.d.	0.21	96.99
prv10	rim	b.d.	b.d.	55.61	0.20	39.43	0.16	0.03	0.05	b.d.	0.31	1.33	0.01	0.01	0.31	97.44
prv10	rim	0.02	b.d.	56.09	0.32	39.41	0.22	0.03	0.03	0.04	0.25	1.34	0.05	b.d.	0.23	98.02

Appendix 2A: *Continues*

Units are in wt.%		SiO_2	Ce_2O_3	TiO_2	La_2O_3	CaO	Al_2O_3	K_2O	MgO	NiO	Na_2O	FeO	MnO	Cr_2O_3	SrO	Total
Analysis	core/rim															
								Sample Y5759								
prv12	core	b.d.	0.50	55.80	0.35	38.56	0.29	0.02	0.05	b.d.	0.36	1.24	0.02	0.02	0.21	97.43
prv12	core	0.02	0.64	56.03	0.45	38.54	0.29	0.01	0.08	0.06	0.36	1.06	b.d.	0.11	0.23	97.84
prv12	rim	0.03	0.72	55.75	0.65	38.49	0.34	0.01	0.05	b.d.	0.39	1.18	0.06	0.08	0.17	97.94
prv12	rim	b.d.	0.43	55.91	0.53	38.98	0.30	0.01	0.08	0.06	0.25	1.27	0.03	0.09	0.22	98.16
prv12	rim	0.01	0.13	56.25	0.50	39.27	0.39	0.01	0.04	0.02	0.27	1.28	0.02	b.d.	0.23	98.40
prv12	rim	0.06	b.d.	56.36	0.32	39.34	0.18	0.01	0.03	0.02	0.33	1.26	0.01	b.d.	0.22	98.12
prv13	core	b.d.	0.29	55.92	0.27	38.84	0.29	0.01	0.06	0.04	0.29	1.24	0.04	b.d.	0.20	97.48
prv13	core	b.d.	0.47	55.82	0.58	39.00	0.32	0.02	0.02	b.d.	0.33	1.14	0.02	0.05	0.25	98.01
prv13	rim	b.d.	0.50	55.70	0.37	38.82	0.31	0.02	0.06	b.d.	0.29	1.20	0.02	b.d.	0.13	97.40
prv13	rim	b.d.	0.31	55.86	0.49	39.11	0.41	0.01	0.04	b.d.	0.24	1.39	b.d.	b.d.	0.23	98.07
prv13	rim	0.65	b.d.	55.88	0.36	39.28	0.21	0.02	0.13	b.d.	0.40	1.24	0.05	b.d.	0.30	98.49
prv14	core	b.d.	0.46	56.40	0.50	38.81	0.32	0.01	0.03	b.d.	0.30	1.17	b.d.	b.d.	0.19	98.17
prv14	rim	b.d.	b.d.	56.46	0.43	39.23	0.17	0.03	0.04	0.03	0.33	1.37	b.d.	b.d.	0.25	98.35
prv16	core	0.07	0.43	56.31	0.48	38.78	0.28	0.01	0.06	0.04	0.32	1.19	0.02	0.04	0.20	98.24
prv16	core	0.05	0.47	56.34	0.70	39.10	0.30	0.02	0.03	0.01	0.30	1.18	b.d.	0.05	0.16	98.71
prv16	rim	0.07	0.55	55.93	0.54	39.21	0.32	0.02	0.01	0.02	0.29	1.33	0.03	0.03	0.21	98.55
prv16	rim	0.05	b.d.	56.40	0.26	39.71	0.20	0.11	0.03	0.03	0.35	1.34	b.d.	b.d.	0.30	98.76

Appendix 2A: *Continues*

Units are in wt.%		SiO_2	Ce_2O_3	TiO_2	La_2O_3	CaO	Al_2O_3	K_2O	MgO	NiO	Na_2O	FeO	MnO	Cr_2O_3	SrO	Total
Analysis	core /rim															
								Sample Y5759								
prv17	core	0.02	0.77	56.04	0.58	38.51	0.31	0.01	0.09	0.01	0.36	1.18	0.03	b.d.	0.20	98.09
prv17	core	b.d.	0.18	56.52	0.43	39.35	0.27	0.01	0.05	b.d.	0.30	1.21	0.05	b.d.	0.25	98.60
prv17	rim	b.d.	0.23	56.44	0.43	39.18	0.28	0.02	0.05	b.d.	0.28	1.30	b.d.	b.d.	0.17	98.38
prv17	rim	0.01	0.39	56.47	0.59	39.00	0.34	b.d.	0.05	0.05	0.34	1.37	0.02	0.02	0.24	98.88
prv17	rim	b.d.	0.10	56.40	0.37	39.80	0.39	0.02	0.04	b.d.	0.25	1.38	b.d.	0.01	0.22	98.98
prv17	rim	b.d.	b.d.	56.53	0.17	39.76	0.12	0.02	0.03	b.d.	0.20	1.48	0.01	b.d.	0.40	98.70
prv18	core	0.02	0.84	55.75	0.67	37.90	0.33	0.03	0.07	0.01	0.39	1.25	b.d.	b.d.	0.21	97.48
prv18	rim	0.05	0.12	56.19	0.51	39.31	0.30	0.01	0.06	b.d.	0.23	1.27	0.03	b.d.	0.21	98.28
prv18	rim	0.02	0.27	56.32	0.38	39.22	0.28	0.01	0.05	b.d.	0.29	1.29	0.03	b.d.	0.23	98.39
prv18	rim	0.01	0.16	56.32	0.29	39.12	0.31	0.02	0.07	b.d.	0.28	1.29	0.05	b.d.	0.19	98.10
prv18	rim	0.04	0.46	56.16	0.60	38.74	0.35	0.01	0.03	b.d.	0.29	1.38	0.04	0.03	0.19	98.31
prv18	rim	0.01	b.d.	56.52	0.35	38.54	0.11	0.03	0.02	0.02	0.45	1.30	b.d.	b.d.	0.33	97.66

Appendix 2B: Trace element composition of perovskites from Weasua

	Sample Y5747								
	prv1_rim	prv1_rim	prv2_rim	prv4_rim	prv7_rim	prv8_core	prv12_core	prv14_rim	prv15_rim
ppm									
Li	1.74	15.57	5.61	-	535.50	8.46	0.87	-	-
Sc	6.51	7.32	8.33	8.41	0.13	5.21	6.19	8.10	4.98
Mn	213.70	228	280.10	209.90	261.70	237.30	254.60	257.90	254.20
Ni	4.36	9.76	2.46	1.74	12.98	28.98	1.58	17.52	23.87
Rb	-	2.26	-	-	-	-	-	-	2.81
Sr	2995	3125	3087	3173	3120	2910	2931.50	3084	3320
Y	208.90	217.90	217.50	241.20	223.20	202.70	308.90	220.60	225.50
Zr	398.60	462.40	440.40	543.30	466.20	360.90	769.70	413.40	478.90
Nb	4602	4526	4846	5439	4519	4617	7130.50	4636	4947
Ba	25.22	35.49	24.31	29	47.25	86.40	32.26	26.68	24
La	7847	8330	8103	6829	7797	7686	6672	7816	7835
Ce	13790	16710	14280	15350	17070	17950	15450	18730	20020
Pr	2033	1989	2142	1579	1900	2047	1517.50	2086	2122
Nd	7874	7480	8318	6273	7060	7948	5854	8299	7197
Sm	867.20	886.40	938.70	712.70	849.70	867.40	658.80	895.70	856.30
Eu	186.70	186.90	196	170.10	188.60	179.10	165.30	188.30	190.60
Tb	31.95	32.20	30.73	27.78	33.20	29.36	31.97	31.82	33.58
Gd	342.20	362.30	364.20	308.10	326.60	334	322.40	338.50	341.50
Dy	103.30	108.30	111.80	107.80	100.90	100.90	123.65	116.10	101.70
Ho	12.51	13.83	11.64	12.48	12.66	10.55	15.48	12.64	11.89
Er	19.08	18.05	21.32	22.40	22.50	18.07	29.74	20.58	19.33

Appendix 2B: *Continues*

	Sample Y5747								
	prv1_rim	prv1_rim	prv2_rim	prv4_rim	prv7_rim	prv8_core	prv12_cor	prv14_rim	prv15_rim
ppm									
Tm	1.68	1.22	1.65	1.83	1.57	1.27	2.52	1.94	2.51
Yb	6.51	8.27	6.51	7.64	6.86	6.23	11.01	7.25	5.33
Lu	0.97	0.57	0.89	0.62	0.68	0.58	0.75	0.72	0.59
Hf	19.89	20.59	21.30	25.23	21.38	15.91	24.42	19.19	19.41
Ta	656.60	633.40	718.70	520.50	568.10	620.20	467.30	646.90	640
Pb	111.30	125	109.20	65.17	103.80	139.10	72.79	111.40	147.70
Th	1665	1662	1743	1032	1440	1721	1012.80	1720	1438
U	53.54	53.20	61.15	53.09	56.55	45.61	92.41	55.50	63.67

	Sample Y5759									
	prv1a_cor	prv1b_cor	prv3_core	prv8_core	prv9_core	prv10_cor	prv13_cor	prv16core	prv18core	prv19core
ppm										
Li	-	-	-	0.67	0.41	0.91	1.89	3.82	7.72	-
Sc	9.81	7.41	12.01	13.34	7.03	9.89	6.94	9.15	7.85	9.84
Mn	215.40	223	284.10	429.20	243.10	245.80	238.47	208.60	537.60	296.85
Ni	1.33	2.08	12.99	8.38	2.59	3.30	0.98	11.95	55.81	8.86
Rb	-	-	17.43	14.91	6.27	-	6.87	-	-	3.25
Sr	3181.50	3320	6341	4582	3377	3236	2973.33	2915	3111	2794.50
Y	209.60	225.55	222.30	254.60	264.50	218	207.13	203.10	261.10	214.35
Zr	470.05	578.50	721.20	757.70	739	379.30	361.10	369.90	467.45	343.75
Nb	4785.50	4828.50	5248	5479	5491	4928	4416.33	4245	5567.50	4877

Appendix 2B: *Continues*

	Sample Y5759									
	prv1a_core	prv1b_core	prv3_core	prv8_core	prv9_core	prv10_core	prv13_core	prv16core	prv18core	prv19core
ppm										
Ba	36.39	136.30	2277	838.90	134.90	60.44	16.85	231.90	39.56	21.84
La	6845.50	6600.50	5926	5860	5996	7527	6746	7156	6717	8456
Ce	14525	14195	11600	10820	11750	16120	15333.33	16600	15735	19050
Pr	1492	1420	1163	1085	1169	1927	1582.67	1700	1671	2322
Nd	5705	5397.50	4348	4030	4432	7310	6077.33	6627	6477	9195
Sm	671.80	634.75	546.70	530	575.10	832.70	704.73	735.10	713.80	1000.65
Eu	146.80	146	132.10	132.30	139.60	176.60	159.43	157.50	170.80	206.80
Tb	27.09	27.57	25.10	26.69	29.84	30.48	28.12	27.49	29.24	34.62
Gd	285.35	282.85	261.60	267.10	268.30	327.80	291.23	288.30	311.90	370.75
Dy	95.76	101.48	94.37	106.90	109.30	106	102.83	95.25	116.25	113.55
Ho	12.77	12.63	12.65	13.72	13.85	12.16	12.10	10.16	14.30	13.87
Er	20.75	20.40	20.86	21.31	26.19	19.49	19.05	18.68	26.98	20.87
Tm	1.70	1.93	1.37	1.61	1.74	1.52	1.81	1.36	2.10	1.80
Yb	7.78	6.96	8.88	8.20	11.02	6.46	7.08	5.46	9.72	6.48
Lu	0.70	0.87	0.84	1.09	0.97	0.47	0.59	0.85	0.80	0.59
Hf	23.57	25	32.99	33.56	32.91	18.01	18.10	17.07	21.01	16.06
Ta	512.20	470.75	381.10	366.70	385.40	642	503.87	532.30	577.95	815.95
Pb	61.05	58.45	37.83	33.79	34.05	98.92	79.96	80.95	94.89	202.75
Th	933.10	841	464.40	319.40	512.60	1678	1013.57	1312	1487	3024.50
U	68	73.24	67.02	85.31	76.63	76.59	77.79	62.12	96.78	90.07